Linear and nonlinear magnetization dynamics in thin ferromagnetic films and nanostructures

Dissertation
zur Erlangung des Doktorgrades
der Naturwissenschaften
(Dr. rer. nat.)
der Fakultät für Physik
der Universität Regensburg

vorgelegt von

Hans Bauer

Diplom Physiker
aus Obernzell

Dezember 2014

Die Arbeit wurde von Prof. Dr. Christian H. Back angeleitet.
Das Promotionsgesuch wurde am 16.04.2014 eingereicht.
Das Prüfungskolloquium fand am 05.02.2015 statt.

Prüfungsausschuss:

Vorsitzender:	Prof. Dr. Ingo Morgenstern
1. Gutachter:	Prof. Dr. Christian H. Back
2. Gutachter:	Prof. Dr. Christoph Strunk
weiterer Prüfer:	Prof. Dr. Jascha Repp

Acknowledgments

First I want to thank my supervisors Christian Back for his way of being the 'boss' and Georg Woltersdorf for his patience in teaching me sample fabrication and measurement techniques, Jean-Yves Chauleau for many fruitful discussions especially on spin wave doppler and vortex domain walls, various PhD and Master student from our group, who I collaborated with in different projects, namely

1. Ajay Gangwar (AMR and spin motif force, vortex dynamics)
2. Johannes Stigloher (spin wave doppler)
3. Markus Härtinger (beamtimes in Bessy)
4. Martin Obstbaum (DC-AMR and ISHE)
5. Matthias Kronseder (domain patterns)
6. Robert Islinger and Tobias Weindler (Vortex domain wall motion)

Furthermore, I want to thank external PhD students Sebastian Neusser (antidot-lattices) from TUM and Markus Sproll (Vortex core switching) from MPI Stuttgart and Prof. Weiss for access to the clean room facilities in the first time of my thesis. Apart from those already mentioned I want to thank all the others from the chair who let me enjoy my time here, especially Helmut Körner and Martin Decker. Last but not least, I want to thank my parents Edith and Hans and my sister Angelika for their longterm support.

Contents

1 Introduction **9**
- 1.1 Applicability of micromagnetics . . . 9
- 1.2 Landau-Lifshitz equation . . . 9
- 1.3 Effective field terms . . . 10
- 1.4 Damping term . . . 10
- 1.5 STT terms . . . 11
- 1.6 Software packages OOMMF and MuMax . . . 11

2 Nonlinear FMR **13**
- 2.1 Linear FMR . . . 14
- 2.2 Spin wave dispersion . . . 15
- 2.3 Nonlinear spin wave theory . . . 16
  - 2.3.1 XMCD-measurements . . . 18
  - 2.3.2 Energy relaxation . . . 22
  - 2.3.3 Analytic model . . . 23
- 2.4 Frequency shift . . . 26
- 2.5 Theoretical model: Mathieu equation . . . 27
- 2.6 Micromagnetic modeling . . . 28
  - 2.6.1 Edge effects and out-of-plane magnetized structures . . . 30
  - 2.6.2 Thermal effects . . . 33
- 2.7 Side-notes . . . 33
  - 2.7.1 Sample preparation . . . 33
  - 2.7.2 X-ray magnetic circular dichroism . . . 33
  - 2.7.3 Microwave circuitry . . . 35
- 2.8 Thresholds for various cases . . . 35
  - 2.8.1 Thickness and frequency dependence . . . 35
  - 2.8.2 Butterfly-curves and 2-magnon-scattering . . . 37
  - 2.8.3 Subsidiary absorption . . . 39
  - 2.8.4 YIG . . . 41
- 2.9 Summary . . . 41

3 Spin waves in stripes **43**
- 3.1 The excitation scheme . . . 43
- 3.2 Spin wave propagation in a wire . . . 46
- 3.3 Spin transfer torque parameters . . . 53
- 3.4 Spin waves in antidot arrays . . . 57
  - 3.4.1 Spin wave modes . . . 57
  - 3.4.2 Angular dependence . . . 58

3.4.3 Spin wave injection into the antidot lattice 59

4 Vortex core dynamics **61**
4.1 Collective coordinates 61
4.2 Vortex domain wall dynamics 64
4.2.1 Above the Walker breakdown 66
4.2.2 Below the Walker breakdown 69
4.3 Nonlocal damping 73
4.4 Nonlinear vortex dynamics 77
4.5 Linear interference in pulsed experiments 83
4.6 CW and CCW excitation 84

Overview

In this thesis magnetization dynamics in thin magnetic films and nanostructures is investigated. The magnetic material of choice is $Ni_{80}Fe_{20}$, a metallic alloy (Permalloy) with vanishing crystalline anisotropies, which is ferromagnetic at room temperature with relatively low damping. The spatial extent of the investigated nanostructures is typically in the range of micro- and nanometers and the time scale ranges from tens of picoseconds up to microseconds. On the theoretical side this is the domain of micromagnetics described by the Landau-Lifshitz-Gilbert equation introduced in the first section and on the experimental side Magneto-Optic Kerr Effect Microscopy (ST-MOKE) and X-Ray Magnetic Circular Dichroism (XMCD) have been used.

The second section is devoted to the study of spin waves, mainly in thin films, where at large excitation amplitudes spin wave instabilities are observed. The main achievement in this section is the deep understanding of nonlinear spin wave dynamics above standard three- and four magnon scattering processes and their experimental observation.

In the third section the thin film is patterned once into an antidot lattice and also into a stripe. In both cases propagating spin waves behave similarly. Their dispersion is investigated in detail in order to allow for the utilization of spin waves as a probe for spin transfer torques and to investigate the possible technological use of magnonic crystals.

Another potentially useful technology is studied in the forth section. Therefore topological objects are used to store information. In the so-called racetrack memory domain walls in stripes contain the binary information that is transported through a racetrack. We thus studied the propagation behavior of domain walls and used it to infer a parameter of an extended micromagnetic model. In vortex random access memory bits are proposed to be encoded in the discrete states of a magnetic vortex and selective bit reversals with interactions of spin wave modes with the vortex core are studied.

From another point of view, section II deals with spin wave dynamics in 2D, section III marks the transition to 1D and in section IV spin waves are investigated within a magnetic dot (0D). While the magnetic ground state is topologically trivial in sections II and III, section IV also deals with topologically more complex magnetization configurations and its excitations.

Chapter 1

Introduction to micromagnetics

1.1 Applicability of micromagnetics

Micromagnetics cover the relevant physics describing the behavior of the magnetization in ferromagnets on length scales large enough to approximate the underlying atomic structure with a continuous real valued function $\vec{M}(\vec{r})$. This typically covers the range from several nanometers (vortex cores) to tens of micrometers (magnetic domains, propagating spin waves). Going to smaller length scales means that quantum effects become more important. But although the origin of the exchange interaction for example cannot be described in a classic picture, its consequences on a larger length scale, namely the tendency to align magnetization, can be implemented. Thus micromagnetics is able to describe structures like domain walls that are too large to be described in a purely quantum mechanical model. The connection between microscopic quantities and effects observable on micromagnetic length scales allows for the determination of the first by the latter. Furthermore magnetic memory applications are on micromagnetic length scales and make it interesting to study micromagnetics not only for the underlying physics but also for technological reasons. Bit reversal rates are in the GHz range as well as typical time scales for the dynamics of the magnetization. In this context it is obvious that much emphasis is put on magnetization dynamics particularly since material parameters are often determined through measurements of resonances, like in various kinds of FMR (ferromagnetic resonance) experiments.

In this thesis we study magnetization dynamics of ferromagnetic thin films and nanostructures within the micromagnetic frame work.

1.2 Landau-Lifshitz equation

The equation that determines magnetization dynamics considered in this thesis was found by Lev Landau and Evgeny Lifshitz [1] already in 1935. The dynamics is determined by the precessional term and the damping term. While the first one describes a precessional motion of the magnetization around an effective

field, only the additional damping term is able to describe energy dissipation away from the magnetic system and relaxation into the equilibrium state.

$$\frac{d\vec{M}}{dt} = \underbrace{-\gamma\mu_0\vec{M}\times\vec{H}_{\text{eff}}}_{\text{precession}} \underbrace{-\frac{\lambda}{M_s^2}\vec{M}\times\left(\vec{M}\times\vec{H}_{\text{eff}}\right)}_{\text{dissipation}} \tag{1.1}$$

with the gyromagnetic ratio $\gamma = g|e|/(2m_e) \approx 1.76\cdot 10^{11}\ \mathrm{s^{-1}T^{-1}}$, the vacuum permeability $\mu_0 = 4\pi\cdot 10^{-7}\ \frac{\mathrm{Vs}}{\mathrm{Am}}$, the saturation magnetization M_s and the damping parameter λ.

1.3 Effective field terms

The effective magnetic field is defined via the variation of the free energy functional:

$$\mu_0\vec{H}_{\text{eff}} = -\frac{\delta E}{\delta\vec{M}}. \tag{1.2}$$

The free energy density usually contains contributions from exchange, dipolar and Zeeman terms as well as from magneto-crystalline anisotropies [2, 3]:

$$e_{\text{exchange}} = A|\nabla\vec{M}|^2 \tag{1.3}$$

$$e_{\text{dipolar}} = \frac{1}{2}\mu_0\vec{H}^2_{\text{induced}} \tag{1.4}$$

$$e_{\text{Zeeman}} = -\mu_0\vec{H}\cdot\vec{M} \tag{1.5}$$

where $\vec{H}_{\text{induced}}$ is the magnetic field that is induced by the magnetization and satisfies the Maxwell-equations $\nabla\cdot(\vec{H}_{\text{induced}}+\vec{M}) = 0$ and $\nabla\times\vec{M}_{\text{induced}} = 0$. As the main material in this thesis is $Ni_{80}Fe_{20}$ (Permalloy) which has only very small crystalline anisotropies we neglect those anisotropy terms. It should only be mentioned that crystalline anisotropies can play an important role and even dominate the other contributions in materials like Fe [4]. A typical exchange parameter for simulations of Permalloy is $A = 1.3\cdot 10^{-11}$ J/m and the saturation magnetization is $M_s = 8\cdot 10^5$ A/m.

1.4 Damping term

In 1955 Gilbert [5, 6] replaced the damping term in the Landau-Lifshitz equation by:

$$\frac{\alpha}{M_s}\vec{M}\times\frac{d\vec{M}}{dt} \tag{1.6}$$

For small damping both relaxation terms give the same solution and we use the one that is easier to evaluate for the specific problem under investigation. Both forms are mathematically equivalent when the damping and precessional constants (λ, α and γ) are adjusted accordingly. A typical value for the Gilbert damping constant is $\alpha = 0.008$ for $Ni_{80}Fe_{20}$, which is among the lowest values for ferromagnetic metals.

1.5 STT terms

To account for interactions of the magnetization with an electrical current flowing through the ferromagnet additional torque terms (spin-transfer-torque, STT) have been introduced [7, 8, 9, 10, 11]. We only consider the Zhang-Li STT terms which model the effect of a spin polarized current that is laterally flowing through a non-uniform magnetization configuration. The whole dynamic equation then reads:

$$\frac{d\vec{m}}{dt} = -\gamma\mu_0\vec{m}\times\vec{H}_{\text{eff}} + \alpha\vec{m}\times\frac{d\vec{m}}{dt} + \underbrace{u\cdot\vec{m}\times(\vec{m}\times\vec{m}')}_{\text{adiabatic}} + \underbrace{\beta u\cdot\vec{m}\times\vec{m}'}_{\text{non-adiabatic}} \quad (1.7)$$

where $\vec{m}'$ is the spatial derivative of the normalized magnetization $\vec{m} = \vec{M}/M_s$ in the direction of the current flow, $u = \frac{jPg\mu_B}{2eM_s}$ the spin drift velocity, j the current density, P the current polarization, μ_B the Bohr magneton, e the electron charge and β the non-adiabaticity parameter.

1.6 Software packages OOMMF and MuMax

To numerically simulate the time evolution of a ferromagnetic system according to equation (1.7) and similar equations, software packages have been developed by several groups. While some of them are finite element methods (FEM) (magnum.fe [12], TetraMag [13], FastMag [14], Nmag [15]) and work on irregular meshes others are finite difference methods (FD) (OOMMF [16] and MuMax[17]) and rely on a regular meshgrid. The advantage of FEM is that typically less cells are required but the mesh has to be chosen such that the cell size is sufficiently small in the region where significant gradients of the magnetization are expected. This is not always straight forward as for example spin waves with short wave length are created when a vortex-anti-vortex pair is annihilated or in the case of parametric excitation of spin waves. FD methods typically use more cells but are faster in calculating the dipolar fields arising from the magnetization configuration. As the dipolar interactions are the only energy contribution in the free energy with a long interaction range, their computation typically consumes most of the simulation time. Therefore in order to improve the runtime of micromagnetic software the focus is on the fast implementation of the dipolar interactions. On a rectangular equally spaced meshgrid the dipolar interactions can be written as a convolution (due to invariance under translations by an integer number of cells) which can be evaluated very efficiently with the help of fast Fourier transforms (FFT). This was already implemented in oommf [16] and only recently the massive parallel power of cheap consumer graphics cards (CUDA-technology,[18]) has been used to further improve performance by up to a factor of 100 [17] at the cost of less (single precision instead of double precision) accuracy. We have extensively used mumax (and mumax2) for our simulations due to its computational capabilities and its availability in the public domain.

Chapter 2

Nonlinear FMR

Nonlinear behavior is observed in a vast range of systems. The physical description often relies on dramatic simplifications, a prominent example being the harmonic oscillator which allows using linear response theory. In many fields of physics, reaching from phonon dynamics to cosmology, anharmonic terms enrich the physical description, but complicate the analysis. The transition between harmonic and anharmonic behavior may, for example, occur when an external driving force exceeds a well defined threshold. While in some cases a transition from a well behaved and predictable linear system to a nonlinear or even chaotic system is detrimental, nonlinear phenomena are of high interest due to their fundamental richness and complexity. Examples range from nonlinear optics, plasma physics, climate modeling or fluid dynamics to name but a few. In addition, many technologically useful processes rely on nonlinear phenomena. Examples are solitonic wave propagation, high harmonic generation, rectification and frequency mixing. In spintronics the reversal of the magnetization in nanostructures is one of the key prerequisites for functional magnetic random access memory cells. Equally important is the complete understanding of spin transfer torque driven nano-oscillators which may function as radio frequency emitters or receivers. Both phenomena inherently involve large precession angles of the magnetization deep in the nonlinear regime.

In general, linear eigenmodes can be viewed as non-interacting quasi-particles whose interaction is set by some control parameter. When a critical interaction strength is reached many systems undergo an instability, i.e. an abrupt change of the systems physical properties. For example the interaction between quasi-particles in cuprates can be tuned by doping levels of the host compound and a transition from a weakly to a strongly interacting system leads to very distinct phases. In the case of spin wave excitation at ferromagnetic resonance, where the degree of interaction depends on the spin wave amplitude and where the interaction can easily be controlled by an external magnetic rf-field, one observes an instability of non-uniform spin wave modes. Very often nonlinear effects can only be accounted for by performing cumbersome micromagnetic calculations (subsection 2.6). A theory describing nonlinear phenomena in terms of modes that are mostly decoupled from each other is thus highly desired.

In the following we use time resolved X-ray magnetic circular dichroism experiments to determine precisely the number of parametrically exited magnons in a $Ni_{80}Fe_{20}$ thin film sample and show that the commonly used models of

nonlinear resonance fail to properly describe the physics that is observed at low magnetic bias fields (subsection 2.3.1). In contrast to the established theory of nonlinear ferromagnetic resonance we find that strong amplitude-phase modulations dominate the critical spin waves. The low field regime is of particular interest for microwave assisted switching [19], where the energy barrier is overcome with the combination of a dynamic field excitation and a static field which counteracts the uniaxial anisotropy. We numerically study a model which allows us to identify the critical modes and find their threshold rf-amplitudes for parametric spin wave generation. In fact a new series of spin wave modes with strong and fast amplitude phase oscillations is found. Furthermore we revisit other experiments that investigate similar samples.

2.1 Linear FMR

Ferromagnetic resonance (FMR) [20, 21, 22] is an experimental technique where typically the uniform magnetization of a ferromagnetic sample is excited by a uniform external microwave field with frequencies in the GHz regime and the precessing magnetization is probed by one of several possible ways [23]. In this thesis local detection by time-resolved magneto-optic Kerr-effect (TR-MOKE) and spatially averaged measurements of the X-ray magnetic circular dichroism (XMCD) have been used. FMR is a widely used technique especially because of the possibility to extract material parameters like the damping constant α, or anisotropies (stiffness fields) from measurements.

In linear FMR, i.e. below a certain excitation threshold one considers deviations from the magnetization ground state only in linear order to find the resonance frequency and linewidth together with the (linear) eigenmodes.

One possibility is to write $\vec{M} = \vec{M}_0 + \vec{m}$, where $\vec{M}_0$ is the equilibrium magnetization and $\vec{m}$ are small deviations which are perpendicular to $\vec{M}_0$ because of the restriction $|\vec{M}| = M_s$. When inserted into the LLG equation and leaving out higher order terms a 2-by-2 system of equations (in the two components of $\vec{m}$ which are perpendicular to $\vec{M}$) has to be solved to find the eigenfrequencies and eigenmodes or the susceptibility tensor.

This perturbative method has been carried to higher orders (and in more systematic ways) already by Schlömann [24], by several authors in the 1970s [25, 26] and also recently in reference [27]. We will come back to this work in the next section when we consider nonlinear spin waves.

Another, though closely related, way of obtaining the linewidth and resonance frequency is found by considering the uniform mode as a macrospin $\vec{M}$ and writing its free energy $F(\vec{M})$ as a function of the orientation of the magnetization. As the effective field around which the magnetization precesses can also be written as a function of the magnetization $\vec{H}_{\text{eff}} = -\frac{\partial F}{\partial \vec{M}}$ it is not surprising that the resonance frequency is proportional to the curvature of the energy density landscape around the equilibrium position or formulated in a differential geometric point of view: Due to the conservation of the magnitude of the magnetization vector $|\vec{M}| = M_s$ the linear spin wave excitations live on the tangential manifold TM with a symplectic structure due to the precession term. From this the frequency can be found as:

$$\frac{\omega}{\gamma M_s} \approx \sqrt{|F|} - i\frac{\alpha}{2} tr(F) \tag{2.1}$$

with $F_{i,j} = \frac{\partial^2 F}{\partial m_i \partial m_j}$ and $|.|$ denoting the determinant and $tr(.)$ the trace, i.e. precession is connected to the Gaussian curvature and relaxation to the mean curvature of the free energy landscape for small α and small precession angles.

For illustration we consider FMR for a plane film magnetized along an in-plane magnetic field H_x. The free energy is given by:

$$F = -\mu_0 M_x H_x + \frac{1}{2}\mu_0 M_z^2, \tag{2.2}$$

i.e. z denotes the out-of-plane direction. $|\vec{M}| = M_s$ and therefore $M_x = \sqrt{M_s^2 - M_y^2 - M_z^2}$. The Hessian matrix with entries $F_{i,j}$ (i, j being the coordinates y and z.) reads:

$$F_{i,j} = \frac{\mu_0}{M_s} \begin{pmatrix} H_x & 0 \\ 0 & H_x + M_s \end{pmatrix}_{i,j} \tag{2.3}$$

and using equation (2.1) we find the FMR resonance frequency for the in-plane magnetized film:

$$\omega = \gamma\mu_0 \sqrt{H_x(H_x + M_s)} - i\gamma\mu_0 \frac{\alpha}{2}(2H_x + M_s) \tag{2.4}$$

2.2 Spin wave dispersion for in-plane magnetized thin films

Before we start with the investigations of more complicated spin wave dynamics we briefly introduce the spin wave dispersion relation for the simple case of a thin in-plane magnetized film. The procedure for finding the dispersion relation is similar to finding the resonance frequency of the FMR mode. Only the demagnetizing and exchange terms have to be adapted to the finite wave vector. For illustration we show the spin wave dispersion relation according to [28] for a 50 nm thin $Ni_{80}Fe_{20}$ film that was saturated with an in-plane field of 20 mT (Fig. 2.1).

The spin wave dispersion is highly anisotropic in the wave number regime we are interested in, i.e. for wavelengths down to approximately 250 nm. In this regime dipolar interactions dominate the dispersion and exchange interactions become relevant and dominant only for shorter wavelengths. While due to the precessional motion of the magnetization spin waves in all directions create magnetic surface charges where the dynamic magnetization points out-of-plane ($\nabla \cdot B = 0$), there are no magnetic volume charges when the wave vector is parallel to the static magnetization. In this case the dispersion relation is very flat and actually starts with a negative slope, i.e. group velocity. These spin waves are therefore called backward volume (BV) spin waves and the term is also used for the direction parallel to the static magnetization for in-plane magnetized films. The direction perpendicular to the BV-direction is called the Damon-Eshbach (DE) direction. Spin waves in this direction are characterized by a maximum of the group velocity. Therefore spin waves propagation much better perpendicular to the static magnetization than parallel to it. The third geometry that is often used is the forward volume (FV) geometry, in which the static magnetization is pointing out-of-plane and the spin wave dispersion is isotropic for spin waves propagating in the plane of the film.

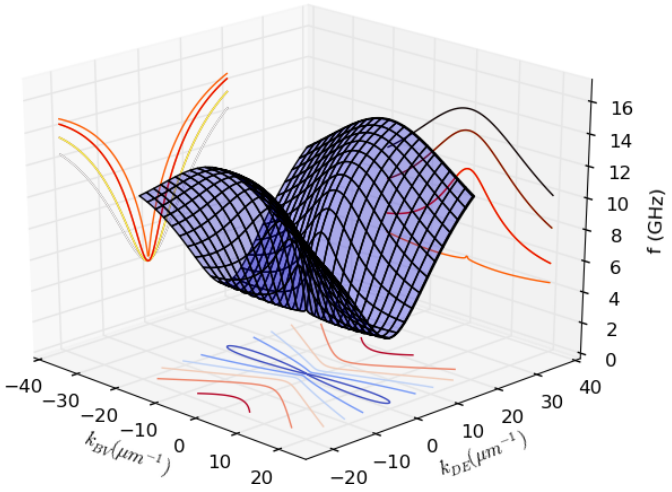

Figure 2.1: Lowest spin wave dispersion branch for a 50 nm thin $Ni_{80}Fe_{20}$ film and 20 mT static in-plane field. Spin waves with a wave vector parallel to the static in-plane magnetization (BV-direction) precess at lower frequencies than spin waves perpendicular to M and the film normal (DE-direction). Contour lines indicate that the minimum of the spin wave manifold is not the FMR-mode ($k = 0$), but that it is lying in BV-direction.

The spin wave dispersion relation obviously depends on the magnetic field, but not only on its direction, but also on its magnitude as was already shown for the FMR mode ($k = 0$) (eq. 2.4). Roughly speaking an increasing static field shifts the dispersion relation to higher frequencies. But the pockets in BV-direction become deeper as well due to the decreasing ellipticity of the magnetization precession.

The spin wave dispersion also depends on the thickness of the film. The larger magnetic moment per area film causes more volume charges for DE spin waves and increased resonance frequencies. Therefore thicker films show better spin wave propagation due to higher group velocities. So far we only considered the lowest spin wave branch, i.e. we neglected higher spin wave modes (perpendicular standing spin waves) due to the quantization in the out-of-plane direction. For most of this work this simplification is justified as higher spin wave branches are separated from the lowest one by the exchange splitting, which is still several GHz even for 100 nm thick $Ni_{80}Fe_{20}$ films (Fig. 2.17 c).

2.3 Nonlinear spin wave theory

In this section we briefly summarize the main points of Suhl's spin wave instability theory. We discuss the 'Hamiltonian formulation of nonlinear spin-wave dynamics: Theory and applications' by Pavel Krivosik and Carl E. Patton [27], and chapters of the book 'Wave Turbulence Under Parametric Excitation' by L'vov [29]. While Krivosik and Patton published their work only recently in a 27-page paper in Physical Review B in 2010, the book by L'vov is based on

work in the 1970s by V.E. Zakharov, V.S. L'vov and S.S. Starobinets.

The equation-of-motion approach briefly outlined in the previous section is intuitive as it directly starts with the LLG equation and has been widely used for linear FMR [23]. The favored method used for nonlinear spin wave dynamics [24] is based on a Hamiltonian formulation. One of the advantages is that this formalism is not specific to spin waves and nonlinear phenomena of very different systems can be understood within a common framework. Victor S. L'vov [29] for example mentions sound in continuous media, gravitational waves on liquid surfaces and capillary waves. The procedure is well described in the literature [29, 27] and extends to states far above the nonlinear threshold (S-theory and S,T^2-theory [29, 25, 26]). The work is lengthy and therefore we only want to briefly outline the results that are important for our study of nonlinear FMR, i.e. we look at 1st and 2nd order Suhl instabilities. Here we follow Krivosik and Patton:

The energy of the dynamic magnetization is expressed in terms of the canonical variables a_k and a_k^* and resulting terms are then sorted by their order in a_k. The a_k and a_k^* are complex numbers and contain the precessing magnetization in the two transverse directions. The diagonalization of the Hamiltonian up to second order (classic analogon to the Holstein-Primakov transformation) corresponds to a change from the elliptically polarized spin wave modes a_k to the circularly polarized new modes b_k. I.e. the b_k describe the linear spin wave modes and b_0 the linear FMR mode. Third and fourth order processes are then processes that create and annihilate certain spin wave modes under momentum conservation. Energy conservation is not explicitly contained in the equations, but usually introduced and termed 'elimination of non-resonant terms'. Krivosik and Patton point out that for resonance saturation (i.e. FMR at high excitation amplitudes) for thin films, i.e. when three wave processes are forbidden by energy conservation the renormalized four wave processes have to be used instead of the 'bare' ones. Under this non-resonance condition another transformation (Krasitskii) eliminates the three wave processes in the forth order Hamiltonian leading to a Hamiltonian of the following form:

$$U = \sum_k \omega_k c_k^*(t) c_k(t) + \frac{1}{2} \sum_{1234} \tilde{W}_{12,34} c_1(t) c_2(t) c_3^*(t) c_4^*(t) \Delta(1+2-3-4) + \text{RFO-terms}, \quad (2.5)$$

where RFO are remaining forth order terms which are also neglected and $c_k(t) \approx |c_k(t)| e^{-i\omega_k t}$, where $|c_k(t)|$ corresponds to a slowly varying envelope. The Δ-function ensures energy and momentum conservation.

The spin wave instability threshold for 2nd order Suhl instability (Fig. 2.2), i.e. for the spontaneous decay of a pair of uniform spin waves into a pair of non-uniform spin waves with opposing wave vectors is then given by:

$$|c_0|_{\text{crit.}} = \min \left(\sqrt{\frac{\eta_k}{|\tilde{W}_{00,k(-k)}|}} \right)_{\omega_k = \omega_0}, \quad (2.6)$$

where η_k is the relaxation rate for a given mode with wave vector k. Equation

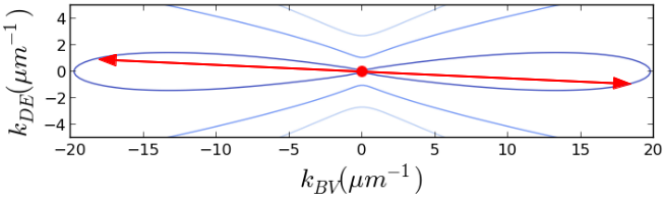

Figure 2.2: In the second order Suhl instability process two uniform magnons ($k = 0$) are scattered into two non-uniform magnons with opposing wave vectors but the same frequency as the uniform mode. The iso-frequency lines illustrate that this process where the total number of spin wave modes, momentum and energy are conserved is possible for all spin wave modes degenerate with the uniform mode.

2.6 expresses the power flow from the uniform mode into the critical mode above the threshold.

To conclude this section we want to stress that the Hamiltonian approach to nonlinear spin wave dynamics has been very successful in predicting nonlinear thresholds like the 2nd order Suhl instability threshold in the past. But we also want the reader to keep in mind the assumptions, especially energy conservation which is valid for systems which are invariant under translations in time. However, periodic driving of the system actually breaks this symmetry.

In the following section we therefore present an experimental and theoretical study of nonlinear FMR that demonstrates a case of nonlinear FMR where the theory of 1st and 2nd order Suhl instabilities cannot predict the correct critical modes and thresholds.

Our approach does not try to extend the Hamiltonian method to higher orders (it was checked that the higher order threshold calculated in [30] is much too high), but is more in the spirit of Bertotti et al. [31, 32] who investigated large angle rotationally invariant LLG-dynamics. They did this in the following way: Due to the rotational invariance (out-of-plane magnetization and circular driving fields) analytic solutions for the magnetization dynamics of a macrospin even for large angles of magnetization precession exist. Then small perturbations around this nonlinear mode (P-mode, the uniform mode) are considered and their equations of motion are numerically integrated to obtain an instability diagram.

2.3.1 XMCD-measurements

In this section we present measurements of longitudinal [33] and transverse [34] components of the dynamic motion of the magnetization vector by X-ray magnetic circular dichroism (XMCD) as a function of rf-power. At large driving amplitudes the results obtained clearly show that the low field nonlinear resonance behavior cannot be described adequately using existing models for nonlinear magnetic resonance [35]. This motivated us to numerically study spin wave turbulence and test existing theories, such as the Suhl theory. In a later section we show that the basic assumption of a slowly varying spin wave amplitude parameter is invalid at low bias fields and amplitude phase oscillations occur and dominate the nonlinear response.

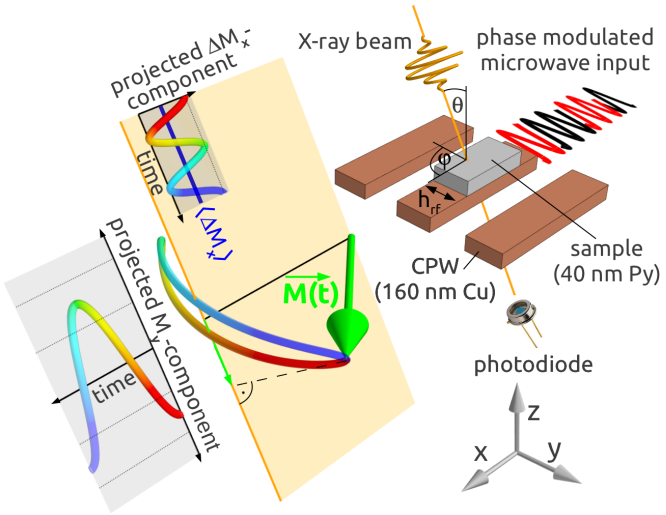

Figure 2.3: Sketch of the experimental setup. The transmitted X-ray intensity is modulated by the XMCD effect which is proportional to the magnetization component projected onto the beam direction. The in-plane component of the dynamic magnetization is measured coherently and the signal is mostly proportional to $M_y(t)$. In order to determine the change in the longitudinal magnetization we rotate the sample by 90° and measure the time-averaged longitudinal magnetization $\langle M_x \rangle$ by turning off the temporal synchronization between the excitation and the X-ray pulses.

Our experiments are performed using Permalloy films deposited on top of the signal line of coplanar waveguide structures. In all measurements a magnetic bias field $\vec{H}_{\mathrm{B}}$ forces the static magnetization to lie along the x-direction. A magnetic rf-field oriented along the y-direction leads to a forced precession of $\vec{M}$, as can be seen in Fig. 2.3. The precession of the magnetization vector is strongly elliptical due to the demagnetizing field. As shown in Fig. 2.3 the X-ray beam can be oriented at an angle $\theta = 30°$ with respect to the film normal. In this geometry the precession of the magnetization causes slight changes of the absorption of circularly polarized X-ray photons detected by a photo-diode in transmission. In a first set of measurements the X-ray beam is oriented as depicted in Fig. 2.3 ($\varphi = 90°$). The microwave excitation is synchronized to the X-ray bunches and due to the large ellipticity of the magnetization precession the detected signal is proportional to the in-plane magnetization M_y projected onto the X-ray beam. When the phase of the rf-driving field is set to 90° or 0° with respect to the X-ray bunches the measured signal represents either the real or the imaginary part (χ' or χ'') of the dynamic magnetic susceptibility [36]. All our measurements are normalized by static hysteresis loops. Thus only non-thermal excitations of the magnetization are detected in units of M_s. For the measurements shown in Fig. 2.4 the microwave phase and frequency ($\omega_p = 2\pi \cdot 2.5$ GHz) are kept fixed while for the resulting resonance curves the magnetic bias field $\vec{H}_{\mathrm{B}}$ is swept for different amplitudes of the excitation field h_{rf}. When the excitation field is increased above a critical amplitude of 2 mT the main absorption shifts to lower fields. This effect is a consequence of the shift of the phase ϕ of the uniform mode above the threshold rf-field. In Fig. 2.4 c) we find phase shifts up to 35° at the small angle resonance field H_{FMR} when the excitation amplitude is increased.

Any magnetic excitation (coherent or incoherent) leads to a decrease of M_x of the order of $g\mu_B$, where g is the g-factor and μ_B the Bohr magneton. Therefore in order to be able to determine and separate (spatially) coherent and incoherent components of the excitation we perform an additional measurement that is sensitive only to M_x. For this the X-ray beam is rotated by 90° around the z-axis ($\varphi = 0°$), the rf-signal is not phase-locked to the X-ray bunches and in order to allow for lock-in detection the amplitude of the rf-excitation is modulated (Fig. 2.3). The signal is calibrated again by XMCD hysteresis loops resulting in $\langle \Delta M_x \rangle$ in units of M_s.

The detected decrease of the longitudinal magnetization component $\langle \Delta M_x \rangle$ is proportional to the total number $N_k = n_k V$ of non-thermal magnons excited in the sample volume V [37]. On the other hand $N_0 = N_{k=0}$ can also be calculated from the coherent measurement of M_y in the linear excitation regime.

$$N_0 = \frac{\Delta E}{\hbar\omega_p} = \frac{V\mu_0 H_B}{2M_s\hbar\omega_p}|M_y|^2 \tag{2.7}$$

Thus the reduction of the longitudinal magnetization per magnon is found to be approximately 5.5 $g\mu_B$. This large value is due to the highly elliptical precession $\left(\epsilon := \frac{|My|}{|Mz|} \approx 11\right)$ and in agreement with $\frac{1}{2}(\epsilon + \epsilon^{-1})g\mu_B$ expected from linear spin wave theory (following the procedure on pages 199-201 of [38]). There the energy $n\hbar\omega$ of n magnons is equated to the classical high frequency energy described by the transverse magnetization components and this relation is used to calculate the reduction of the longitudinal magnetization per magnon.

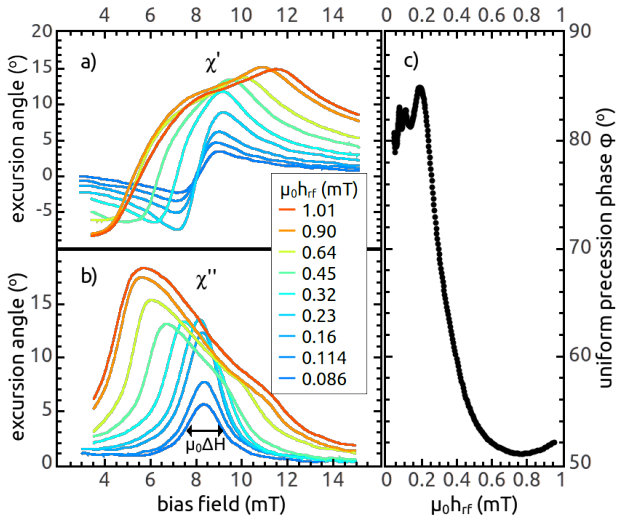

Figure 2.4: FMR resonance curves for in-phase a) and out-of-phase b) precession corresponding to the real and imaginary parts of the susceptibility. The main absorption proportional to the imaginary part is clearly shifted to lower fields as soon as a critical excitation level is reached [35]. The main mechanism limiting growth of the precession amplitude with an increasing driving field is a shift in the phase of the precessing magnetization c). It arises from effective driving fields due to non-uniform spin wave modes [25].

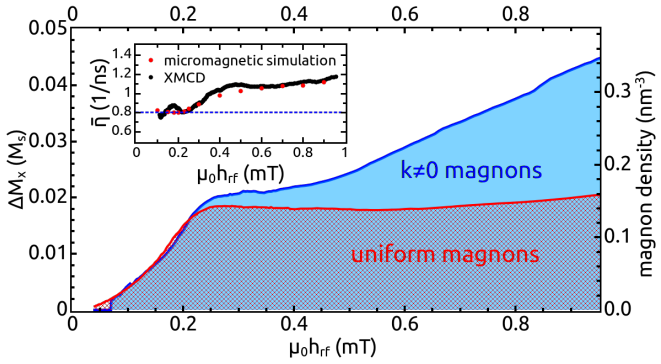

Figure 2.5: The decrease of the longitudinal magnetization ($\Delta M_x = M_s - M_x$) with growing excitation power measured for $H_{\mathrm{bias}} \approx H_{\mathrm{FMR}}$. The blue line shows the measured ΔM_x which is proportional to the total number of magnons excited. ΔM_x corresponding to uniform precession (red line) is calculated from the coherent M_y components. Above the threshold the total number of uniform magnons locks close to its threshold value whereas the number of non-uniform magnons $n_{k\neq 0}$ (blue area) increases with h_{rf}. When a second order Suhl instability is assumed ($\omega_k = \omega_0$), the average relaxation rate $\bar{\eta}$ increases significantly (inset).

In Fig. 2.5 we show the power dependence of ΔM_x directly measured in the time averaged $\langle M_x \rangle$ experiment and compared to the time resolved $M_y(t)$ measurement. In the linear regime both curves coincide and the total magnon population is composed only of uniform $k = 0$ magnons. Above a critical rf-field of 0.2 mT these curves begin to separate, due to saturation of the uniform magnon occupation density n_0 and the excitation of higher k magnons in the nonlinear regime [39, 24, 40]. The difference between the curves corresponds to $k \neq 0$ spin wave excitations.

2.3.2 Energy relaxation

The saturation of the homogeneous mode (Fig. 2.5) is closely connected to an increased relaxation rate when additional damping channels open up due to nonlinear coupling of the uniform mode to nonuniform spin waves. In this regime the energy pumped into the homogeneous mode by the rf-excitation is only partly relaxed by intrinsic uniform mode damping. In fact, a significant portion of the energy is distributed to non-uniform modes by additional magnon-magnon scattering processes and subsequently relaxed by intrinsic damping.

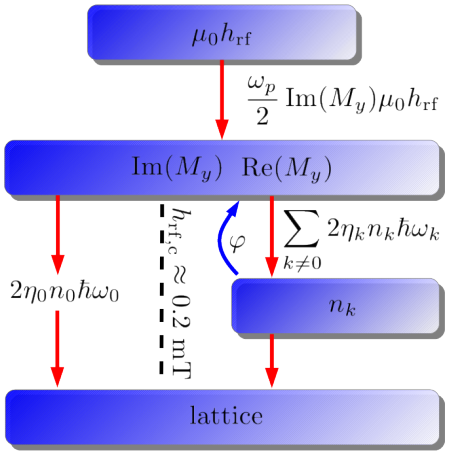

Figure 2.6: At first the energy flows from the driving field into the uniform mode which we detect by the amplitude of its transverse in-plane component (Re and Im). Intrinsic damping leads to a relaxation of the energy inherent in the uniform mode into the phononic system. The relaxation time is determined by linear FMR measurements. Above the critical excitation field amplitude of about 0.2 mT non-uniform spin wave modes are also excited. They react back on the uniform mode by changing the phase angle φ between the uniform precession and the driving field. Their energy is also released into the lattice and together with the uniform energy relaxation must equal the energy pumped into the magnetic system. Therefore this contribution to the energy relaxation can be determined when the other two contributions are known.

The energy pumped into the magnetic system (Fig. 2.6) must equal the energy damped out of the magnetic system by the intrinsic damping of the

dynamic modes [41]:

$$\frac{\omega_p}{2}\,\mathrm{Im}(M_y)\mu_0 h_{\mathrm{rf}} = 2\eta_0 n_0 \hbar\omega_0 + \sum_{k\neq 0} 2\eta_k n_k \hbar\omega_k \tag{2.8}$$

where $n_{0,k}$ are the magnon densities and $\hbar\omega_{0,k}$ and $\eta_{0,k}$ the magnon energy and relaxation rates of their precession amplitudes. At the FMR condition ($\omega_p = \omega_0$) only uniform magnons are directly pumped and all other magnons (with density $n_{k\neq 0}$) are indirectly excited through nonlinear processes. When we assume the latter to be second order Suhl instability processes ($\omega_k = \omega_0$), the inset of Fig. 2.5 shows an increase in the average relaxation rate $\bar{\eta}$ compared to the relaxation rate of the uniform mode ($\eta_0 \approx 0.8$ ns^{-1} at $\omega_p = 2\pi\cdot$ 2.5 GHz), which we extract from the measurements at low rf-power. This increased relaxation rate is unexpected since microscopic theory of magnetic damping [42] does not predict a strong dependence of the Gilbert damping constant α on the wave vector for the parameters of our and similar experiments. Micromagnetic simulations ($\alpha_k = \alpha_0$) reproduce our measurements (subsection 2.6) and thus also speak against an increased damping parameter.

2.3.3 Analytic model

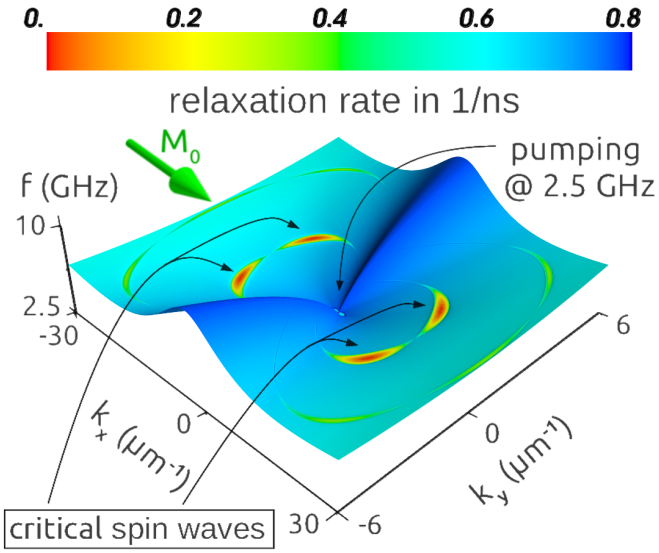

Figure 2.7: Precession frequency (z-axis) and relaxation rate (color scale) as a function of the in plane wave vector at an excitation field slightly above the threshold at which the first pair of spin waves ($k_{\mathrm{crit.}} \approx (\pm 9.4, \pm 2.4)$ μm^{-1}) becomes unstable. The resonance frequency of spin waves in certain arch-like regions around $\frac{3}{2}$, 2, ... ω_p become frequency-locked already well below the threshold. The instability first occurs in those regions. In addition spin wave frequencies over the whole spin wave manifold are shifted. This shift is most pronounced in the direction of the static magnetization, where it is positive and of the order of 500 MHz.

In order to unravel the physical origin for this discrepancy and to gain insight into the physics involved we performed numerical calculations. We start with the Landau-Lifshitz-Gilbert (LLG) equation.

$$\frac{d\vec{m}}{dt} = -\gamma\mu_0\vec{m} \times \vec{H}_{\text{eff}} + \alpha\vec{m} \times \frac{d\vec{m}}{dt} \tag{2.9}$$

The magnetization dynamics may be well approximated by a macrospin representing the uniform mode, even when a linearization of the LLG equation is no longer sufficient. As the non-uniform modes are not directly driven by the external field, their amplitudes are small (at the thermal level). Hence we restrict our considerations to linear terms in the spin wave amplitude m_k and write the equation of motion for the transverse components in matrix form [43, 28]:

$$\begin{pmatrix} \dot{m}_y^k \\ \dot{m}_z^k \end{pmatrix} = \begin{pmatrix} D_{11}(t) & D_{12}(t) \\ D_{21}(t) & D_{22}(t) \end{pmatrix} \begin{pmatrix} m_y^k \\ m_z^k \end{pmatrix} \tag{2.10}$$

Straight forward transformations (subsection 2.5) allow to demonstrate the physical meaning more clearly. First, the separation of both transverse coordinates from each other leads to the differential equation of a parametric oscillator for spin wave amplitudes m^k

$$\ddot{m}_y^k + \beta(t)\dot{m}_y^k + \omega^2(t)m_y^k = 0 \tag{2.11}$$

and one can see the parametric nature of the instability processes. By further appropriate algebraic transformations we obtain from eq. 2.11:

$$\ddot{f} + \Omega'^2(t)f = 0 \tag{2.12}$$

with a time periodic function $\Omega'^2(t)$. This equation is similar to the Schrödinger equation describing a quantum particle in a 1D periodic potential [44]. As a first approximation one can rewrite the parametric oscillator equation in the form of the Mathieu equation, which has been extensively studied due to its significance for quantum particles in a periodic potential [45]:

$$f'' + (a - 2q\cos(2x))\, f = 0 \tag{2.13}$$

While for a quantum particle the amplitude and phase of a wave function oscillate with the spatial period of the potential, the parametric spin wave behaves in a similar manner in the time domain. A numerical evaluation of equation (2.13) for different in-plane wave vectors and microwave excitation amplitudes is easily done with standard mathematical software. It provides us with the critical modes as well as wave vector dependent nonlinear frequency shift and relaxation rates (Fig. 2.7).

A fundamental finding from the model is that the excited spin waves do not precess at the driving frequency as expected for the 4-magnon scattering processes that usually lead to 2nd order Suhl instability [29, 46, 47]. Instead we find that the spin waves precess non-monochromatically at frequencies that are half-integer multiples of the driving frequency with additional oscillations of their amplitude and phase with the driving frequency (see Fig. 2.8 a). This magnetization behavior has to our knowledge not been described before and we believe that these nonlinear processes explain the observations of several groups under similar experimental conditions [48, 49, 50].

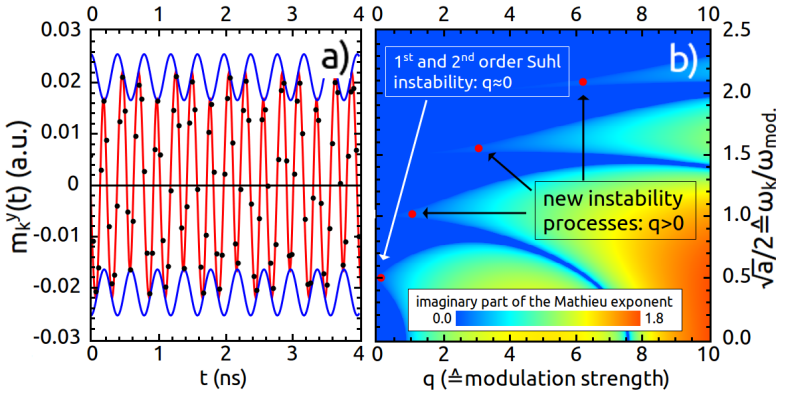

Figure 2.8: The instability diagram of the Mathieu equation b) shows the relation between Suhl instability processes and the instability processes described here. While the first processes constitute the special case of vanishing modulation, the latter processes are characterized by a significant modulation of the instantaneous resonance frequency $\Omega_k(t)$ for the critical spin wave mode a). In our experiment the large angle precession of the uniform mode modifies the effective field for non-uniform spin waves at a frequency $\omega_{\text{mod.}} = \omega_p$ leading to the instability of spin waves with a mean frequency of $\omega_k = 3/2\ \omega_p$. In contrast to much slower incoherent oscillations found for example in [51], this leads to fast (and coherent) oscillations of the spin wave's amplitude and phase a) with the frequency of the modulation.

Using eq. 2.13 the instability processes can be categorized by the parameters a and q. Where $a \hat{=} (2\omega_k/\omega_{\mathrm{mod.}})^2$ and ω_k is the mean frequency of the spin wave and $\omega_{\mathrm{mod.}}$ the frequency of the modulation and parameter q is the modulation strength. Thus we can calculate an instability diagram of the Mathieu equation in Fig. 2.8 b). In this representation Suhl instability processes turn out to be the special case of small modulation. I.e. Suhl instabilities are characterized by an almost constant and thus well defined resonance frequency for the critical modes and the energy conservation which is assumed in Suhl instability processes is valid. On the other side the strong modulation of the resonance frequency for other instability processes destroys the invariance under time translations and thus the energy (and frequency) is only well defined modulo multiples of the driving frequency.

In conclusion here we investigated the nonlinear magnetization dynamics of a thin Permalloy film at low magnetic bias fields. Our analysis led to a description of parametric excitations and to the experimental discovery of new classes of spin wave instabilities that turned out to be the dominant nonlinear processes at low fields.

2.4 Frequency shift

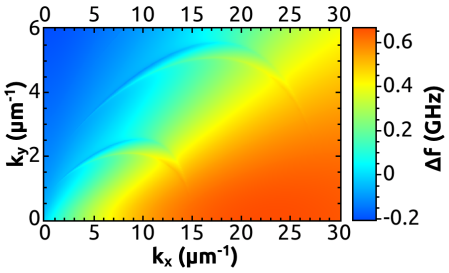

Figure 2.9: Nonlinear frequency shift for a critical excitation field of 0.2 mT. It shows strong up-shift (0.5 GHz) for spin waves in the BV-direction and a decrease in the resonance frequency for spin waves with a wave vector in the DE-direction.

The reason why Suhl instabilities are not observed at low bias fields is connected to the nonlinear frequency shift and will be discussed later in more detail (subsections 2.6 and 2.8.1). In Fig. 2.9 we show the nonlinear frequency shift for spin waves at the critical excitation field as obtained from our model. It can be understood by the following rough considerations:

The instantaneous resonance frequency $\omega_k(t)$ depends on the angle between the wave-vector k and the uniform magnetization direction $\vec{M}(t)$.

$$\begin{aligned}\omega_k(t) &\approx \omega_k(\vec{M}(t)) \approx \omega_k(\vec{M}_0 + \vec{m} \cdot \sin(\varphi(t))) \\ &\approx \omega_k(\vec{M}_0) + \frac{\partial \omega_k}{\partial \varphi} \cdot \vec{m} \sin(\varphi(t)) + \frac{\partial^2 \omega_k}{\partial \varphi^2} (\vec{m} \sin(\varphi(t)))^2 \qquad (2.14)\end{aligned}$$

$$\langle \omega_k(t) \rangle_t \approx \omega_k(M_0) + \frac{1}{2} \frac{\partial^2 \omega_k}{\partial \varphi^2} \cdot m^2 \qquad (2.15)$$

From this hand waving estimate we can see that the nonlinear frequency shift should be positive in BV-direction and negative in DE direction according to the second derivative of the dispersion relation with respect to the angle between the wave vector and the uniform magnetization (φ). And the shift should scale with the square of the cone angle of the uniform precession which was verified in micromagnetic simulations. Note that in [52] the authors investigated the nonlinear frequency shift of the uniform mode and found that its sign depends on the applied static magnetic field. As their experiments have been conducted on 300 nm thick $Ni_{80}Fe_{20}$ films and the shift is in the opposite direction as in our own measurements with much thinner films, one can conclude that even the sign of the nonlinear frequency shift can change with film thickness.

2.5 Theoretical model: Mathieu equation

We start with the LLG equation in the following form:

$$\dot{\vec{M}} = -\gamma\mu_0\vec{M} \times \vec{H}_{\text{eff}} + \frac{\alpha}{M_s}\vec{M} \times \dot{\vec{M}} \tag{2.16}$$

with $\vec{M} = M_0\hat{e}_x + \vec{m}_0 + \vec{m}_k$, where we assume $M_0 > |\vec{m}_0| >> |\vec{m}_k|$, i.e. the uniform precession $\vec{m}_0$ is smaller than the static uniform magnetization and the non-uniform dynamic magnetization $\vec{m}_k$ is much smaller than $\vec{m}_0$. $\vec{H}_{\text{eff}}$ is the effective field consisting of the external field, the exchange field ($\vec{h}_{\text{exch}} = 2Ak^2/(\mu_0 M_s)$) and the dipolar field ($h^k_{\text{dip.,i}} = N^k_{i,j}m^k_j$). Here we use a thin film approach [43] for the dipolar tensor $N^k_{i,j}$ instead of the more complicated expressions that we use for the analysis of parametric instability in thicker films [28]. To first order in the non-uniform spin wave amplitudes we find an equation of the form:

$$\begin{pmatrix} \dot{m}^k_y \\ \dot{m}^k_z \end{pmatrix} = \begin{pmatrix} D_{11} & D_{12} \\ D_{21} & D_{22} \end{pmatrix} \begin{pmatrix} m^k_y \\ m^k_z \end{pmatrix} \tag{2.17}$$

with time dependent components D_{ij}. The coupled coordinates can be separated by applying a time derivative. The result for m^k_y looks as follows (where we dropped the superscript):

$$\ddot{m}_y + \beta(t)\dot{m}_y + \omega^2(t)m_y = 0 \tag{2.18}$$

with $\beta(t) = -trD - \dot{D}_{12}/D_{12}$ and $\omega^2(t) = det(D) - \dot{D}_{11} + D_{11}\dot{D}_{12}/D_{12}$. This form corresponds to the differential equation for a parametric oscillator. By substituting

$$q = e^{d(t)}m_y(t) \tag{2.19}$$

with $d = \frac{1}{2}\int \beta(t)dt$ we can eliminate the damping term:

$$\ddot{f} + \Omega'^2(t)f = 0 \tag{2.20}$$

with $\tilde{\Omega}^2(t) = \omega^2 - \frac{1}{2}\dot{\beta} - \frac{1}{4}\beta^2$. Now we introduce the dimensionless parameter $x = \omega_p t/2$ and assume that $\tilde{\Omega}^2(t)$ varies periodically with the frequency ω_p. One thus obtains:

$$f''(x) + \Omega^2 f(x) = 0 \tag{2.21}$$

where we use $\Omega^2 = (4\omega^2 - 2\dot{\beta} - \beta^2)/\omega_p^2 \approx a - 2q\cos(2x)$ in order to find approximate solutions. This assumption only implies that the time dependent

modulation of the parametric oscillator is sinusoidal with a single frequency (for example the driving frequency ω_p).

Equation (2.21) can then be written in the form of the Mathieu equation:

$$f'' + \underbrace{(a - 2q\cos(2x))}_{\tilde{\Omega}^2} f = 0 \tag{2.22}$$

According to Floquet's Theorem [53] the solutions of this equation are of the form:

$$F(a, q, x) = e^{i\nu x} P(a, q, x) \tag{2.23}$$

where the complex number $\nu = \nu(a, q)$ is called the Mathieu exponent and P is a periodic function in x (with period π). As a and q depend on the parameters of the spin wave, so does ν. From the knowledge of ν for a spin wave, we know its behavior as a function of time: For example as soon as the imaginary part of $\nu\frac{\omega_p}{2}$ exceeds the exponent in equation (2.19) the spin wave becomes critical. Furthermore the real part of $\nu\frac{\omega_p}{2}$ gives the frequency of the spin wave. Due to the importance of equation (2.21) it was extensively studied [45] and it is well understood for special shapes of the 'potential' $\tilde{\Omega}^2$. While the case of a constant $\tilde{\Omega}^2(t)$ just describes the spin wave amplitude without any modulation, taking the next term in a Fourier expansion of $\tilde{\Omega}^2(t)$ into account is sufficient to qualitatively explain the instabilities found in the numerical calculations (Fig. 2.7). In order to very quickly find the dispersion and the lifetimes of all possible spin wave modes the parameter ν is evaluated as a function of k_x and k_y. As basically all modes are independent from each other it is also easy to implement the numerical procedure for parallel execution on a graphics card using cuda technology [18] and integrate the equation of motion (eq. 2.17) directly with a Runge-Kutta integrator. This procedure results in data like those shown in Fig. 2.7 and Fig. 2.9. Although there are differences between results from the evaluation of equation 2.17 and the Mathieu equation, the latter is still a good approximation in many cases and serves as the simplest model to classify the instability effects.

In thicker films or more complicated structures when the eigenmodes are not known a priori it is necessary to take more than one spin wave mode into account. Nevertheless the equation of motion can be written in the same form as in (2.17) and (2.18), but with D_{ij} being n×n-matrices instead of scalars and $\beta(t)$ and $\omega^2(t)$ also being n×n-matrices: $\beta(t) = -D_{11} - D_{12}D_{22}D_{12}^{-1} - \dot{D}_{12}D_{12}^{-1}$ and $\omega^2(t) = D_{12}D_{22}D_{12}^{-1}D_{11} - D_{12}D_{21} - \dot{D}_{11} + \dot{D}_{12}D_{12}^{-1}D_{11}$. Where n is the number of transverse modes. A projection onto the linear eigenmode's y-component of the matrix D finally leads to the equation of a one dimensional parametric oscillator equivalent to the case of $n = 1$ discussed before.

2.6 Micromagnetic modeling

Micromagnetic simulations that confirmed our conclusions were performed using the open source GPU based code Mumax [17]. The simulated sample volume is 80 μm × 20 μm×30 nm. Time traces of 500 ns were computed to extract the numerical values. Standard parameters for $Ni_{80}Fe_{20}$ were used in the simulations: saturation magnetization $M_s = 8 \times 10^5$ A/m, damping constant $\alpha = 0.009$, and

exchange constant $A = 13 \times 10^{-12}$ J/m. For our sample we were able to reproduce the critical excitation fields and magnon densities above the threshold quite accurately (Fig. 2.5) as well as nonlinear susceptibility curves. Furthermore we actually found the amplitude phase oscillations in simulation data as a frequency comb in the in-plane magnetization at a certain wave-vector. The wave vector in DE-direction is quite small so the simulation volume has to be sufficiently large in this dimension.

Well above the threshold interactions between the non-uniform spin waves lead to the generation of spin waves with the sum and difference wave-vectors resulting in fascinating magnetization dynamics in real space.

The dispersion relation just below the critical excitation amplitude has also been simulated and compared to the one without uniform excitation. This was achieved by evaluating Fourier transforms in time and space of thermally (randomly) excited spin wave modes. In Fig. 2.10 a) a distribution of spin wave amplitudes (of the transverse in-plane component) is shown for the 2.5 GHz frequency component. Due to the shallow dispersion relation and the limited frequency resolution (only 0.1 GHz in this case) the iso-frequency line is not clearly visible as a line but as the bright region extending from $k = 0$ to approximately $k_{\mathrm{BV}} \approx 5\ \mu\mathrm{m}^{-1}$. The second bright region is a numerical artifact probably coming from numerical instabilities of the gpu-software that only uses single precision arithmetics. Numerical instabilities have been observed for dynamic simulations and spin waves with a wavelength comparable to the cell-to-cell spacing. The instabilities did neither lead to divergence of the short wavelength spin waves nor to major perturbation of results for the long wavelength spin waves. The simulation was repeated with an additional rf-field term that was driving the uniform mode. In Fig. 2.10 b) - d) the spin wave amplitude distribution is shown for increasing uniform driving field amplitudes $\mu_0 h_{\mathrm{rf}}$ of 0.05, 0.10 and 0.15 mT and the one for no driving (Fig. 2.10 a) is already subtracted.

The appearance of a lobe which becomes stronger with increasing rf-amplitude is observed. This iso-frequency line is not at 2.5 GHz, but at 5 GHz and it can be seen as 'sidebands' of spin waves that precess at 5 GHz, 7.5 GHz, ... with amplitude-phase oscillations. Parts of the 7.5 GHz iso-frequency line can also be seen. With increasing rf-amplitude the extent of the iso-frequency lines in BV-direction decreases, i.e. for a spin wave with fixed k-vector in BV-direction the eigenfrequency is shifted to lower frequencies in agreement with Fig. 2.9.

In Fig. 2.11 we show results of the Fourier analysis for the driving with 0.2 mT, i.e. just above the threshold. For those simulations thermal excitations (through a random field) were used and the simulation time was more than 300 ns to reach an above threshold equilibrium state. After 300 ns images of the magnetization configuration were recorded for 32 ns for later Fourier analysis. Fig. 2.11 c) can be directly compared to Fig. 2.10 where we saw the 5 GHz iso-frequency line which is apparent when we compare it with Fig. 2.11 e). In Fig. 2.11 d) we observe the fundamental critical spin wave modes at wave vectors that agree very well with those we found earlier ($k_{\mathrm{crit.}} \approx (\pm 9.4, \pm 2.4)\ \mu\mathrm{m}^{-1}$, Fig. 2.7). We see the direct trace of the amplitude-phase oscillations also for the critical modes (compare Fig. 2.11 b and d) as well as linear combinations of the critical wave vectors in the spatial Fourier images. Finally in Fig. 2.11 f) we verify that the parametrically excited spin waves precess exactly at half integer multiples of the driving frequency by plotting the spin wave amplitudes summed over the whole k-plane as a function of its Fourier-frequency.

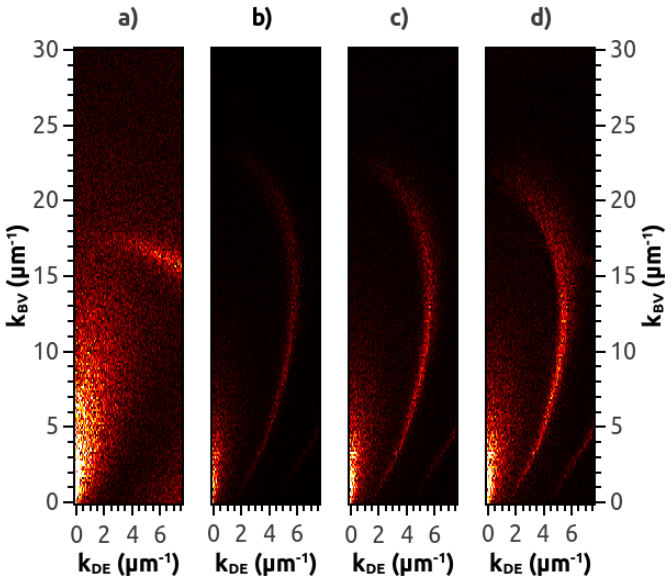

Figure 2.10: Distribution of spin wave amplitudes at the 2.5 GHz Fourier frequency for zero uniform driving field in a) and 0.05, 0.10 and 0.15 mT driving amplitudes (b - d). The reference (with no excitation) has been subtracted from the other images and the same linear color-map has been used for all four images.

The sharp peaks that show clear contrast against the background of 'thermal' spin waves (which is similar to those observed in the simulations for Fig. 2.10) provide sufficient evidence for the coherence of the magnetization oscillations as α was 0.008 in this case and natural linewidths would be expected in the 200 MHz range which is much broader than the lines in Fig. 2.11 f) which are still limited by the frequency resolution (1/32 ns $\approx$ 30 MHz) of our simulations.

2.6.1 Edge effects and out-of-plane magnetized structures

While we only considered infinite films so far, where plane waves are the linear spin wave eigenmodes we report here effects at the edges of the film as they appear in every real sample. We do this quickly for in-plane magnetized films, i.e. the case that we considered so far, and give an outlook for parametrically excited spin waves for out-of-plane magnetized structured thin films. We use micromagnetic simulations in both cases as our major tool.

In simulations for a rectangle instead of the infinite plane film (rectangle with 2D periodic boundary conditions) we find that the finiteness plays a role only within a few micrometers to the edges. This is probably due to the small thickness of the film (30 nm), i.e. the dipolar fields are strong enough to cause a clearly visible effect only within a relatively short range. Furthermore because of the reciprocity of the spin wave dispersion for counter-propagating modes it is expected that the nodes of their interference pattern should not move (after a long enough time and not too far above the nonlinear threshold). For in-

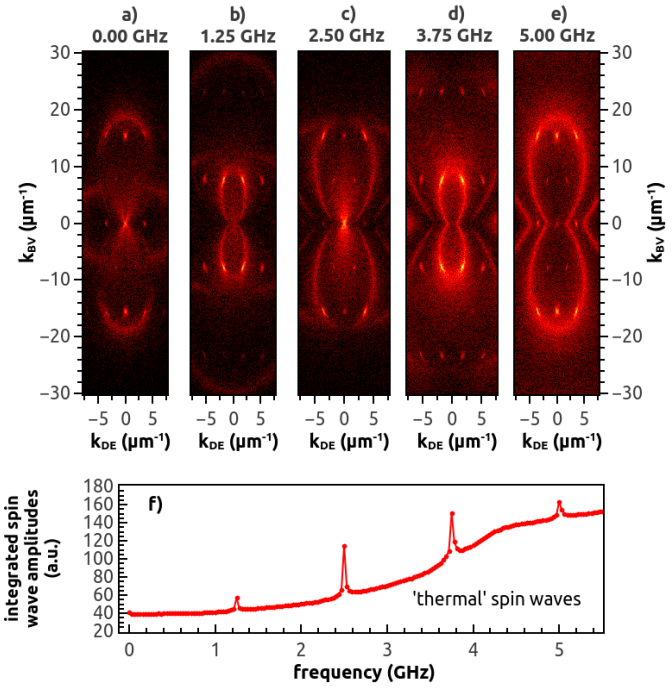

Figure 2.11: As in the simulations for Fig. 2.10 the simulations were done on a 1024×1024 cell grid with rather large cells of $100 \times 100 \times 30$ nm to achieve a reasonable resolution in k-space and therefore the exchange interaction was probably not taken into account correctly. A logarithmic color-map was used for all five sub-figures in order to see thermal spin wave amplitudes and parametric spin wave amplitudes in the same figure. Iso-frequency lines and critical spin waves' main frequencies can be seen in c) to e) and its traces, i.e. 'sidebands' due to the amplitude-phase oscillations in a) - c). The spin wave amplitudes summed over the whole k-plane can be seen in f).

plane magnetized films this should not change because of the reciprocity of the scattering process for a spin wave with the edge or with defects. And so far we did not observe unexpected behavior with this respect.

The situation changes when the dispersion relation is no longer symmetric. This is the case when spin transfer torque acts on spin waves and slightly shifts their eigenfrequencies depending on the propagation direction of the spin wave with respect to the direction of the spin polarized current (see 3.3).

In this case the interference pattern is expected to shift with the spin drift velocity $u = \frac{jPg\mu_B}{2eM_s}$.

For out-of-plane magnetized structured films the scattering process of a magnon with the edge or a defect is no longer reciprocal due to the Berry curvature Ω [54]. This phase difference might lead to a shift of the interference pattern. This means for example that the pattern shifts in opposite directions at opposing edges of the sample (magnon edge current) when the interference pattern is not hindered to do so. We observed this effect as the rotation of the interference pattern around the center of an out-of-plane magnetized disk and a ring.

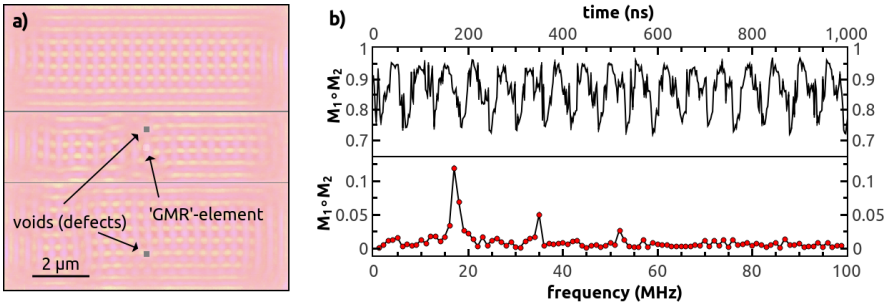

Figure 2.12: a) The interference pattern of parametrically excited spin waves align with the edges of the out-of-plane magnetized structure and disappear only within approximately one micrometer to the edges. This allows the interference to be moved. Besides the edges we introduced two defects (voids) in order to get a feeling about the pinning behavior of the pattern. In the middle of the square a stripe has been separated from the rest by removing the magnetic material on two lines. A spin polarized current is then sent through this stripe and the magnetization underneath a small disk (mimicking a GMR sensor) is plotted as a function of time in b). The time trace and its spectrum clearly show that the interference pattern is moving due to the spin transfer torque.

Fig. 2.12 exemplifies some of the points already discussed on an out-of-plane magnetized $Ni_{80}Fe_{20}$ (1.086 T out-of-plane field, $\mu_0 M_s = 1.0$ T) rectangle (10×10 μm^2) with 48 nm thickness excited with an in-plane rotating excitation field of 10 mT amplitude and 5 GHz frequency. The rectangle is further patterned into three stripes. Fig. 2.12 a) shows a snapshot of the magnetization after 1 μs simulation time. The interference pattern is clearly visible apart from the surrounding of the edges. In this case the interference pattern did not move by itself, but was pinned, not only by the defects we modeled as voids, but also in the upper stripe.

A spin polarized current ($P = 0.65$) of $1.8 \cdot 10^{11}$A/m^2 sent only through

the middle stripe was able to move the interference pattern in this stripe in one direction. Fig. 2.12 b) shows a trace of the dot product of the normalized magnetization M_1 of a small circular disk (8 nm thick) placed 8 nm above the patterned film and the magnetization underneath it (M_2) mimicking a magneto resistive sensor element to read out the local magnetization. It clearly shows periodic oscillations with a frequency of approximately 17 MHz that correspond to the shift of the interference pattern by one wavelength. Reducing the current density leads to pinning at approximately $5 \cdot 10^{10}\mathrm{A/m}^2$ for this case.

For a ring structure with similar dimensions and parameters we found rotating interference patterns even without spin polarized currents due to the magnon Berry phase.

2.6.2 Thermal effects

In Fig. 2.5 the uniform magnon density deviates from its expected parabolic excitation field dependence already before it locks to its threshold value resulting in a rounded kink. As discussed earlier the measurements have been carried out at room temperature and the dynamic magnetization was normalized by the room temperature saturation magnetization and therefore only non-thermal magnons are detected although magnons are present in the sample at any excitation power. However, our numerical studies show that relaxation rates are reduced for magnons in arch like regions (Fig. 2.7) already below the threshold. I.e. energy is pumped into non-uniform modes resulting in additional relaxation of the uniform mode and the observed kink. Alternative explanations that could also cause the rounded kink would be spatial inhomogeneities of the sample or the excitation field leading to a distribution of thresholds across the sample.

2.7 Side-notes

2.7.1 Sample preparation

The samples are composed of a metallic film stack grown on top of a 100 nm thick Si_3N_4 membrane supported by a silicon frame in order to allow transmission of X-rays. The film system was patterned into a coplanar waveguide by lithography and lift-off processes. The $Ni_{80}Fe_{20}$ layer is isolated from the 160 nm thick copper capping layer by a 5 nm thick film of Al_2O_3. The isolation layer and the low conductivity of the $Ni_{80}Fe_{20}$ ensure that 99% of the rf-current flow in the Cu layer leading to a well defined in-plane rf-excitation of the sample. The driving field is oriented along the y-direction (see Fig. 2.13) perpendicular to the external dc field (transverse pumping). Cooling of the magnetic sample on the Si_3N_4 membrane inside the vacuum chamber is achieved by a Helium atmosphere of 200 mbar.

2.7.2 X-ray magnetic circular dichroism

X-ray magnetic circular dichroism is measured in absorption at the Fe L_3 absorption edge. A typical spectrum of our samples is shown on the left in Fig. 2.14. The dichroic component of the signal is proportional to the magnetization component parallel to the beam. The size of the probed spot on the sample is defined by the width of the signal line of the coplanar waveguide structure (80

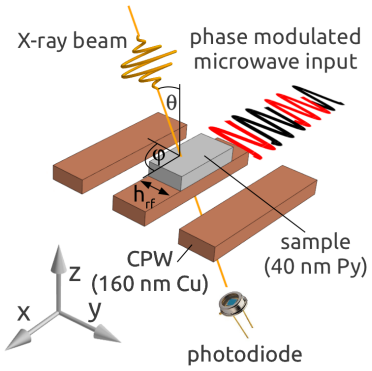

Figure 2.13: Geometry of the sample. The surface normal of the magnetic sample can be precisely oriented with respect to the k-vector of the X-rays. A microwave in-plane magnetic driving is generated by the signal line of the coplanar waveguide.

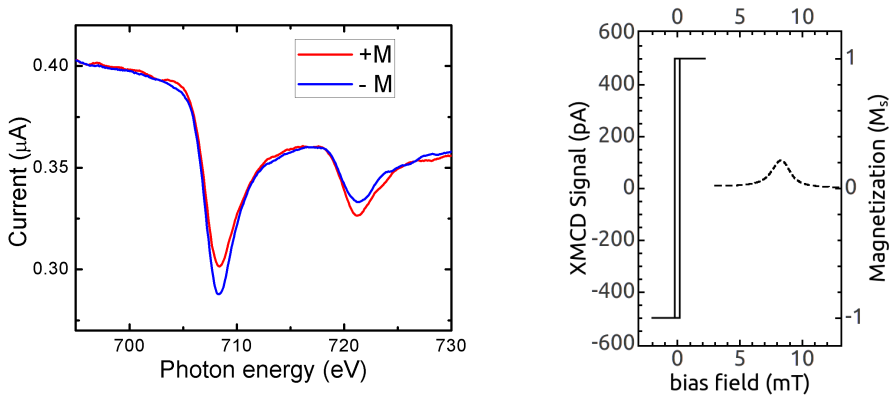

Figure 2.14: XMCD spectra. Left: X-ray absorption spectrum of the L_{23} edge recorded for two orientations of the magnetization in 40 nm thick $Ni_{80}Fe_{20}$. All dynamic (FMR) and static (hysteresis loops) measurements are performed at the X-ray energy where the dichroism is maximum (L_3 edge). Right: Normalization of the dynamic magnetization (dashed line) to the saturation magnetization M_s, which was determined by measuring static hysteresis loops (full line).

μm) and by the lateral dimension of the X-ray beam (900 μm). The transmitted X-ray intensity is detected by a photo-diode [55].

2.7.3 Microwave circuitry

The microwave excitation in the XMCD-FMR experiment is phase-synchronized with the bunch timing structure of the storage ring so that stroboscopic measurements are sensitive to the phase of the magnetization precession. Synchronization is ensured by a synthesized microwave generator, which uses the ring frequency of 500 MHz as a reference in order to generate the required rf frequency. The phase of the microwave excitation with respect to the X-ray pulses is adjusted by the signal generator. In order to allow lock-in detection of the XMCD signal the phase of the microwaves is modulated by 180° at a frequency of a few kHz. Due to the synchronization of the microwave signal and the X-ray bunches, the magnetization is sampled at a given constant phase. The amplitude of the modulated intensity is proportional to the dynamic magnetization component projected onto the X-ray beam, see Fig. 2.13. This signal is normalized by static XMCD hysteresis loops, see Fig. 2.14. The normalized signal is an absolute measure of the amplitude of the magnetization dynamics, evaluated as a fraction of the saturation magnetization or as the cone angle of the precession.

2.8 Thresholds for various cases: thickness dependence and YIG

Thresholds for several cases have been calculated numerically in order to investigate different aspects of the involved instability processes and to make sure that our numerical method is correct:

2.8.1 Thickness and frequency dependence

As mentioned earlier (section 2.4) the nonlinear frequency shift is the reason why the 2nd order Suhl instability process is not the one with the lowest threshold at low frequencies. Here we show more details to corroborate this claim. Therefore we evaluated numerically the rf-field amplitudes $h_{\text{crit.}}$ that are needed to compensate the damping for two kinds of spin waves, i.e. for those of the 2nd order Suhl instability and for those at $\frac{3}{2}\omega_p$. On the left side of Fig. 2.15 it is clearly visible that for frequencies below ≈ 5 GHz the $\frac{3}{2}\omega_p$ spin waves are excited before the 2nd order Suhl instability can set in. Above ≈ 6 GHz the 2nd order Suhl instability becomes the relevant instability process with the lowest threshold. In the transition region the 2nd order Suhl threshold sharply increases as a consequence of the positive nonlinear frequency shift for the critical spin waves. This frequency shift is more relevant at lower fields because the spin wave dispersion in BV direction becomes very shallow at low fields, i.e. low resonance frequencies. This decreases the k-vector of the critical spin wave significantly and its coupling parameter with the uniform mode W_k decreases as well (see [48] for a plot of W_k versus the frequency and reference 16 therein for a definition of W_k).

To further test this explanation we repeated the calculations with a film of 60 nm thickness, leaving other material parameters the same (right side of Fig. 2.15). For the thicker film the spin wave dispersion minima (pockets) are

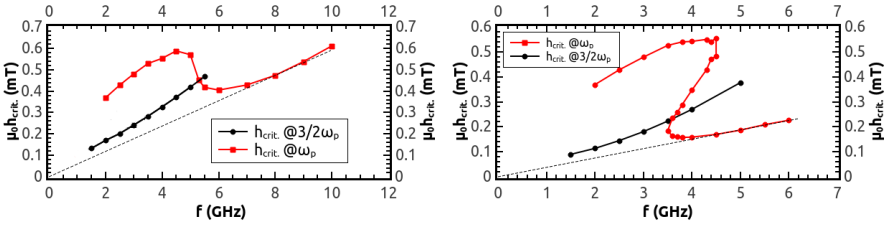

Figure 2.15: The critical rf-field amplitude as a function of the excitation frequency. Parameters are: $\alpha = 0.009$, $M_s = 8 \cdot 10^5$ A/m, and film thickness is 30 nm (left) and 60 nm (right). When the pump frequency is sufficiently low the threshold for the 2nd order Suhl instability (red line) increases above the critical driving field for the instability that generates spin waves at $\frac{3}{2}\omega_p$ (black line).

deeper, i.e. at lower frequencies, compared to the previous 30 nm film. Therefore the transition region is at lower fields/frequencies as expected and even a kind of fold-over threshold line is found for the 2nd order Suhl instability, i.e. two rf-field ranges of super critical behavior, one at low amplitudes with less nonlinear frequency shift and a second one for stronger shifts are found.

In [48] Gerrits et al. measured nonlinear FMR in a 20 nm thin Permalloy film by magneto-optical Kerr effect. The time averaged longitudinal magnetization of the sample is probed with a laser resulting in field swept curves of $\Delta M_z(H)$ for frequencies between 1.25 and 3.75 GHz. The authors define a critical pump field amplitude h_{crit} as the position of the kink in a plot of the maximum ΔM_z versus the pump field (Fig. 2 in [48]). This procedure is repeated for various frequencies resulting in a plot of h_{crit} versus the driving frequency. Furthermore the authors assume that the parametric spin waves are excited at the driving frequency in a second order Suhl instability process and find that the relaxation rate below 2.5 GHz is significantly lower than expected while above 2.5 GHz the relaxation rates agree with the uniform relaxation rate.

As the authors determine the relaxation rate by the use of

$$\eta_k = \frac{1}{2} \left(h_{\mathrm{crit}}/\Delta H_{\mathrm{FMR}}\right)^2 W_k \omega_m \tag{2.24}$$

one could directly conclude that below 2.5 GHz there is an instability process with a lower threshold than the second order Suhl instability for which the formula was calculated.

In order to verify this alternative conclusion we calculate thresholds and directly compare them with the experimental results (Fig. 2.16). We find that below a certain frequency spin waves at $\frac{3}{2}\omega_p$ have a lower threshold (by about a factor of 2) compared to the second order Suhl instability. From this result we claim that the relaxation rate that was determined in [48] is not correct for low frequencies and that the authors observed parametric instability of spin waves at $\frac{3}{2}\omega_p$.

Second order Suhl instability is dominant only for higher fields/frequencies. The cross-over between the two instability processes is at about 5.5 GHz in the calculations and seems to be lower (about 2.5 GHz) in the measurements.

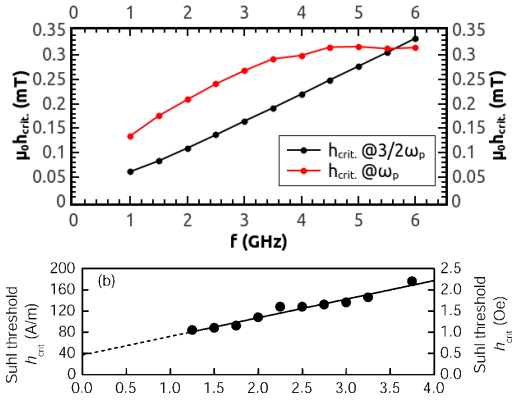

Figure 2.16: The critical rf-field amplitude as a function of the excitation frequency. The upper part presents our simulation with the following parameters: $\alpha = 0.006$, $M_s = 8 \cdot 10^5$ A/m, and a film thickness of 20 nm. For comparison we replicate the experimental results by Gerrits et al. [48] below our calculations.

Reasons for this difference could be thermal or disorder effects which are not included in the calculations. Another possible explanation lies in the complicated method the experimental thresholds have been determined with. Therefore in the next section we investigate the field dependence of the thresholds for a fixed frequency and answer the question if the threshold at the FMR condition is always lowest.

2.8.2 Butterfly-curves and 2-magnon-scattering

The threshold for the excitation of parametric spin waves $H_{\mathrm{rf,crit.}}$ depends on the external bias field H_{bias}. Naively it is expected to be lowest close to the ferromagnetic resonance field H_{FMR} and to increase once the bias field is detuned from resonance. Due to the shape of these curves they are called 'butterfly-curves'.

In Fig. 2.17 a) we calculated such curves for our sample (30 nm, $\alpha = 0.009$). The reason for the step-like increase at the high field side of the resonance is that the spin wave manifold is shifted above the FMR condition such that there are no spin waves that can be resonantly excited. For 6 GHz this happens still above the FMR field, while for 5 GHz and below this happens below the FMR field in agreement with Fig. 2.15 a).

For frequencies below 5 GHz the minimum of the butterfly-curve is even shifted away from the FMR field because of the non linear frequency shift, that shifts the spin wave modes in BV-direction, i.e. those that become critical, to higher frequencies and above the FMR condition.

Especially Olson et al. [46] measured butterfly-curves in Permalloy and therefore we reproduced these curves with our simulations (Fig. 2.17 d).

We find good general agreement with the measured ones. We used standard parameters for the simulations, i.e. a M_s of $8{\cdot}10^5$ A/m which is about 10% higher than the one determined in their measurements for the 104 nm thick sample

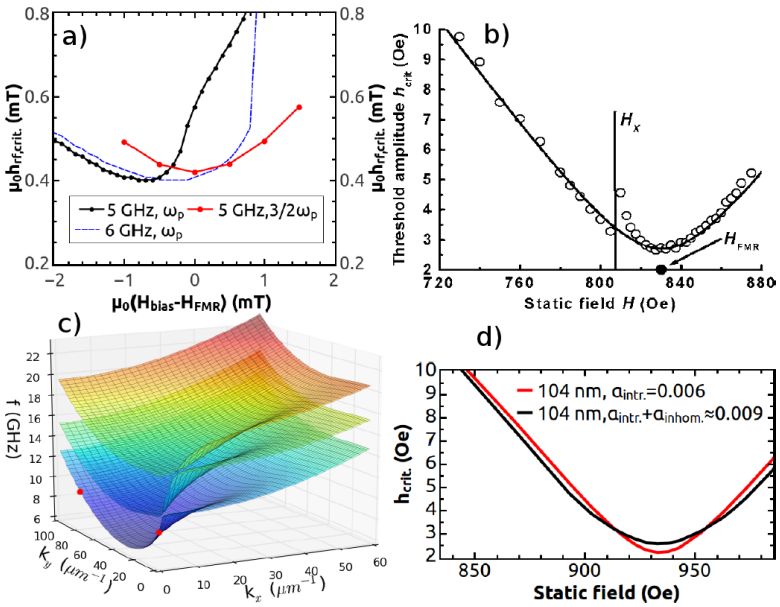

Figure 2.17: a) The calculated critical fields as a function of the detuning from the FMR condition are shown for a film of 30 nm thickness and $\alpha = 0.009$. The nonlinear frequency shift leads to an increase of the 2nd order Suhl threshold especially at and above the linear FMR resonance field. b) The experimental results of Olson et al. [46] are reproduced for comparison with our calculations on a 104 nm thick film excited at 9 GHz and shown in d). c) The dispersion relation for the three lowest spin wave branches for this sample at a bias field $\mu_0 H_y$ of 94.3 mT (943 Oe) is calculated using numerical diagonalization for the linear analysis following [28]. The uniform and the critical mode are marked with a red dot.

and explains why our resonance field is also about 10% higher. For the Gilbert damping parameter Olson et al. found 0.0093 from FMR measurement which has probably an extrinsic contribution which stems from sample inhomogeneities and broadens the FMR linewidth through 2-magnon-scattering processes. In such a 2-magnon scattering process a uniform magnon is scattered into a non-uniform mode by a sample inhomogeneity. While this process changes the wave vector of the magnon, its frequency stays the same. Therefore the uniform mode can only scatter into energetically degenerate states, i.e. into those at the iso-frequency lines of the spin wave dispersion. Characteristic quantities that can be extracted from 'butterfly'-curves are the width and the threshold amplitude at the minimum. The width is directly related to the width of the uniform mode as the 2nd order Suhl instability is driven by the uniform precession and the instability threshold depends on the uniform precession angle. The critical field amplitude also depends on the damping rate of the critical mode as the parametric pumping has to compensate the relaxation into the phonon system at the threshold. We find a good fit to the experimental data when we assume an intrinsic Gilbert damping parameter $\alpha_{\text{intr.}} = 0.006$ which is a typical value for good quality Permalloy together with an inhomogeneous contribution equivalent to $\alpha_{\text{inhom.}} = 0.003$ (Fig. 2.17 d). Note that this is consistent with $\alpha_{\text{FMR}} = \alpha_{\text{intr.}} + \alpha_{\text{inhom.}}$ and reproduces the minimum threshold amplitude and the width of the 'butterfly'-curve better than calculated curves which do not include the inhomogeneous effect. To be more precise, an intrinsic damping parameter of 0.009 shows a broader 'butterfly'-curve and a 'butterfly'-curve that gives good agreement in the width shows too small minimum thresholds as shown in the black curve in Fig. 2.17 d). The kink in the measured curve (Fig. 2.17 b) at H_x which is related to a qualitative change in the response as noted by Olson et al. is not reflected in our calculations of the threshold. Therefore we believe that this is an artifact of the way the threshold is determined.

2.8.3 Subsidiary absorption

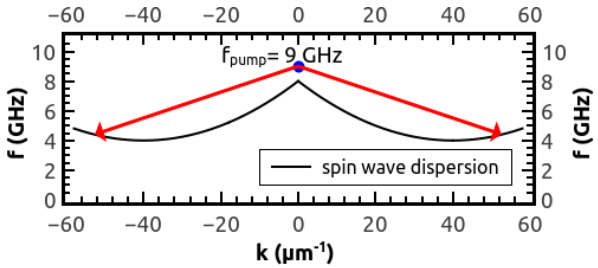

Figure 2.18: When the excitation of the FMR mode is off-resonance and spin wave modes at half the excitation frequency exist the first order Suhl instability can occur. In this instability process a uniform magnon with frequency f_{pump} splits into two non-uniform magnons at frequency $f_{\text{pump}}/2$ with opposing wave vectors. Because the dispersion relation for a thin film is shallow this type of instability is usually observed in thicker samples where the threshold can more easily be reached.

Another known type of spin wave instability is the so called subsidiary absorption, which manifests itself in an increased absorption well below the FMR field above a critical pump amplitude. An et al. [56] experimentally investigated such thresholds for Permalloy films of various thicknesses. Subsidiary absorption can be observed when the driving frequency is twice the resonance frequency of some spin wave mode. We want to show that our calculations also reproduce thresholds due to subsidiary absorption and in this context briefly discuss thick films, i.e. films where the wavenumber thickness product kd is no longer smaller than one and the validity of the thin film approximation has to be checked.

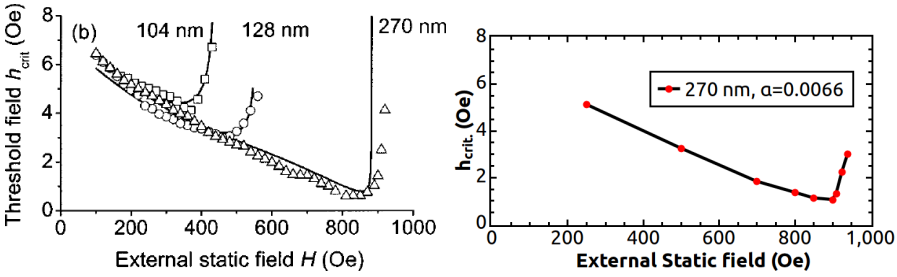

Figure 2.19: (left) An et al. [56] measured subsidiary absorption threshold curves and fitted numerically obtained curves to it. We performed threshold calculations on the 270 nm thick film (right) excited at 9 GHz and a Gilbert damping parameter $\alpha = 0.0066$ which can directly be compared to the experiments.

In Fig. 2.19 we reproduce the main experimental results of [56] shown on the left. The three curves represent the subsidiary absorption thresholds for three samples with different thicknesses of 104 (the same as used in [46]), 128 and 270 nm. All three samples have a FMR field of roughly 900 Oe. Due to their different thickness the spin wave dispersions show minima that reach to lower frequencies for the thicker films. Therefore one needs to apply higher bias fields to bring the spin wave with the lowest eigenfrequency into resonance (or in this case into parametric resonance at half the pumping frequency). For even higher fields the threshold is expected to increase because there are no more spin waves that can be parametrically driven within this instability process. The authors used a Suhl/Schlömann type analysis and calculated threshold curves numerically for this first order process. Under certain assumptions (including an angle dependent linewidth) they found reasonable agreement with the measurements (black lines on the left side of Fig. 2.19). Therefore they used the spin wave dispersion in the thin film approximation. The authors also note the difference between the two curves for 270 nm for fields above the minimum. In order to check the validity of the thin film approximation, the angle dependent linewidth and the behavior above the minimum threshold we performed our own calculations. Therefore we first numerically calculated the linear eigenmodes [28] of the thick film and continued as described before. Our calculated threshold curve for the 270 nm thick film shown on the right side of Fig. 2.19 agrees well with the experiments. The Gilbert damping parameter was $\alpha = 0.0066$ and equal for all spin waves. Therefore we can conclude that although the linewidth is wave vector dependent, the damping constant is still independent of the k-vector. Furthermore we find that the critical spin waves still belong to the lowest spin wave dispersion branch, although the branches are changed compared to the

non-interacting thin film approximation (Fig. 2.17 c). And above the minimum field (around 900 Oe) we find an increase in threshold that fits rather well to the experiment and is much less abrupt than in the numerical calculations by An et al. from which we conclude that it is important to take nonlinear frequency shifts consistently into account since in this case it seems to be the effect of frequency locking to half the driving frequency that takes place slightly below the spin wave manifolds minimum (linear) frequency.

Note that we also checked our calculations for the 104 nm film that was also used by Olson et at. [46] and found that the critical modes are still in BV-direction. Although the order of the spin wave modes changes for example in the lowest branch (Fig. 2.17 c): in BV (y-) direction $n = 0$ is the lowest mode while in DE (x-) direction $n = 1$ is the lowest frequency mode (for $|k| > 3 \cdot 10^6$ m^{-1}), where n is the number of nodes in the mode profile in perpendicular (z-) direction and was determined from the corresponding numerically calculated eigenmode profiles. In the thin film approximation only $n = 0$ is considered and in BV-direction this approximation is still valid and therefore the thresholds for 2nd order Suhl instability do not change significantly whether or not the thin film approximation is used.

2.8.4 YIG

frequency	thickness	H_c	$M_{y,\text{crit.}}$
10 GHz	20 nm	0.3 Oe	0.013 M_s
20 GHz	20 nm	0.3 Oe	0.04 M_s
10 GHz	2 μm	0.1 Oe	0.03 M_s

Table 2.1: Critical parameters for nonlinear FMR in YIG films.

Yttrium iron garnet (YIG) is a ferrimagnet with very small damping. Therefore it was the preferred material to study nonlinear magnetization dynamics and as a consequence most of the literature on nonlinear magnetization dynamics is about YIG. Because of its low damping it found its way into applications (YIG-filter). Typical material parameters are: $\mu_0 M_s = 0.175$ T, $l_{\text{ex.}} = 15.7$ nm and $\alpha = 0.0001$, which leads to thresholds of less than 0.5 Oe for thin films at 10 GHz and critical in-plane excursion angles of a few degrees. Table 2.1 shows some calculated threshold fields H_c and critical in-plane excursions $M_{y,\text{crit.}}$ of the uniform mode. Both are roughly an order of magnitude smaller than for $Ni_{80}Fe_{20}$.

2.9 Summary

In this section we investigated nonlinear effects in spin wave dynamics close to the threshold. This covered standard 1st and 2nd order Suhl instabilities in thin and thick $Ni_{80}Fe_{20}$ and in YIG, nonlinear frequency shifts, frequency locking and the experimental determination of magnon densities and magnon relaxation rates. Furthermore an alternative method of detecting small differences in the resonance frequencies of counter-propagating spin waves due to spin transfer torques or the magnon Berry curvature has been show in simulations.

Chapter 3

Spin waves in stripes

In this chapter we investigate propagating spin waves in stripes in the linear regime, i.e. small wave-like excitations of the magnetization moving along a stripe which is often called (spin wave) wave-guide in analogy to optical wave guides.

Various experiments use spin waves in thin magnetic wires to study spin wave modes [57, 58] or spin wave decay lengths [59]. As a consequence of lateral confinement in one direction quantized modes have been observed [57] as well as their superposition and constructive interference [60]. Due to the long range dipolar interactions and the anisotropic dispersion relation it is not trivial that spin waves can follow a curved wire, which was achieved using the additional magnetic field of an electric current following the wire structure [61]. When the current is flowing directly in the magnetic wire the current is spin polarized and interacts with propagating spin waves via spin transfer torques leading to a spin wave Doppler shift [62, 63, 64, 65, 66] which was detected mostly in propagating spin wave spectroscopy experiments [62, 63, 64, 65]. In these experiments cw-excited spin waves are measured nonlocally [62, 67] and the decay length of spin waves is the crucial parameter for the signal amplitude. To understand and control this parameter is highly desirable and therefore we studied spin wave propagation in a magnetic wire in detail [68] as well as their interaction with a spin polarized current [66].

While spin wave propagation can be controlled by the external field its properties can also be tailored in periodically nano-structured ferromagnets, so called magnonic crystals [69, 70, 71]. As the magnetic counterpart of photonic crystals they are promising candidates for applications like (spin wave) filters and we also studied those experimentally and numerically [67, 72].

3.1 The excitation scheme

In order to study spin waves they have to be created first. In principle this can be achieved through many different methods, but in order to experimentally observe the excited spin waves we wish to have phase coherent spin waves with a certain amplitude at frequencies in the GHz regime. The most convenient method to achieve this is excitation through a coplanar wave guide (CPW) (see Fig. 3.3 for a sketch of a CPW). A CPW is a metallic structure through

which a rf-current can flow and create a magnetic field. In the magnetostatic approximation this field is easy to calculate with Biot-Savart's law:

$$\vec{H} = \frac{1}{4\pi} \int_V \frac{(\vec{j}dV) \times \vec{r}}{r^3} \tag{3.1}$$

where $\vec{j}$ is the current density that is assumed to be known either a priori or from some electro-magnetic simulations. When we assume that the current is homogeneous within the conductors of rectangular cross section and that the conductors are infinitely long in the other direction, then we can even calculate the resulting field distribution (in k-space) analytically. For arbitrary current distributions (also infinitely long wires are assumed) a Fast Fourier Transform (FFT) method, similar to the one used to calculated magnetic fields from the magnetization is used to calculate the magnetic field distribution from the distribution of the current.

In Fig. 3.1 a) such a field distribution is shown for a CPW geometry similar to those used in experiments in this section. It is worth noting that the in-plane field is symmetric as the current distribution is also symmetric, but the out-of-plane field is anti-symmetric. Therefore the in-plane excitation field leads to the symmetric excitation of (DE-) spin waves on both sides of the CPW as shown in Fig. 3.1 b), while out-of-plane excitation causes the spin waves to be excited with opposite sign Fig. 3.1 d). Therefore when both components of the excitation field are present as in a real CPW, the linear combination of both leads to an asymmetry in the amplitudes of spin waves excited at different sides of the CPW (Fig. 3.1 c). When the magnetization is reversed for example by reversing the external field the side where more spin waves are excited changes. This is simply due to the fact that the magnetization has a unique sense of precession. Therefore when one only measures the spin wave amplitude on one side of the CPW one finds different amplitudes for positive and negative fields. Note that other effects can also lead to the same result [73]. Although the amplitude is different on both sides of the CPW the wavelength and the phase (at a given distance to the symmetry center) are the same (the phase might change by π).

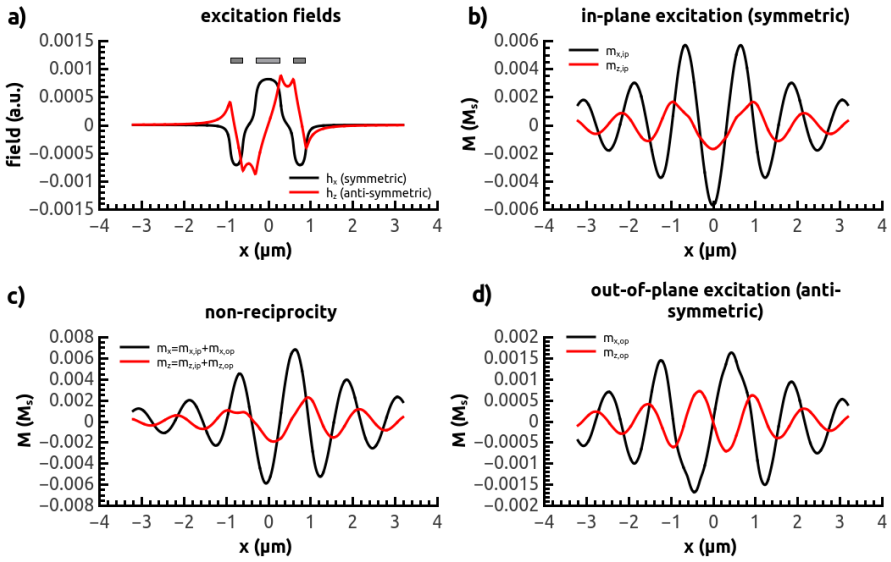

Figure 3.1: a) In-plane (x-direction) and out-of-plane (z-direction) components of the excitation field for a coplanar wave guide (CPW) structure of approximately 2 μm width as shown above the plot. b) In-plane and out-of-plane magnetization components of spin waves excited only by the symmetric in-plane field components. d) the same as is b) but the excitation field is purely out-of-plane. c) Magnetization components of spin waves excited by a realistic field consisting of in-plane and out-of-plane fields as shown in a).

3.2 Spin wave propagation in a magnetic wire

Parts of this section have been published in Applied Physics Letters 104, 102404 (2014) [68].

In the following we investigate the magnon dispersion of spin waves propagating in a Permalloy stripe and compare it to a plane film. Experimentally we directly image the spatial propagation of spin waves using a TR-MOKE. To confirm our findings and to get a deeper insight we perform additional micromagnetic simulations.

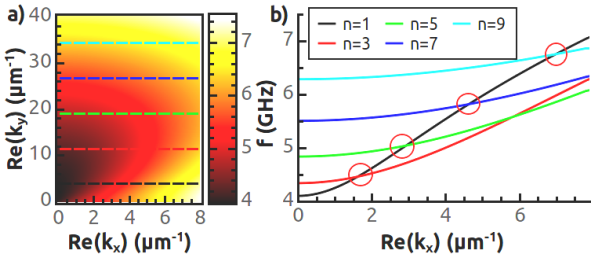

Figure 3.2: a) In the effective stripe model the susceptibility of a thin plane film (color encoded) is used and only quantized transverse wave numbers $k_y = n\frac{\pi}{w}$, $n = 1, 2, ...$ are allowed. b) The branch with the highest group velocity ($n = 1$) crosses other branches. These crossings become avoided crossings in the full micromagnetic model.

We start by discussing the spin wave properties in a thin magnetic film. As already seen in section 2 the dispersion relation is highly anisotropic. It was obtained from a linearization of the Landau-Lifshitz-Gilbert equation [1, 74, 6], where the spatial homogeneity allowed us to use plane wave solutions, i.e. we were looking for the resonance frequency as a function of the real valued k-vector. Therefore the resonance frequency had real and imaginary parts corresponding to precession and temporal decay of spin waves. Now the situation is slightly different, as the propagating spin waves in our experiment are excited continuously and decay spatially. Therefore basically the same equations have to be solved, but now the frequency is a real valued parameter and we obtain real and imaginary parts of the wave vector, corresponding to spatial oscillations and decay.

Another way of seeing the importance of taking the spatial decay part into account is by considering the complex magnetic susceptibility $\chi(\omega, \vec{k})$ which characterizes the linear response of a magnetic system to an external monochromatic excitation. Using linear superposition the spatial spin wave pattern can be calculated as an integral in k-space [75, 76, 77]:

$$\vec{m}_\omega = \int_{-\infty}^{+\infty} \chi(\omega, k)\vec{h}(k)e^{ikx}dk, \tag{3.2}$$

where the harmonic time dependence has been dropped and $\vec{h}(k)$ is the Fourier spectrum of the excitation field as discussed in the previous subsection.

The complex tensor $\chi(\omega, k)$ has poles k_0 in the complex k-plane for a fixed frequency ω. These poles represent spatially decaying spin wave modes. Us-

ing the residue theorem the dynamic magnetization in equation (3.2) can be rewritten as:

$$\begin{aligned} \vec{m} &= \vec{m}_{\text{pole}} + \vec{m}_{\text{imag}} \approx \vec{m}_{\text{pole}} \\ &\approx 2\pi i \,\text{Res}\,|_{k_0}(\chi)\vec{h}(k_0)e^{ik_0 x} \end{aligned} \tag{3.3}$$

In this equation $\vec{m}_{\text{imag}}$ is coming from the integration path over the imaginary k-axis and can be neglected for a coplanar wave guide excitation, i.e. when $\vec{h}(k)$ decreases fast enough to zero for small wave vectors. Apart from this contribution close to the coplanar wave guide the pole(s) k_0 determine the spatial decay rate and oscillation frequency completely. Only the amplitude and phase of the spin wave depend on the excitation $\vec{h}(k_0)$. Therefore for a fixed excitation frequency it does not matter how broad the excitation spectrum in k-space is, as the relevant spin wave parameters wavelength and decay length do not depend on it. Therefore simple coplanar wave guides result in the same wave length and decay length as more complicated k-antennas [62]. As we investigate the dispersion relation of spin waves it is even advantageous to have a broader excitation spectrum as it allows measurements over a wider wave vector range ($\approx 1 - 8\ \mu\text{m}^{-1}$).

In order to know how far an excited spin wave might travel before it decays we look at the damping length in Damon Eshbach (DE, $\vec{k} \perp \vec{M}$) geometry. The thin film susceptibility is known and the dispersion can be calculated [76]. Solving for the wave vector k leads to the damping length l_{damp} which is the inverse of the imaginary part of k:

$$l_{\text{damp}} = \frac{1}{\text{Im}(k_0)} = \frac{dM_s^2\mu_0\gamma}{2\alpha\omega(M_s + 2H_0)} = v_g\tau, \tag{3.4}$$

with the group velocity $v_g = \frac{d(\gamma\mu_0 M_s)^2}{4\omega}$ and the decay time $\tau = \frac{2}{\alpha\mu_0\gamma(M_s+2H_0)}$. From this we can immediately see that the group velocity and the damping length are proportional to the film thickness d. As the group velocity is usually highest in DE-direction and lower in all other directions the film thickness can be a limiting factor for the observation of propagating spin waves, especially in materials with low M_s such as GaMnAs as the group velocity is proportional to M_s^2. Note that v_g varies smoothly as $1/\omega$ with the frequency and therefore we expect $\text{Im}(k_0) \propto \omega$ for DE spin waves in the plane film.

The basic idea for the calculation of the dispersion for spin waves propagating in stripes is to take the dispersion relation from the plane film and quantize the wavevector component k_y which is perpendicular to the propagation direction (Fig. 3.2 a). By doing so the transverse wave vector can attain values of $n\frac{\pi}{\text{w}}$ where w is the width of the stripe and n is an integer.

This procedure seems to be useful as long as there are no strong nonlocal interactions present. Without nonlocal interactions like the dipolar interactions it does not make any difference for the magnetization inside the stripe how wide the stripe is. Therefore in the absence of dipolar interactions the dispersion relation in the stripe changes only by the quantization conditions at the boundaries. Spin waves in the micrometer wavelength regime are still dominated by dipolar interactions. How strong the magnetization in a certain region interacts with the magnetization in another region is expressed by the dipolar tensor or the stray field. Consider now a region of fixed lateral size. As the thickness

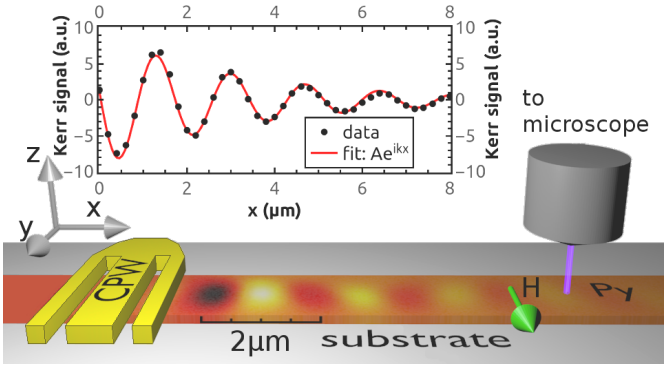

Figure 3.3: Spatial map of the out-of-plane component of the dynamic magnetization recorded by TR-MOKE at a bias magnetic field of 31 mT applied perpendicular to the stripe (DE geometry). A rf-current oscillating at 5.44 GHz in the shorted coplanar wave guide produces an amperian rf-magnetic field that excites the spin wave.

goes to zero, the demagnetizing factor [78] of that region goes to the one for a plane film, i.e. only the out-of-plane component is different from zero. Thus the strayfield does not reach the magnetization in other regions in the plane. Therefore the character of dipolar interactions becomes more and more local when the film thickness decreases. The same applies for the electric stray field of a plate capacitor when the plate spacing is reduced and less field leaks out of the capacitor.

Due to the lateral translational invariance in a plane film the spin waves are eigenmodes, i.e. in a perturbation approach there are no (linear) interactions between them. Therefore the dispersion branches cross each other without repulsion (Fig. 3.2 b). But as discussed before the eigenmodes of the plane film are not exact eigenmodes of the stripe due to the nonlocal character of the dipolar interactions. Therefore spin waves in different branches interact with each other and form avoided crossings where the dispersion relations of the unperturbed modes approach each other. The strength of the level repulsion depends on the two modes and the perturbation term, which is arising from the dipolar strayfield from the edges of the stripe. When the symmetries of the two modes are different, i.e. one is even and the other is odd, then the interaction term vanishes and no avoided crossings are expected (at least from that level of perturbation theory). The CPW only excites modes with $n = 1, 3, 5, ...$, they interact only with other modes with odd n and therefore we expect to observe only the dispersion of these modes and their avoided crossings (Fig. 3.2).

Close to an anti-crossing the dispersion of the main propagating mode (the one with the highest group velocity) becomes flat, i.e. its group velocity and decay length decrease. As a result we expect to observe peaks in $\mathrm{Im}(k)$ when the frequency is varied across an anti-crossing.

To observe this expected behavior we use a time resolved scanning Kerr microscope which allows us to detect the dynamic out-of-plane magnetization with a spatial resolution of about 250 nm. The spin waves in the $Ni_{80}Fe_{20}$ stripe are excited by the magnetic rf-fields in the vicinity of a coplanar waveguide

(CPW) with 2 μm between the ground lines and 600 nm width of the signal line (Fig. 3.3). We record the spatial sinusoidal decay pattern of the spin waves under the continuous excitation with a fixed rf-frequency and a fixed magnetic in-plane bias field perpendicular to the stripe axis. As illustrated in Fig. 3.3 the resulting Kerr image is averaged over the stripe width and fitted to an exponentially decaying wave $m(x) = Ae^{ikx}$, $k \in \mathbb{C}$.

Varying the microwave frequency in small steps of 80 MHz allows to measure the complex spin wave dispersion as shown in Fig. 3.4 a).

The observed dispersion relations with a group velocity of about 2.9 km/s and decay lengths of up to 4.5 μm resemble the one for spin waves in DE-geometry. From the decay length and the group velocity we find amplitude decay times around 1.5 ns and a Gilbert damping parameter α of 0.008 which is typical for thin $Ni_{80}Fe_{20}$ films.

In contrast to a smooth dispersion relation we observe discontinuities at excitation frequencies of 4.72 GHz (for $\mu_0 H = 21$ mT) and 5.2, 6.0 and 6.2 GHz ($\mu_0 H = 31$ mT). Even for the measurements at a field of $\mu_0 H = 41$ mT, which is also shown in Fig. 3.4, the deviations from a smooth dispersion relation are visible, although they are much less pronounced than for the lower field equivalents.

The discontinuities are not only in the real part of the wave vector, but also in the imaginary part of k, where we find maxima corresponding to a short damping length l_{damp} as expected from the flat dispersion close to anti-crossings. These maxima become less pronounced when the magnetic bias field is increased but can still be clearly identified for the $\mu_0 H = 41$ mT measurement.

As the stripe width is approximately 800 nm the transverse k-vector is rather large and the corresponding length is short. Considering $n = 3$, i.e. the next higher transverse mode that can be excited, the transverse wave vector is of the order of $3\pi/0.8\ \mu\mathrm{m}^{-1} \approx 11.8\ \mu\mathrm{m}^{-1}$ corresponding to about 250 nm separation between minimum and maximum, which is also the resolution limit of our TR-MOKE microscope. However, to gain further insight beyond the experimental resolution limit we study spin wave propagation in the wire with micromagnetic simulations [17].

The model wire had a volume of 25.6 μm $\times$ 840 nm $\times$ 13.5 nm divided into 4096×128 cells with periodic boundary conditions along the long dimension. Due to the artificial periodic boundary conditions unphysical effects arise. We checked that the wire was long enough such that these effects are negligible by monitoring the spin wave amplitude at the ends of the wire. Saturation magnetization $\mu_0 M_s = 0.95$ T and Gilbert damping parameter $\alpha = 0.008$ were set to typical values for $Ni_{80}Fe_{20}$.

As spin waves are small excitations of an underlying ground state the magnetization was first relaxed into an equilibrium state. From 'C-shaped' and 'S-shaped' magnetization ground states only the 'S-shaped' configuration is realized in the experiment because it is energetically favorable especially when the external field is not perfectly aligned with the axis (Fig. 3.5). Additional simulations where the dispersion relation was simulated for the 'C-shaped' ground state and compared to the experimental curves confirmed this expectation.

After relaxation the magnetization was excited through the magnetic rf-field of a CPW like structure for a time of 100 excitation periods which allowed the spin waves to spread out and settle their amplitudes everywhere on the sample to balance the energy flow between pumping and relaxation.

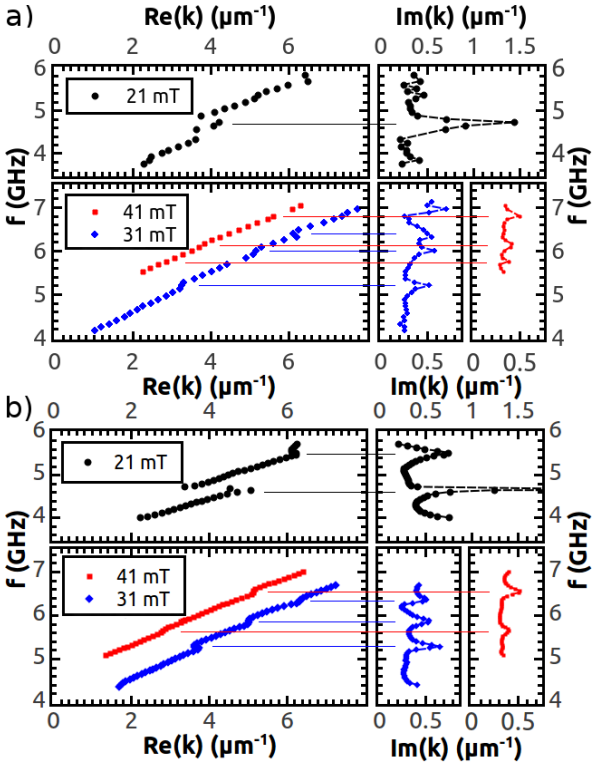

Figure 3.4: a) Experimental complex spin wave dispersion for propagating spin waves in a 15 nm thick and 800 nm wide $Ni_{80}Fe_{20}$ stripe. The propagation direction of the spin waves is perpendicular to the applied bias magnetic field of 21 mT (upper panel), 31 mT and 41 mT (lower panel) along the stripe axis. The dissipative part of the dispersion relations is shown on the right side. b) Corresponding simulated dispersion.

We also simulated for the three different magnetic fields as in the experiments for direct comparison. The dispersion relations extracted from the simulations are shown in Fig. 3.4 b) and agree quite well with their experimental counterparts. In more detail, the agreement is found in real and imaginary parts of the dispersion relation, the group velocities and the anti-crossings for all three fields.

The largest deviations, though still minor, are found in the frequencies where the anti-crossings appear. This might be caused by imperfect knowledge and modeling of the sample or a small misalignment of the external field. In order to check the latter we repeated the simulations with a small misalignment of the external field and found that especially the peak height of the anti-crossings in $\mathrm{Im}(k)$ depends strongly on the misalignment angle. From a comparison with the experiments, we conclude that the in-plane misalignment angle was smaller than 1°.

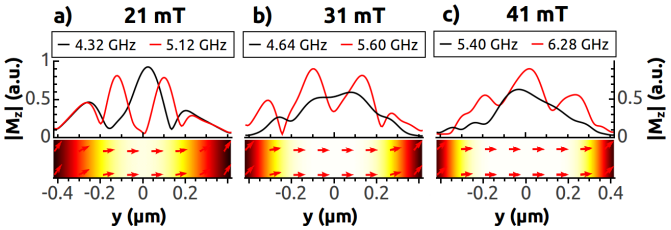

Figure 3.5: Cross sections of simulated ground states are shown color encoded, where bright color represents magnetization aligned with the external field, i.e. perpendicular to the stripe axis. The width of the edge channels (dark color) decreases with the external field leading to less pronounced anti-crossings. The transverse mode profiles of the dynamic M_z component (upper row) show that the characteristic transverse mode number increases from one side of the anti-crossings to the other.

In order to verify that the observed phenomena are indeed due to avoided crossings of spin wave dispersion branches with different transverse wave numbers we plot the spatial amplitude distribution of the out-of-plane magnetization component across the stripe width (Fig. 3.5). The profiles shown for two frequencies, one below and one above the avoided crossing, exemplify that the spectral weight of the higher transverse wave number increases with the excitation frequency. The mode profile also changes significantly from one side to the other.

Thin films can be considered being 2-dimensional as higher spin wave dispersion branches due to the quantization in out-of-plane direction (perpendicular standing spin waves) are found at much higher frequencies due to the small thickness. Therefore no (anti-) crossings are expected for this kind of spin waves in the frequency range below 10 GHz. Therefore the anti-crossings are solely caused by effects from the finite width. To find out whether static or dynamic effects dominate additional simulations are performed where the static magnetic surface charges at the edges of the stripe are artificially compensated. This alters the magnetic ground state to be uniformly aligned with the magnetic bias field in y-direction. By this method the edge channels with reduced effective fields and the modes propagating in these channels are also removed.

Note that only static demagnetizing fields have been compensated and the dynamic fields coming from the precessing magnetization still differ from those of a spin wave in a plane film, especially at the edges.

The simulated spin wave dispersion relations in these artificially altered stripes still display avoided crossings but with slightly reduced coupling strength. Thus changes in the equilibrium magnetization do not play the dominating role and it is the dynamic demagnetizing field which contributes the most to the coupling and the resulting anti-crossings.

The dipolar fields scale with the magnetic moment of the sample and therefore with the thickness. In a thinner sample (10 nm, w ≈ 1 μm) we found only very weak (almost no) signs of avoided crossings when it was measured at a bias field of 31 mT. This also confirms that the anti-crossings are due to the dipolar interactions rather than due to exchange interactions.

The spatial overlap of the spin wave modes is also an important quantity for the interaction strength as already mentioned for the different symmetries. But for decaying waves the overlap in the propagation direction might also depend on the decay length. As Im(k) is proportional to the Gilbert damping parameter α we doubled α in another set of simulations and found that the extracted Im(k) doubles indeed, except for the maxima, where the mode coupling dominates the relaxation and Im(k) is less than twice its original value. Thus the interaction between two spin wave branches must have decreased due to the higher α. The real part of the dispersion which shows less pronounced discontinuities (not shown here) confirms this finding.

In conclusion we studied propagating spin waves in thin wires using time resolved MOKE, simplified analytic models and micromagnetic simulations. We showed that beyond the simplified model avoided crossings in the spin wave dispersion relation can be observed and that they are connected to the dynamic dipolar fields. Furthermore the signs of the anti-crossings have been found to become weaker for higher magnetic bias fields. This is important whenever one wants to avoid discontinuities in the dispersion relation as for example in the following subsection. Although the discontinuities decrease for higher fields the avoided crossings are still there and are observable in measurements of high precision.

3.3 Spin transfer torque parameters P and β

Parts of this section have been published in Physical Review B 89, 020403(R) (2014) [66].

Slonczewski and Berger [7, 8, 9] investigated the transfer of angular momentum from a spin-polarized current to the local magnetization and extended the LLG-equation by an additional torque term (see [79] for a review article). The associated torque is therefore termed spin-transfer torque (STT) ([80] for a tutorial article). Technologically interesting applications are STT-MRAMs, spin transfer nano oscillators (STNO) ([81] for a review article) or the racetrack memory [82] to name but a few. The material parameters that determine the size of the effect are the degree of spin-polarization P of the conduction electrons, ($|u| = \frac{jPg\mu_B}{2eM_s}$) and the degree of non-adiabaticity χ [10] or the non-adiabaticity parameter β respectively. Therefore methods which reliably determine those parameters are desirable, in order to find materials that show properties most suitable for applications. Spin waves are an elegant means of determining both the spin polarization P [83, 84] and β [65, 66] as the calculations in the following subsection show. Practically the previous experiment has to be extended such that an electric current can flow through the $Ni_{80}Fe_{20}$ wave guide and interact with propagating spin waves excited by the rf magnetic field of the CPW.

In the following we determine the material parameters P and β from measurements of spin wave propagation parameters under different current densities, bias fields and at different excitation frequencies.

This seems to be straight forward, but one has to keep in mind that high precision is needed together with a thorough analysis of the data in order to obtain P and especially β. On the experimental side, this has been reached besides other means by actively stabilizing the sample position in all three dimensions as well as the phase delay between the excitation and the probing laser pulse [66]. The sample design was also carefully adjusted to our measurement procedure. Therefore a CPW was used instead of a meander antenna [68, 62] as we measure shifts in the spin wave wave length and not frequency shifts due to the TR-MOKE setup operating principle. Furthermore the Damon-Eshbach geometry is the only configuration that is practically useful in our setup, i.e. the equilibrium magnetization is lying in the plane of the sample and the propagation direction is perpendicular to it. While in general it is advantageous to use thicker stripes to observe longer spin wave propagation, this causes problems in our case. One reason is more heating for the same current density and the second is the dc-Oersted field which is created within the $Ni_{80}Fe_{20}$ stripe and also causes similar shifts in the spin wave parameters. While this effect cannot be avoided completely, it can be minimized by keeping the cross section of the stripe and especially the thickness small, i.e. below 20 nm [73]. Further considerations relate to the frequency of spin wave excitation. One limitation are the effects of the anti-crossings [68]. As shown before these are much stronger at low fields, corresponding to low frequencies. Therefore higher fields that nearly saturate the magnetization transversally to the stripe axis have been used, i.e. 10 GHz excitation frequency corresponding to about 0.1 T external field.

The following analysis of the data connects the measured changes of the spin wave parameters (real and imaginary part of the wave vector k) due to the current on the one side with the material parameters P and β on the other side.

The starting point of the analysis is the Landau-Lifshitz equation with the $\vec{M} \times (\vec{H} \times \vec{M})$ damping term which turns out to be easier to handle than the Gilbert form. As in previous sections we set $|\vec{M}| = 1$, i.e. $\vec{M}$ is the magnetization normalized by M_s. The dynamic equation with the relevant spin transfer torque terms then reads:

$$\frac{\partial \vec{M}}{\partial t} = (1+\alpha^2)\gamma\mu_0 \vec{H} \times \vec{M} - \alpha\gamma\mu_0 \vec{M} \times (\vec{H} \times \vec{M}) + (\beta - \alpha) u \vec{M} \times \frac{\partial \vec{M}}{\partial x} + u(1+\alpha\beta)\vec{M} \times (\vec{M} \times \frac{\partial \vec{M}}{\partial x}) \quad (3.5)$$

When we keep only terms up to linear order in α and β as it turns out that those terms can be considered as small perturbations, we find:

$$\frac{\partial \vec{M}}{\partial t} \approx \gamma\mu_0 \vec{H} \times \vec{M} - \alpha\gamma\mu_0 \vec{M} \times (\vec{H} \times \vec{M}) + (\beta - \alpha) u \vec{M} \times \frac{\partial \vec{M}}{\partial x} + u\vec{M} \times (\vec{M} \times \frac{\partial \vec{M}}{\partial x}) \quad (3.6)$$

Linearizing this equation in terms of small deviations $\vec{m}e^{i(kx-\omega t)}$, i.e. spin waves, from the equilibrium state $\vec{M}_0$ and taking into account that $\vec{M}_0$ and $\vec{H}$ are parallel and $\vec{m}$ is perpendicular to $\vec{M}_0$ leads to:

$$-i\omega\vec{m} = \underbrace{\gamma\mu_0 \vec{H} \times \vec{m} + \gamma\mu_0 M_s N^k \vec{m} \times \vec{M} + \alpha\gamma\mu_0 H \vec{m}}_{\text{torque without STT}} + \underbrace{(\beta - \alpha) iuk \vec{M} \times \vec{m} - iuk\vec{m}}_{\text{STT terms}}. \quad (3.7)$$

which has the advantage that there is no $\alpha\omega$ term from the Gilbert damping torque, which simplifies the following substitutions and there is no derivative with respect to the experimentally not easily controllable parameter α [85], but only derivatives which are (in principle) accessible through experiments by varying the external parameters H and ω while observing k. In fact the STT effects can be written as a shift in the precession frequency and effective external field for the spin wave.

$$\begin{aligned} \omega &\rightarrow \omega \underbrace{-\Delta u k}_{\Delta\omega} \\ H &\rightarrow H \underbrace{+i(\beta-\alpha)\frac{\Delta u k}{\gamma\mu_0}}_{\Delta H} \end{aligned} \quad (3.8)$$

This is correct up to first order in terms of α or β. From this it becomes clear why spin waves are advantageous for the determination of P and β:

Because of the sinusoidally varying magnetization configuration of spin waves the STT does not change the shape of the spin wave and the relevant parameter is its wavenumber k in the direction of the current which is accessible through

measurements. Furthermore when the wavelength of the spin wave is in the micro meter range disorder on the nano scale averages out due to the long range dipolar interactions. Other methods, especially those using vortex core dynamics [86] and (vortex-) domain wall dynamics [87, 88, 89] might suffer from disorder effects due to the local character of the vortex core as shown in simulations in [90, 91]. Our own investigations [92] of field driven vortex domain wall motion show that not even the damping parameter α can reliably be determined in measurements of the domain wall displacement. In our and similar studies [93, 88] the displacement/velocity is proportional to the amplitude of the applied field, but the proportionality constant is strongly (by more than a factor of two) increased due to disorder. This leads to an overestimated Gilbert damping parameter α. Thus determining P and β with spin waves is advantageous compared to methods using strongly localized magnetic structures prone to disorder effects.

Therefore in [66] we determine P and β from measurements of continuously excited spin waves. The precession frequency ω and the external field H are fixed and the only parameter that changes due to STT is the wavenumber k. Its change Δk due to STT is expressed as:

$$\Delta k = \frac{\partial k}{\partial \omega}\Delta\omega + \frac{\partial k}{\partial H}\Delta H \tag{3.9}$$

and when the expressions from equation (3.8) are used:

$$i\frac{\partial k}{\gamma\mu_0 \partial H}(\beta - \alpha) - \frac{\Delta k}{k}\frac{1}{\Delta u} = \frac{\partial k}{\partial \omega} \tag{3.10}$$

Note that this is a complex equation as the decay of the spin wave makes k a complex number. This linear equation is solved for the two real quantities $(\beta - \alpha)$ and $\frac{1}{\Delta u}$. The result for β is:

$$\beta = \frac{\mathrm{Im}\left(\frac{\partial k}{\partial \omega}\cdot\left(\frac{\Delta k}{k}\right)^*\right)}{\mathrm{Re}\left(\frac{\partial k}{\gamma\mu_0\partial H}\cdot\left(\frac{\Delta k}{k}\right)^*\right)} + \alpha \tag{3.11}$$

As before the denominator is well approximated with
$\mathrm{Re}\left(\frac{\partial k}{\gamma\mu_0\partial H}\right)\mathrm{Re}\left(\frac{\Delta k}{k}\right)$ whereas the numerator's second part
$\mathrm{Im}\left(\frac{\partial k}{\partial \omega}\right)\mathrm{Re}\left(\frac{\Delta k}{k}\right)$ gives a contribution of the order of 10%. As $\mathrm{Im}\left(\frac{\partial k}{\partial \omega}\right)$ is too small to be determined directly with reasonable errors, we use the plane film approximation $\mathrm{Im}\left(\frac{\partial k}{\partial \omega}\right) \approx \frac{\mathrm{Im}(k)t}{1-\mathrm{Re}(k)t}\cdot\mathrm{Re}\left(\frac{\partial k}{\partial \omega}\right) \approx \frac{\mathrm{Im}(k)t}{1-\mathrm{Re}(k)t}\cdot\frac{1}{v_g}$ and α determined from the measured decay length $\alpha \approx \frac{2v_g\,\mathrm{Im}(k)}{\gamma\mu_0(2H+M_s)}$. Therefore:

$$\beta \approx \frac{\frac{-1}{v_g}\cdot\mathrm{Im}\left(\frac{\Delta k}{k}\right)}{\mathrm{Re}\left(\frac{\partial k}{\gamma\mu_0\partial H}\right)\cdot\mathrm{Re}\left(\frac{\Delta k}{k}\right)} + \frac{\frac{1}{v_g}\cdot\frac{\mathrm{Im}(k)t}{1-\mathrm{Re}(k)t}}{\mathrm{Re}\left(\frac{\partial k}{\gamma\mu_0\partial H}\right)} + \alpha \tag{3.12}$$

Applying this method to the simulations, where we have control over all parameters we find only a small difference (of about 2%) between the β value that was set manually and the one we re-extracted from the simulated decaying spin waves for parameters similar to those found experimentally [66].

Solving equation (3.10) for Δu leads to:

$$\Delta u = \frac{\mathrm{Re}\left(\frac{\partial k}{\gamma\mu_0 \partial H} \cdot \left(\frac{\Delta k}{k}\right)^*\right)}{-\mathrm{Re}\left(\frac{\partial k}{\partial \omega} \cdot \left(\frac{\partial k}{\gamma\mu_0 \partial H}\right)^*\right)} \tag{3.13}$$

and with the same arguments as before it can be approximated as $\Delta u \approx \mathrm{Re}\left(\frac{\partial \omega}{\partial k}\right) \mathrm{Re}\left(\frac{\Delta k}{k}\right)$ without introducing large errors.

Note that this way of determining P and especially β relies on the accurate measurement of the change of the k-vector with the current, the field and the frequency. Therefore a considerable amount of work in our group (especially Jean-Yves Chauleau and Johannes Stigloher) has been put into the improvement of its precise determination and ongoing work tries to push the limits further. Currently the accuracy for the determination of Δk from a single image (approximately 20 minutes) is in the range of $5 \cdot 10^{-4}$ $\mu\mathrm{m}^{-1}$ for $k \approx (3.10 + 0.25i)$ $\mu\mathrm{m}^{-1}$ and should in principle be sufficient to study the dependence of β on other parameters.

3.4 Spin waves in antidot arrays

Parts of this section have been published in Physical Review Letters 105, 067208 (2010) [67] and in Physical Review B 84, 184411 (2011) [72].

A plane ferromagnetic (thin) film can be patterned periodically for example by removing magnetic material or changing material properties on a regular lattice. By this way spin wave properties can be tailored. For example the group velocity can be tuned or band gaps in the spin wave dispersion can be introduced. This idea is the magnon counterpart of photonics and therefore termed magnonics [94, 71].

3.4.1 Spin wave modes

In order to demonstrate that by the removal of a small amount of magnetic material spin wave propagation can be significantly altered we compare spin wave propagation in an antidot array with the one in a plane film. Dipolar dominated spin waves in a plane film reach their maximum group velocity in the direction perpendicular to the external field and the magnetization (Damon-Eshbach direction, DE) and therefore this configuration is best suited for the observation of spin waves in experiments. As an example a square array of circular antidots has been investigated with our MOKE-setup and by micromagnetic simulations. The $Ni_{80}Fe_{20}$ film was nominally 22 nm thick and the holes were fabricated using a focused ion beam (FIB) and had a diameter of 120 nm $\pm$ 30 nm and a center-to-center spacing of 800 nm. The samples were fabricated by the group of Prof. Dr. Grundler in Munich (TUM).

First micromagnetic simulations were performed [16], where the excitation field was oriented perpendicular to one of the antidot array axes. One-dimensional periodic boundary conditions were used along this axis to reduce computational costs. An external bias field of 20 mT was applied to ensure good spin wave propagation in DE-geometry and the magnetization was relaxed into an equilibrium state. In order to investigate spin wave propagation a magnetic δ-like field pulse that was spatially confined to a small region around the middle of the simulation volume (85 antidot lattice sites, 0.8 μm $\times$ 68 μm) was used to excite spin waves. The time evolution of the magnetization was recorded for 10 ns and Fourier transforms in space and time reveal the dispersion relation of spin waves propagating away from the excitation region.

In Fig. 3.6 a) the result for the antidot lattice is shown as the grey-colored background for spin wave propagation along a lattice axis in DE-configuration. The circles and squares show the corresponding MOKE-measurements on the antidot array and the plane film respectively. Apparently the dispersion relation for spin waves in the antidot array is discontinuous, i.e. there are frequencies at which spin wave propagation is strongly suppressed. This resembles the situation in Fig. 3.4 where different transverse spin wave modes form anti-crossings in the dispersion relation of spin waves propagating in a stripe. And indeed the spatial profiles in Fig. 3.6 b) - d) reveal that spin wave propagation is similar in the antidot arrays. The effective fields around the antidots form channels that allow spin waves to propagate just like in a stripe. Therefore it is also not surprising that different transverse modes can be identified and anti-crossings in the dispersion relation can be observed.

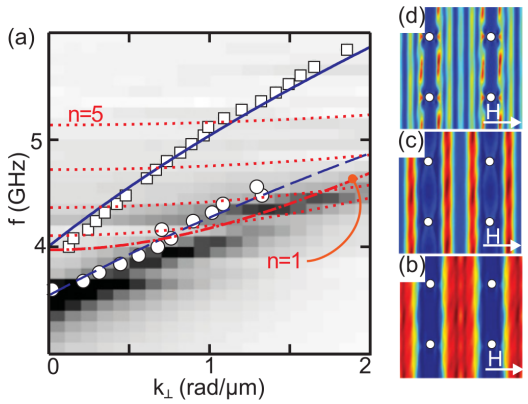

Figure 3.6: a) Measured dispersion relation for spin waves in the antidot array (circles) and the plane film (squares). Spatial profiles in b) - d) red means high amplitude, dark blue no amplitude.

3.4.2 Angular dependence

Next we show that spin wave propagation can be suppressed in antidot arrays by varying the field angle by a few degrees. Therefore we repeat the micromagnetic simulations at different angles of the bias field. In order to compare the simulation results with the experiments we restrict our investigations to a k-vector which approximately corresponds to the excitation maximum of the actual coplanar wave guide used to excite spin waves in the antidot sample.

In Fig. 3.7 the angular dependence of the spin wave resonances for a k-vector of $\approx 0.8\ \mu\mathrm{m}^{-1}$ are shown for a plane film (left) and for the antidot lattice (right).

Away from the DE direction (0°) the group velocity smoothly decreases in the plane film leading to a decreasing resonance frequency when the field angle is increased towards BV-direction (90°). At the same time the amplitude decreases as the in-plane component of the excitation field becomes parallel to the static magnetization and the resulting torque goes to zero.

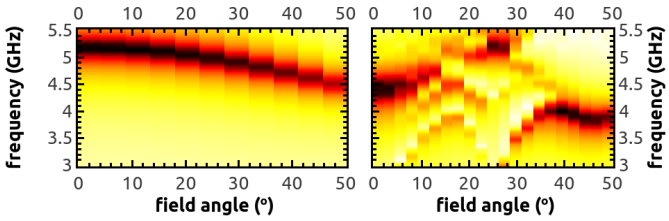

Figure 3.7: In a plane film (left) the resonance frequency of a spin wave with a small wave vector ($k \approx 0.8\ \mu\mathrm{m}^{-1}$) decreases when the field angle is increased away from the DE-direction ($\hat{=}0°$) towards BV-direction ($\hat{=}90°$). In the antidot lattice (right) mainly the three modes at 0°, 25° and around 45° shown in Fig. 3.8 propagate.

In contrast to the simple and smooth picture in the plane film at least three different regions of spin wave propagation in the antidot array can be identified for field angles between 0° and 50°: The first one corresponding to propagation

in DE-direction ($0° \hat{=} (1,0)$), the second to propagation along the $(2,1)$-direction ($\hat{=}26.6°$) and the third one to propagation along the $(1,1)$-direction ($\hat{=}45°$).

Spatial profiles of these three modes have been imaged by TR-MOKE and confirmed by micromagnetic simulations. Fig. 3.8 shows that for 0° (a) and 45° (c) the spin waves only propagate in between the antidots like in a stripe.

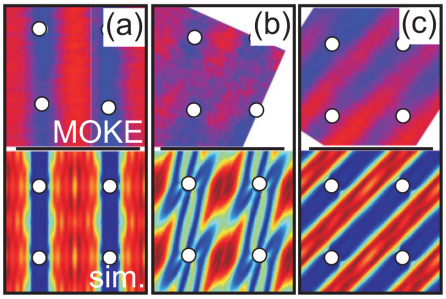

Figure 3.8: Spin wave modes in the antidot lattice for three different field angles of a) 0°, b) 25° and c) 45°. The measurements in the upper row compare quite well with the simulations in the second row.

3.4.3 Spin wave injection into the antidot lattice

So far we have investigated spin wave propagation either in a plane film or in a structured plane film (stripe or antidot lattice). In the language of photonics this would be photons in a homogeneous medium (air) and in a photonic crystal or wave guide. Here we investigate the injection of spin waves from the plane film into the antidot array. When we disregard some of the properties of spin wave propagation in the antidot lattice, the antidot lattice can be seen as a metamaterial [72]. In this case the metamaterial is described by effective material parameters (M_s^*) that describe the main features of propagating spin waves without looking at the structural details of the antidot lattice. Therefore the structuring may be seen as tailoring these effective parameters. For this to work it is usually required that the wave length of the propagating waves is larger than the lattice constant, i.e. $\lambda > 0.8\ \mu$m as it was in our case. In [72] we investigated the transmission and reflection of cw-excited spin waves at the plane film to antidot boundary within this simplified approach.

In particular we analyzed the interference pattern of MOKE images of incident and reflected spin waves from the boundary (Fig. 3.9) using

$$|M_z(x)| \propto | \underbrace{e^{-ikx}}_{\text{incident wave}} + \underbrace{(1-t)e^{ikx}}_{\text{reflected wave}} | \tag{3.14}$$

where the origin ($x = 0$) was set to the boundary and k is the complex wave vector of the spin wave in the plane film. $t = 1 - r$ is the transmission coefficient for spin waves into the antidot array. This turned out to be more reliable than the measurement of the transmission as the spin waves decay quite fast in the antidot lattice and the MOKE signal might change due to the patterning in the antidot lattice, especially when the transmission is low. The complex k-vector depends on the excitation frequency and it was found that the transmission

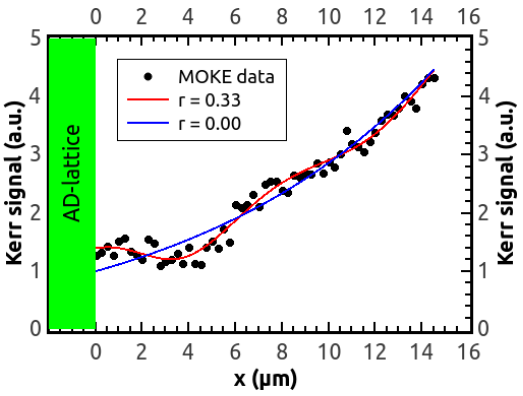

Figure 3.9: Reflexion and interference of spin wave coming from the right and being partially reflected at the antidot-to-plane film boundary. The experimental data taken at 4.48 GHz shows the amplitude of the spin wave calculated from two consecutive measurements of real and imaginary parts together with a fit to equation (3.14) (red) and the corresponding curve without reflexion (blue).

coefficient t follows the dependence expected for a wave at a boundary [72, 44]:

$$t(f) = \frac{2k_{\mathrm{pf}}(f)}{k_{\mathrm{AD}}(f) + k_{\mathrm{pf}}(f)} \tag{3.15}$$

where k_{pf} and k_{AD} are the k-vectors in the plane film and in the antidot lattice respectively. For our sample (prepared in the group of Prof. Dr. Grundler) and the external magnetic field in the DE-direction (0°) the k-mismatch leads to a relatively poor transmission of $t \approx 0.5$. Remembering Fig. 3.7 we can see that the mismatch for our case is smaller for the spin wave mode around 25°, i.e. for the field applied at an angle of approximately 25° a better transmission of spin waves from the plane film into the antidot lattice can be expected. This is also seen in all-electric spin wave spectroscopy measurements performed by the group of Prof. Dr. Grundler and in our time-resolved MOKE measurements [72]. In conclusion the description with an effective medium allows to understand most of the transmission properties, but does not cover things like the anti-crossings for example which are also observable in the transmission measurements mentioned above.

Chapter 4

Vortex core dynamics

So far we have investigated spin wave excitations of the magnetic ground state, where the ground state can be considered trivial in a topological sense. The ground state of the magnetization configuration can also be non-trivial as for example in the case of a vortex state shown in Fig. 4.1.

Opposed to a spin wave a vortex is protected against decay by its topology and there is an additional type of excitation corresponding to the translation of the vortex core. This motion, termed gyration or gyro motion, is a low frequency excitation with a resonance frequency usually below 1 GHz.

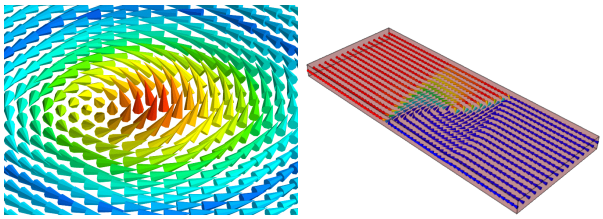

Figure 4.1: Left: A vortex state consists of in-plane magnetization curling around the vortex core where the magnetization points out-of-plane. The typical size of the vortex core is several tens of nanometer and depends on the strength of the exchange interaction. Right: In stripes, domain walls separate regions of different magnetization directions. Depending on the geometry and material parameters different kinds of domain walls can form. For example in a 20 nm thick and 1 μm wide $Ni_{80}Fe_{20}$ stripe a vortex domain wall is formed as shown on the right.

4.1 Collective coordinates

Due to the rigidity of the vortex structure it makes sense to consider the vortex core as a particle that can move within some potential given by real and effective magnetic fields. In order to describe the effective fields acting on the vortex core a collective coordinate approach describes the magnetization $\vec{M}(\vec{r})$ by a few coordinates like the position of the vortex core and allows to obtain simple equations that describe the motion of the vortex core as long as the assumption

of a rigid magnetic structure is reasonable. This method proved to be quite successful not only in describing the motion of a vortex in a magnetic disk, but also for vortex domain wall motion. Therefore we will briefly introduce the basic principle.

We follow D. J. Clarke et al. [95] who used such an approach to describe the motion of vortex domain walls with up to six collective coordinates (the lateral coordinates of the positions of the vortex and the two half anti-vortices shown for example in Fig. 4.2) to introduce the gyrotropic motion of the vortex core in a domain wall.

Starting with the Landau-Lifshitz equation [5, 6] in Gilbert form, which reads:

$$\dot{\vec{m}} = \gamma\mu_0\vec{H}_{\text{eff}} \times \vec{m} + \alpha\vec{m} \times \dot{\vec{m}}. \tag{4.1}$$

where $\vec{m} = \vec{M}/M_s$, $\mu_0\vec{H}_{\text{eff}} = -\delta U/\delta\vec{M}(\vec{r})$ and $\gamma = g|e|/(2m_e)$, we introduce collective coordinates ξ_i (which no longer depend on $\vec{r}$) by writing:

$$\dot{\vec{m}}(\vec{r}) = \frac{\partial\vec{m}(\vec{r})}{\partial\xi_i}\dot{\xi}_i \tag{4.2}$$

In our investigations the collective coordinates describe the position of the vortex core, i.e. $\xi = (X, Y)$. Inserting this expression into the Landau-Lifshitz equation leads to the 'Thiele-equation' [96, 97]:

$$F_i - \Gamma_{ij}\dot{\xi}_j + G_{ij}\dot{\xi}_j = 0 \tag{4.3}$$

where the parameters are given by:

$$F_i = -\int dV \frac{\delta U}{\delta\vec{m}} \cdot \frac{\partial\vec{m}}{\partial\xi_i} = -\frac{\partial U}{\partial\xi_i} \tag{4.4}$$

$$\Gamma_{ij} = \alpha J \int dV \frac{\partial\vec{m}}{\partial\xi_i} \cdot \frac{\partial\vec{m}}{\partial\xi_j} \tag{4.5}$$

$$G_{ij} = J \int dV \vec{m} \cdot \frac{\partial\vec{m}}{\partial\xi_i} \times \frac{\partial\vec{m}}{\partial\xi_j} \tag{4.6}$$

with $J = M_s/\gamma$. Γ_{ij} and G_{ij} can be found when we assume to know an expression for $\vec{m}(\vec{r})$ in terms of ξ. This expression can be found numerically from a simulated magnetization configuration or by fitting the simulated time evolution of ξ_i either to the numerically calculated trajectory or - if possible - to the analytic solution. Γ is the symmetric matrix of viscosity coefficients and G is the antisymmetric gyrotropic matrix. In the case where the collective coordinates are just the two in-plane coordinates of the vortex core position (X, Y), G can also be represented as the crossproduct with a vector: the gyrotropic vector, which points out-of-plane.

When the forces F_i are due to a parabolic potential $U = (k_x X^2 + k_y Y^2)/2$ as approximately in a disk for example, analytic solutions can easily be found and resemble the one for the Landau-Lifshitz-Gilbert equation (2.1):

$$\omega \approx \sqrt{k_x k_y}/G - \frac{i\Gamma}{G^2}(k_x + k_y)/2 \tag{4.7}$$

Therefore the equilibrium position of a vortex is approached in a spiraling motion of the vortex core for a disk, whereas the equilibrium is approached exponentially without oscillations for a vortex (domain wall) in a stripe. This

can easily be seen by assuming e.g. $k_y = 0$ in the above equation (although the damping term is not correct in this case since the approximation $\Gamma \ll G$ that was used to obtain the equation does not hold). Comparing micromagnetic simulations of vortex domain wall motion with results using the Thiele equation gives quite good agreement for narrow wires even above the walker breakdown [95]. For wider wires the fact that a vortex switches its polarity when a certain critical velocity [98] is reached has to be taken into account. In addition the confining potential in the stripe also depends on the vortex core polarity [95]. Both facts together lead to different switching behavior for the two vortex polarities which will be discussed in the following [99].

But caution should be taken when extracting material parameters from experiments, because one also has to consider disorder as the vortex core gets easily pinned due to its small size. The vortex core senses inhomogeneities stronger than e.g. a spin wave mode [100]. Especially the extraction of the Gilbert damping coefficient from vortex domain wall motion experiments is problematic when using simple collective coordinate models as there are no additional magnetic excitations, like spin waves, wall distortions etc. in the model which can absorb energy. This energy dissipation is typically underestimated within this model when compared to real experiments. Consequently the real Gilbert damping parameter is typically over-estimated [92]. Similarly disorder may play a role in the evaluation of spin transfer torque parameters (P and β) when vortex dynamics or vortex domain wall dynamics are used [91].

4.2 Vortex domain wall dynamics

In this section we study the motion of vortex domain walls (Fig. 4.2) under in-plane field pulses. In particular we focus on the displacements of such walls after short (23 ns) field pulses in stripes and investigate disorder effects.

The expected behavior that has also been observed experimentally [92] is as follows: For weak pulse amplitudes smaller than the depinning field disorder pins the domain walls and no displacement is observable. When the field is strong enough to depin the domain wall from its local pinning potential the domain wall moves with an averaged velocity that is proportional to the field amplitude. We will use the slope of displacement vs. field amplitude in this linear regime to extract the effective damping constant α_{eff}. For even higher field amplitudes the linear regime ends abruptly at the Walker field H_w above which smaller displacements/velocities are observed Fig. 4.6.

The experiments in this section have been conducted by Tobias Weindler and Robert Islinger under the supervision of Jean-Yves Chauleau using a wide field MOKE setup.

In the beginning of the theoretical investigations it is instructive to consider stripes without disorder within the collective coordinate approach introduced in the previous subsection.

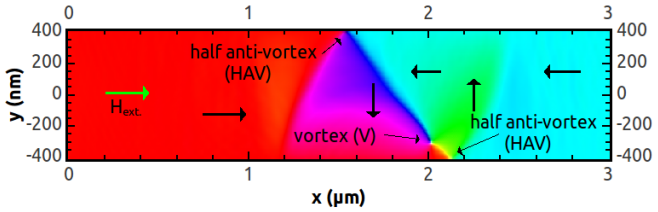

Figure 4.2: Magnetization configuration of a moving vortex domain wall in a 800 nm wide stripe. The vortex core and two half anti-vortices at the edges of the stripe are bound to a 90° Neel wall and two additional walls beginning at the half anti-vortices form the front and the back part of the complete vortex domain wall structure. When an external magnetic field is applied the whole structure moves and the vortex core shifts its relative position within the domain wall.

It has been noticed that due to the missing mirror symmetry in a stripe with a vortex domain wall, the motion of the domain wall depends on its chirality

$$\chi = c \cdot p. \tag{4.8}$$

For example the velocity with which the vortex core collides with the edge of the stripe above the Walker breakdown is significantly higher for one edge than for the other [101].

A mechanism for vortex core polarity reversal where the vortex core does not reach the boundaries of the sample has been studied extensively in disks and squares with a magnetic vortex ground state. When the vortex core is excited such that it moves with high velocity a region of opposite out-of-plane magnetization next to the vortex core evolves (Fig. 4.3 c) due to the gauge field coming from the translation of the rigid vortex core [102]. At a critical velocity

[98] which is roughly 300 m/s for Permalloy this dip-region is large enough such that a vortex-anti-vortex pair of opposite polarity is created within this region and the anti-vortex annihilates with the original vortex core, i.e. a vortex core of reversed polarity is left over [103, 104]. In the following we combine the concept of a critical velocity for the vortex core with the collective coordinate approach for domain wall motion.

In order to find the vortex core trajectory and its velocity we use eq. 4.3 in terms of the two spatial coordinates (X, Y) of the vortex core with the potential

$$U(X,Y) = -QH(X + b\chi Y) + \frac{1}{2}kY^2 \tag{4.9}$$

where $Q = 2\mu_0 M_s dw$ is the magnetic charge associated with a domain wall in a magnetic stripe of width w thickness d and saturation magnetization M_s. The first term is due to the magnetic field that tends to shrink one domain and increase the other. The $-QHb\chi Y$ term arises due to the 180° rotational symmetry that is broken when a magnetic field is applied (b is of the order of unity [95]) and therefore depends on the chirality χ. The last term is the parabolic potential with stiffness constant k due to the finite width of the stripe and leads to the equilibrium position of the vortex core in the middle of the stripe ($Y = 0$) when no external field is applied ($H = 0$).

4.2.1 Above the Walker breakdown

Parts of this section are in preparation for publication [99].

We consider now the following situation: The domain wall is initially at rest in its equilibrium position in the middle of the stripe, which we define as the origin $(X,Y)_{t=0} = (0,0)$ (see Fig. 4.3) and then a magnetic field in x-direction is suddenly switched on.

Without disorder the forces F_x, F_y in equation (4.3) are invariant under translations in the direction of the stripe axis x, i.e. $F_y = F_y(y) = QHr\chi - kY$ and $F_x = const. = QH$. According to equation (4.3) the vortex core velocity $v = \sqrt{\dot{X}^2 + \dot{Y}^2}$ is no longer a function of X and it is directly linked to the transverse displacement Y, i.e. $v = v(Y)$. As the critical velocity $v_{\text{crit.}} \approx 1.66\gamma\sqrt{A_{\text{ex}}}$ [98] for a moving vortex depends on the exchange constant and not on p or χ, the corresponding critical transverse force $|F_{y,\text{crit.}}|$ is also independent of p and χ. Note that in the above expression non-SI units have been used and $1.66\gamma\sqrt{10^{-7} \cdot A_{\text{ex}}}$ has to be used instead when the values for γ and A_{ex} are used in SI units. Interestingly this force leads to different critical transverse displacements $Y_{\text{crit.}} = \frac{1}{k}(QHr\chi - F_{y,\text{crit.}})$ that differ by $\frac{2}{k}QHr$ for the two chiralities $\chi = \pm 1$.

This has interesting consequences. When the vortex core reaches the critical transverse displacement, it becomes unstable and reverses its polarity and thereby the product $c \cdot p = \chi$ changes sign. The important point is that the critical transverse displacement for its new polarity is different from the one before the reversal. It becomes larger for one case and smaller for the other case of the initial core polarity. When it increases, nothing special happens: the vortex core starts to move towards the middle of the stripe with a reduced velocity. In the opposite case, when the critical transverse displacement is smaller than before the switching, the reversed vortex core starts to move towards the middle of the stripe with a velocity that is larger than the critical velocity which might lead to a second polarity reversal a short time after the first one.

In Fig. 4.3 a) and b) we show simulated trajectories of the vortex core for different initial vortex core polarities. The sense of the in-plane rotating magnetization (circulation c of the vortex wall) is the same and therefore the chirality $\chi = c \cdot p$ is initially opposite for the two cases. For a field pulse of 5 Oe amplitude and 15 ns duration, which is below the Walker breakdown, the vortex core polarity is never reversed (Fig. 4.3 a) and the displacements a long time after the end of the field pulse are equal for the two initial polarity cases. For a field above the Walker breakdown field, the vortex core changes its polarity at least once and the behavior after this first reversal is qualitatively different for the two cases as explained before. Each reversal process causes spin waves to be emitted and hence additional relaxation of energy from the magnetic vortex core system first to spin waves and then to the lattice. During the time immediately after the first reversal the transverse velocity $\dot{X}$ depends strongly on the initial polarity and leads to displacements of the vortex at the end of the pulse and after relaxation which differ by several micrometers. Therefore it is possible to observe this chirality effect on the domain wall displacements with static measurements that only determine the position of the domain wall before and after the field pulse.

In order to observe this effect the vortex core has to reach its critical velocity

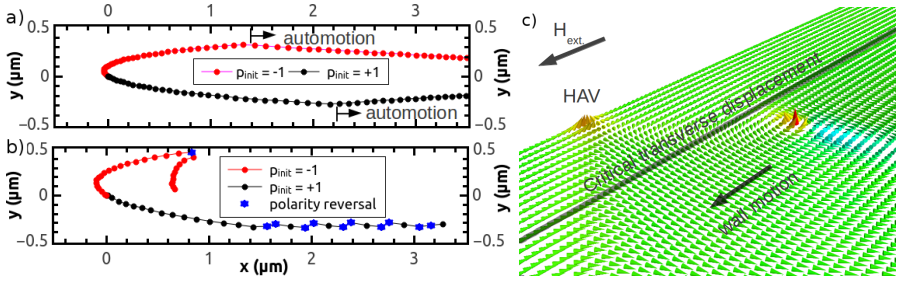

Figure 4.3: a) Simulated trajectories of the vortex core for a 1 μm wide stripe (20 nm thick). Data points are drawn in 500 ps time steps and the field pulse had an amplitude of 5 Oe and a duration of 15 ns. After the end of the pulse the transverse displacement of the vortex core translates into longitudinal displacement (automotion [105]). Note that the two curves reach the same final displacement when extrapolated ($t \to \infty$). This is no longer the case for field amplitudes above the Walker breakdown. b) Above the Walker breakdown field the trajectories during a 15 ns long pulse (11 Oe amplitude) differ qualitatively due to different reversal behavior. c) Snapshot of the magnetization around the vortex core during domain wall motion. The fast motion of the vortex core causes a gauge-field with opposite polarity and a dip in the out-of-plane magnetization (blue region) next to the vortex core which eventually induces the polarity reversal process.

before it collides with the stripe edge. According to simulations for 20 nm thick stripes this is typically the case when the stripe is at least 750 nm wide. Another parameter that was investigated is the roughness of the sample. It was found that the maximum field above the Walker breakdown at which the difference in the displacements is still observable decreases with increasing disorder, but realistic estimates suggest that the effect is observable experimentally.

For comparison with the experiments we simulate stripes of 20 nm thickness and approximately 750 nm width (Fig. 4.4) with vortex walls of both polarities. Field pulses of 23 ns duration are applied and the final displacement of the domain wall is determined. The simulations are repeated for ten realizations of disorder which is modeled as a variation of the saturation magnetization $D = \sqrt{\langle (M(r) - M_s)^2 \rangle}/M_s$ of 3% in this case, mimicking thickness variations in the same way as it has been done by Min et al. [101]. In Fig. 4.4 the displacement $\delta q := X(t \to \infty) - X(t = 0)$ is normalized by the Thiele width Δ_T defined as

$$\frac{2}{\Delta_T} = \frac{1}{d} \int \left(\frac{\partial \vec{m}}{\partial x} \right)^2 dxdy \tag{4.10}$$

in order to make stripes of different width comparable [106, 96]. The integral is over the whole area of the magnetic stripe containing the domain wall and $\vec{m}$ is the magnetization direction of unit length averaged over the stripe thickness d. As our samples are sufficiently thin such that we do not expect substantial variations of $\vec{m}$ with the thickness we use only a single layer of cells in the out-of-plane direction in our micromagnetic simulations. We evaluate the Thiele width Δ_T from these simulations for the relaxed state as well as during domain wall motion and find only small deviations of less than 5% between these two

situations. It is clearly visible in Fig. 4.4 that above the Walker breakdown field of about 0.8 mT domain walls with large displacements are all of the same initial polarity/chirality (black), while most of the short displacements correspond to vortex domain walls with the opposite initial polarity/chirality (red). Sometimes, probably influenced by disorder and the interference of the vortex core with spin waves that have been emitted after the first reversal, the second reversal does not take place and therefore not all short displacements have the same initial vortex core polarity.

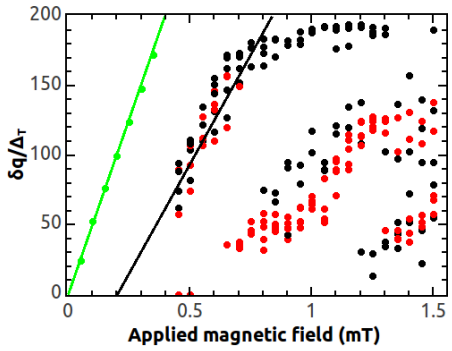

Figure 4.4: Results of micromagnetic simulations of vortex domain walls in 750 nm wide and 20 nm thick stripes with surface disorder. The simulation for each initial polarity was repeated for five different realizations of disorder. Black and red symbols correspond to $p_{\text{init}} = \pm 1$ as in Fig. 4.3. The final displacement δq of the domain walls due to a 23 ns long field pulse of various amplitudes is shown normalized by the Thiele width Δ_T. Below the Walker breakdown field of approximately 0.8 mT all data points follow a single line, whereas they split into two regions above the Walker breakdown field. For comparison a simulation without disorder is also shown (green).

In experiments we cannot easily determine the polarity of the vortex or its chirality directly, but the displacement of the domain wall after the field pulse and the relaxation is accessible in wide field MOKE measurements [99, 92]. Therefore displacements for fields above the Walker breakdown field have been recorded in order to obtain histograms of the domain wall displacements. We expect to see two peaks corresponding to the two different initial chiralities and their distinct behavior after the first polarity reversal process.

In the experiments a new vortex wall was initiated by applying a short field pulse before each measurement of the wall displacement. This field pulse allowed us to inject a domain wall from a nucleation pad into the stripe. As we do not try to control the chirality of the initial vortex wall we believe that we nucleated an approximately uniform distribution of initial states of both chiralities and polarities.

For field amplitudes in the linear regime (Fig. 4.5 a) a single peak is observed, i.e. no difference is visible between the displacements of initial states with different chirality as expected. In contrast, for pulse amplitudes above the Walker breakdown (dark blue line in Fig. 4.5 a) the distribution shows two peaks. We attribute the peak at higher displacement to the case where the vortex core moved to the edge and repeatedly reversed there until the end of

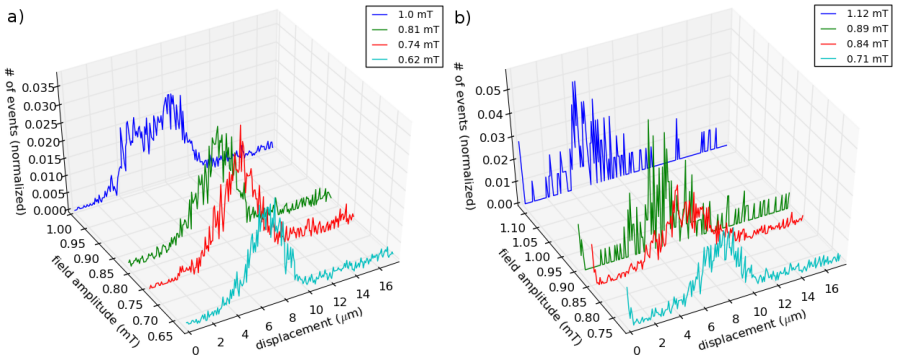

Figure 4.5: a) Experimentally determined number of events for detecting a certain domain wall displacement normalized to the total number of events. The sample is a 750 nm wide stripe and the pulse length is 46 ns. Longer field pulses are used for a more reliable detection of the domain wall displacements from wide field Kerr images. Only for the measurement above the Walker breakdown field (1.0 mT) the distribution of the detected displacements is no longer single peaked and displays a second peak at shorter displacements. b) For a 500 nm wide stripe all measured distributions seem to be single peaked with smaller displacements above the Walker breakdown (1.12 mT).

the pulse and the peak at the lower displacement to the case of the opposite initial chirality, i.e. the one with smaller critical transverse displacement.

Furthermore in order to check that these two peaks are not due to differences in the magnetic properties at both edges of the stripe we performed measurements on stripes with different widths on the same sample. While we find two peaks for wider stripes (1 μm) the histograms for 500 nm wide stripes show only a single peak below and above the Walker breakdown field (Fig. 4.5 b).

In the narrow stripes the vortex core collides with the stripe edge before its critical velocity is reached. Thus, in these samples the reversal is no longer due to the critical velocity and the vortex core periodically traverses the stripe from one side to the other, reversing its polarity once at each side. Consequently no large difference in the displacements is expected for both chiralities.

In conclusion we found a displacement of vortex domain walls under the action of field pulses that depends on the chirality of the initial state. This can be understood within the framework of the Thiele equation combined with the concept of a critical vortex core velocity.

4.2.2 Below the Walker breakdown

Parts of the following two sections have been accepted for publication in Physical Review Letters [92].

As already mentioned before disorder plays a significant role in domain wall motion. In the following we therefore investigate disorder effects on domain wall motion in the linear regime, i.e. below the Walker breakdown where they can be quantified. Two effects can be distinguished: pinning and enhanced dissipation. While the first one can be understood intuitively, the second one

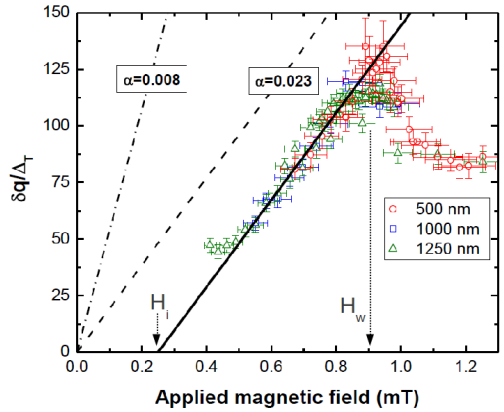

Figure 4.6: Experimental domain wall displacements δq normalized by the Thiele width Δ_T as a function of the applied magnetic field amplitude for stripes of different width. The black line is a linear fit of domain wall dynamics in the linear regime. The dashed and dot-dashed lines are the expected behaviors in the steady state regime for $\alpha = 0.023$ and $\alpha = 0.008$ without disorder.

needs further investigations; especially the question by how much dissipation can be increased through disorder is of interest in the following. It is clear that it cannot be increased arbitrarily for a given field amplitude as no energy is dissipated as soon as the domain wall is completely pinned and does not move at all.

In order to connect domain wall displacements with dissipation we use [107, 105]:

$$\frac{\delta q}{\Delta_T} = \frac{\gamma}{\alpha} \int \mu_0 H(t) dt \tag{4.11}$$

with the Thiele width Δ_T. This equation states that the displacement increases linearly with the field amplitude and the slope is indirectly proportional to the damping parameter α. The validity of this equation was checked in simulations without disorder, i.e. α in this equation coincides with the Gilbert damping parameter in the simulations (green data points in Fig. 4.4). Note that this equation is derived from equation (4.3) and therefore does not take interactions of the domain wall with dynamic excitations of the magnetization, like spin waves or domain wall distortions, into account.

We want to discuss now the effects of disorder on the domain wall displacement in more detail. When a domain wall is depinned from its initial pinning site the moving domain wall also becomes trapped earlier compared to the case without disorder and the final displacement will be shorter. To understand this we have to consider automotion [105] which is the motion of the vortex wall after the end of the pulse due to the transverse displacement (potential energy) of the vortex core. Within this process the vortex core approaches its final position exponentially with a time constant that is the same for both coordinates X and Y. This results in a straight vortex core trajectory (Fig. 4.3 a) after the end of the pulse in the absence of disorder. As the restoring force, averaged over many realizations of disorder $\langle F_y \rangle = -kY$, only depends on the transverse displacement Y disorder during automotion leads to a reduction of the displace-

ment that is independent of the pulse amplitude, causing a negative offset in the displacement curves (Fig. 4.4 and Fig. 4.6).

Furthermore the slope of these curves decreases indicating that energy is transferred from the domain wall into other degrees of freedom, which are not present in the simple collective coordinates model. This could be for example spin wave modes, or distortions of the domain wall as already mentioned earlier. To allow further conclusions we quantitatively compare the experimental data (Fig. 4.6) with micromagnetic simulations that incorporate disorder. Here we investigate two possible disorder models. The first one, we call 'surface disorder', mimics surface roughness of the magnetic layer by M_s variations [108] and the second one, 'edge roughness', which models random variations of the stripe edge by randomly removing the magnetization from the outer cells at the edges. It seems reasonable to assume that both types of disorder are connected to the grains in the magnetic material and that their length scales should be of the order of nanometer to tens of nanometers. Therefore the length scale of the disorder was also varied between 2×2 and 8×8 cells in the simulations with a cell-size of $5 \times 4 \times 20$ nm^3.

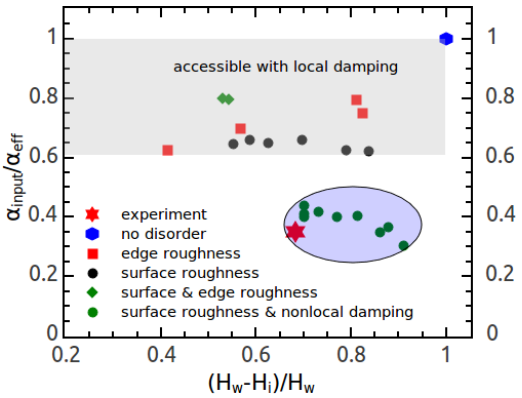

Figure 4.7: Micromagnetic domain wall displacement simulations for a 512 nm wide and 20/17 nm thick stripe of $Ni_{80}Fe_{20}$ ($M_s = 8/7.2 \cdot 10^5$ A/m, $\alpha_{\text{input}} = \alpha_{\text{FMR,exp.}} = 0.008$) with 5×4 nm^2 lateral cell-size. α_{eff} has been obtained from the slope of the linear part of the displacement vs. field plots up to the Walker breakdown field (H_w) and H_i is the intersect of that straight line with the field field axis. Although all tested kinds of modeling disorder without a nonlocal damping term lead to a reduction of α_{eff}, none fully accounts for the lower experimental value. Only simulations including a nonlocal damping parameter $\eta \approx 0.07$ nm^2 come close to the experimental value. To model surface disorder we used M_s variations between 2% and 6% on a scale between 2×2 and 8×8 cells and edge roughness was modeled by removing different portions of the outer one or two cells.

The experimental Gilbert damping parameter has been determined through local FMR measurements ($\alpha \approx 0.008$) and the simulation parameter was set accordingly. Then domain wall motion under the influence of the disorder models have been simulated and corresponding displacement curves, i.e. the displacement as a function of the pulse amplitude, have been recorded. The effective damping parameter α_{eff} was then determined from the slope of the displacement

curves according to:

$$\alpha = \gamma \Delta_T \cdot \frac{\int \mu_0 H dt}{\delta q} \tag{4.12}$$

In Fig. 4.7 we show the ratio of the Gilbert damping parameter in the simulations $\alpha_{\text{input}} = 0.008$ and the effective damping parameter α_{eff} as a function of $(H_w - H_i)/H_w$, where H_w is the Walker breakdown field and H_i the field at which the linear slope extrapolates to zero (see Fig. 4.6). Note that the depinning field is not well defined in the experiment as for decreasing fields a smoothly increasing portion of the domain walls is pinned. The ratio H_i/H_w can be determined reliably in the experiments and is not prone to calibration errors of the pulse amplitude and therefore we use a combination of H_w and H_i. Interestingly the experimental data point is separated from all the simulated data points showing a smaller slope in the displacement curves corresponding to more dissipation than in any of the simulations. Furthermore we find that increasing the disorder parameters (M_s variation or edge roughness) above a certain level primarily increases the pinning effects, but does not lead to a further increase of the effective damping parameter α_{eff}. For example the simulations with different degrees of surface roughness, which was modeled as M_s variations ranging from 2% to 6%, all show similar slopes in the displacement curves resulting in an effective damping parameter α_{eff} of about 0.012. We obtain similar values for the edge roughness simulations.

To summarize this subsection we have to say that so far we can only qualitatively reproduce the experiments in simulations and that there seems to be significantly more dissipation involved in reality than in our simulations.

4.3 Nonlocal damping

A reason for the higher dissipation rates inferred from the experiments could be that the damping term, as it is implemented in the micromagnetic simulations, only depends on the magnetization and its time derivative at a given spatial coordinate.

$$\vec{T}_\alpha(\vec{r}) = \alpha\vec{m}(\vec{r}) \times \dot{\vec{m}}(\vec{r}) \tag{4.13}$$

However, $\vec{T}_\alpha$ could also depend on the magnetic texture and nonlocal terms might have to be included [109, 110, 111], i.e. damping might not only depend on the magnetization and its time derivative at a given spatial coordinate $\vec{r}$, but also on these quantities in its vicinity [112]. These additional terms would not contribute to the damping of the uniform FMR mode, but only when large magnetization gradients are present as in narrow domain walls or vortex structures.

In [110] the authors give an analytic expression for the tensorial damping torque for conducting ferromagnets, like $Ni_{80}Fe_{20}$:

$$\vec{T}_\alpha(\vec{r}) = \vec{m}(\vec{r}) \times \left(D \cdot \dot{\vec{m}}(\vec{r})\right) \tag{4.14}$$

where D is the 3×3 differential damping tensor given by:

$$D_{\alpha\beta} = \alpha_0\delta_{\alpha\beta} + \eta \sum_i \left(\vec{m} \times \partial_i\vec{m}\right)_\alpha \left(\vec{m} \times \partial_i\vec{m}\right)_\beta \tag{4.15}$$

with α_0 the original damping parameter. Furthermore they calculate $\eta = g\mu_B\hbar G_0/(4e^2M_s)$ and estimate $\eta \approx 0.5$ nm^2 for Permalloy by using $G_0 = (5\ \mu\Omega\ \text{cm})^{-1}$ for the conductivity.

We have implemented equation (4.14) into mumax2 [17] by introducing the possibly space-dependent quantity η and rewriting the cuda [18] code. As the nonlocal damping torque includes a time derivative of the magnetization, it cannot easily be implemented as an addtional field term in mumax and therefore the file torque.cu was rewritted. Besides other quantities' dependencies, Fig. 4.8 illustrates on what quantities the torque depends on.

After checking that the new implementation with $\eta = 0$ reproduces results of the original code we performed simulations on vortex core motion in a disk. In Fig. 4.9 we show simulated spectra of the in-plane magnetization $m_x + im_y$ averaged over the whole sample. The sample is a 50 nm thick $Ni_{80}Fe_{20}$ disk of 1.6 μm diameter. The vortex ground state is excited by a δ-like in-plane field pulse and the magnetization evolution is recorded and Fourier transformed. The peaks correspond to different spin wave modes at GHz frequencies and the vortex gyrotropic mode at 250 MHz. Due to the large gradient of the magnetization around the moving vortex core, the gyrotropic mode is much more influenced by nonlocal damping than spin wave modes, whereas the Gilbert damping parameter α acts on all modes in the same way irrespective of their spatial structure. Comparing the decay of the gyrotropic mode (inset) we find that in this case $\eta = 0.1$ nm^2 corresponds to an increase of the effective Gilbert damping parameter from 0.008 to 0.030.

Ajay Gangwar has measured the temporal trajectory of a vortex core directly using STXM (Scanning Transmission X-Ray Microscopy) on a nominally equivalent sample. Fitting the trajectory a resonance frequency of 155 MHz and

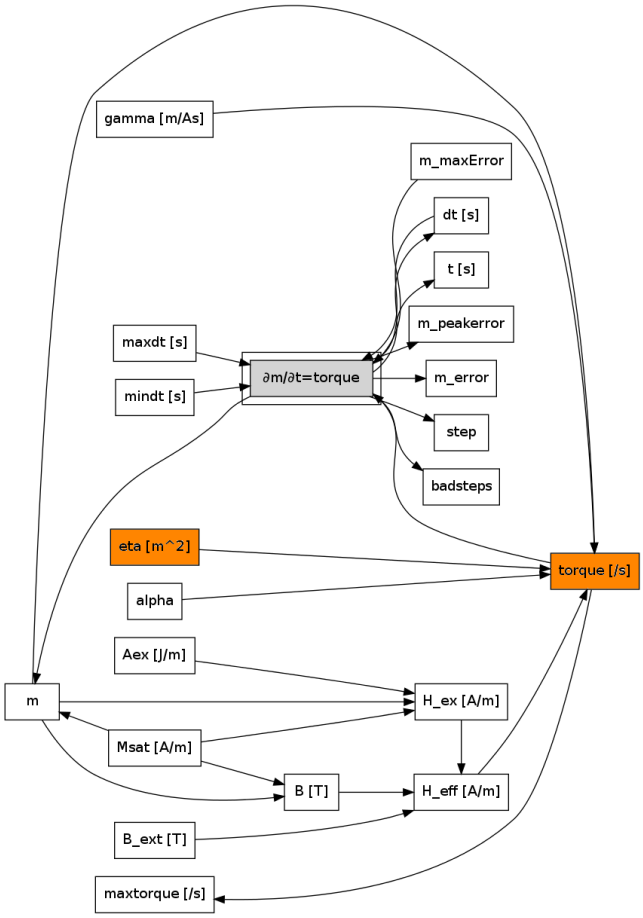

Figure 4.8: Dependency graph illustrating the relationship of relevant quantities for a simple mumax2 simulation including a nonlocal damping term. Note that the damping terms depend on the effective field via $\frac{\partial \vec{m}}{\partial t}$ and therefore cannot be modeled as effective fields themselves in this scheme.

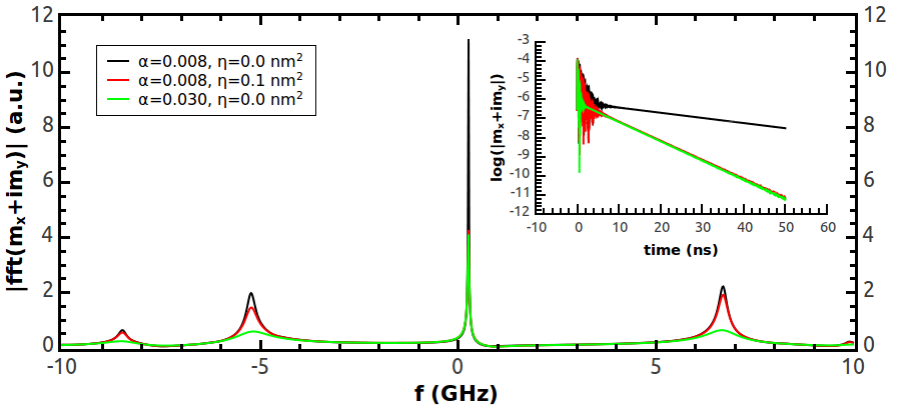

Figure 4.9: Typical Fourier spectra of the magnetic excitations in a $Ni_{80}Fe_{20}$ disk which is in the vortex ground state for three different combinations of the Gilbert damping parameter α and the nonlocal damping parameter η. Here we plot clock-wise rotating modes at positive frequencies and counter clock-wise rotating modes at negative frequencies (see also Fig. 4.10 a) - c) and the following subsection). $m_x + im_y$ captures both, the spin wave dynamics of the lowest spin wave modes as well as the low frequency gyrotropic mode. The inset displays the decay of the gyrotropic mode in the time domain as the gyrotropic mode is the only mode left after several nanoseconds. Note that the green and red curves basically fall on top of each other for the gyrotropic mode whereas they are clearly different for the spin wave modes.

a decay time for the gyro mode of 23.5 ns has been determined. Taking into account the sample geometry and material parameters [113] this corresponds to a Gilbert damping parameter $\alpha_{\text{eff}} \approx 0.023$. This experimental result can be reproduced assuming $\alpha = 0.008$ and $\eta \approx 0.07$ nm^2. In later measurements on another sample no signs for an increased damping were found and therefore no unambiguous conclusions can be drawn on whether nonlocal damping can be seen experimentally for vortex core motion in these disks or not.

We also simulate field driven vortex domain wall motion including the nonlocal damping term and also find enhanced damping of domain wall motion. In particular using $\eta = 0.07$ nm^2 and 3% surface roughness we obtain displacement curves that match much better with the experimental observation than the simulations without nonlocal damping (Fig. 4.7). From this we conclude that the experimental displacement curves show hints that disorder alone cannot explain the observations fully. Furthermore according to [110] η is given by

$$\eta = g\mu_B \hbar G_0/(4e^2 M_s) \tag{4.16}$$

where G_0 is the conductivity of the ferromagnetic metal. A value of $\eta = 0.07$ nm^2 then corresponds to a conductivity of $(37\ \mu\Omega\ \text{cm})^{-1} = 2.69 \cdot 10^6\ 1/\Omega\text{m}$, which is in reasonable agreement with values measured for $Ni_{80}Fe_{20}$ samples in our group. These samples show a typical conductivity of approximately $2 \cdot 10^6\ 1/\Omega\text{m}$ and $\mu_0 M_s = 0.92$ T.

At this point we want to remind the reader that the effect of nonlocal damping is only observable due to the large gradient in the magnetization close to

the vortex core. For spin waves of several hundred nanometer wavelength this contribution is already too small to clearly distinguish it from disorder contributions: $\alpha_{\text{eff}} = \alpha_0 + \eta k^2 + \alpha_{\text{disorder}}$, where $\eta k^2 \approx 0.0004$ and α_{disorder} is the increase in the effective damping parameter α_{eff} due to two magnon scattering at sample inhomogeneities.

Nevertheless, to our best knowledge there are no experimental values for η available in literature so far and we do not consider nonlocal damping in the next section which is not dedicated to the investigation of damping, but to interactions between spin wave modes and the vortex core gyration.

Finding that the damping parameter may have nonlocal contributions the question arises if other parameters do also show such contributions. And indeed we find significant differences between our spin wave doppler experiments where the non-adiabatic spin transfer torque parameter β was determined [66] (section 3.3) and other experiments where β has been evaluated in non-homogeneous magnetic textures. There have been different studies using vortex core dynamics and domain wall dynamics [79, 86]. As for example shown in [91] disorder corrupts the determination of β due to the local vortex structure and its interplay with the local disorder in a similar way as disorder hinders the determination of the intrinsic Gilbert damping parameter from domain wall displacement curves (section 4.2.2,[92]).

Recently, in another study [114], using static displacements of vortex cores in a $Ni_{80}Fe_{20}$ square, a value for β has been published ($\beta = 0.119 \pm 0.022$) which is significantly higher than ours ($\beta = 0.035 \pm 0.011$). As both results are not strongly influenced by errors due to disorder it is very likely that there are additional nonlocal spin-transfer torque contributions as suggested in [114] and references therein [115, 116, 117, 118].

In conclusion we investigated vortex domain wall motion in stripes. For the case of the prototypical material $Ni_{80}Fe_{20}$ without disorder we found that the existing model which uses the Thiele equation has to be extended by the concept of the critical velocity in order to explain the experimentally observed chirality dependent domain wall displacements in micron wide stripes. Including disorder then lead to the belief that even the micromagnetic model may have some shortcomings when used in its standard form without nonlocal damping.

4.4 Nonlinear vortex dynamics

Parts of this section have been published in Physical Review Letters 112, 077201 (2014) [119] and in Applied Physics Letters 104, 012409 (2014) [120].

Dipolar interactions favor a flux closed configuration of the magnetization in magnetic micro and nano-sized objects. Similar to the vortex domain walls in the last subsection the magnetization in flat cylindrical elements curls around the edges of the element in one of the two possible senses: clockwise (CW) or counter-clockwise (CCW). As the magnitude of the magnetization vector is preserved, the magnetization at the center of the disk has to form an out of plane magnetized vortex core [121] which can either point up or down. In principle this allows to store two bit (2 circulations $\times$ 2 polarities) of information in each vortex. Furthermore the flux closed vortex structure is energetically stable in a practically usable range of thickness to diameter ratios and allows close packing required e.g. for high speed magnetic memory applications referred to as vortex random access memory (VRAM) [122, 123, 124, 125].

The translational motion of the vortex core is described by the Thiele equation [96, 97] already introduced in this section (4.3). The free vortex core motion follows a spiral back to its equilibrium position in the middle of the disk with an eigenfrequency of 50 MHz to 1 GHz. This gyro-frequency is determined by the harmonic potential which in turn is due to dipolar fields and therefore depends on the aspect ratio of the magnetic element [126]. The sense of gyration depends on the polarity of the vortex core and hence breaks the symmetry of the dipole dominated spin wave eigenmodes [100, 127, 128] which are characterized by the number of azimuthal and radial nodal lines (m, n) [129, 130, 131].

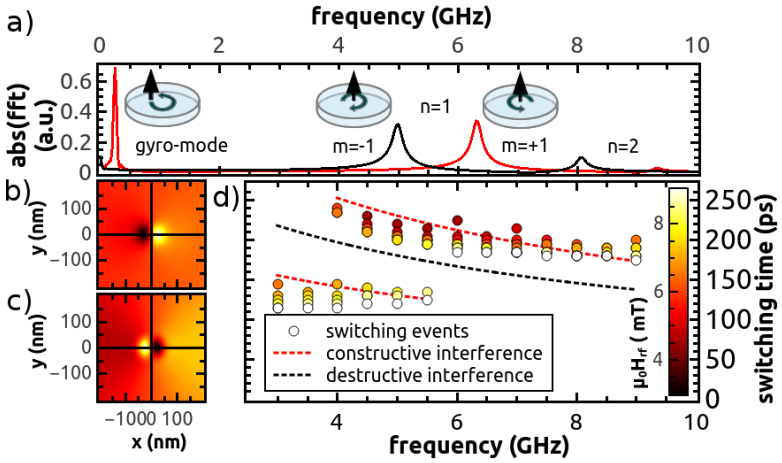

Figure 4.10: a) The lowest excitations of the magnetization in a Permalloy disk (diameter = 1.6 μm, thickness = 50 nm) are the gyrotropic vortex mode (gyration frequency 250 MHz), followed by the $n = 1$, $m = \pm 1$ spin wave modes found at 5 GHz and 6.25 GHz, respectively [132]. Their spatial mode structures close to the disk center for polarity up ($p = +1$) are shown in b) and c) respectively. d) shows switching times compared to a simple picture of interference of these two modes.

In the following we use a 50 nm thick disk of $Ni_{80}Fe_{20}$ with a diameter of 1600 nm for our numerical investigations [17] and for comparison with the experiments. The simulation parameters have been set to: $M_s = 7.6 \cdot 10^5$ A/m, α=0.006 and $A_{\text{exch.}} = 1.3 \cdot 10^{-12}$ J/m on a two-dimensional grid with 512 by 512 cells. The linear eigenmodes shown in Fig. 4.10 a) are the starting point of our study and illustrate the resonances of the gyro-mode and the characteristics of the lowest spin wave modes (Fig. 4.10 b and c) in our sample.

Technologically, fast and selective switching of the vortex core polarity is needed for a memory device. Dynamic excitations using magnetic field bursts [103] or pulses [133, 134] have been used to achieve fast reversal and rotating field excitations have been used to solve the selectivity problem [135, 132]. Recently rotating spin wave eigenmodes have also been used for vortex polarity reversal [132].

Although there are multiple ways to reverse the core polarity the mechanism is often the same [103, 128]: First a region of enhanced out-of-plane magnetization anti-parallel to the vortex core (a 'dip') is formed. This is due to gauge fields that arise due to the motion of a rigid vortex core in its vicinity. Then a vortex/anti-vortex (V/AV)-pair is formed (right hand side of Fig. 4.13) and the anti-vortex of opposite polarity annihilates with the original vortex leaving the new vortex with 'reversed' polarity behind.

But not only the gauge fields coming from the gyro motion [128], but also dynamic fields due to rotating magnetic fields [136], or spin waves [132] and their combinations facilitate the reversal. For example in the case of gyro motion and spin waves their out-of-plane fields add up as argued in [132].

Even for fast vortex core switching as in [137] this seems to be a good model. The authors used in-plane rotating field bursts of one period duration and carrier frequencies of $4.5 - 10$ GHz. The broad spectrum of the short pulse excites both $m = \pm 1, n = 1$ modes, that rotate around the center in opposite directions and their constructive interference increases the probability for a V/AV-pair nucleation. The clustering of data points around switching times that correspond to constructive interference (Fig. 4.10 d) strongly supports this simple model.

We will go into more details of the fast reversal later. We just want to add here that due to the broad excitation spectrum of short bursts we also expect to find a broader region around the resonances where vortex core polarity reversal is possible below a certain threshold amplitude. For (quasi) continuous sinusoidal excitations, one expects a reduced threshold only in a frequency range of roughly a linewidth around the spin wave resonances [132].

However, a combination of quasi continuous low and high frequency excitations showed a surprising switching diagram [120]. It featured very low switching thresholds for frequencies between the gyro- and spin wave resonances, i.e. for a range where no resonances have been known to exist (Fig. 4.11).

The excitation scheme in these experiments was such that the vortex gyro motion was excited to a finite gyration radius prior to the excitation of the spin waves by high frequency magnetic fields. In order to study spin wave dynamics for this situation we introduce a coordinate system that rotates with the frequency of the gyro-excitation (250 MHz) around the disk center [136]. In this reference frame the circular gyro-motion turns into a static background magnetization and additional spin wave modes can be seen as small perturbations of that (back-) ground state. Note that a little care has to be taken as the frequencies of rotating spin wave modes seem to be shifted. For example the

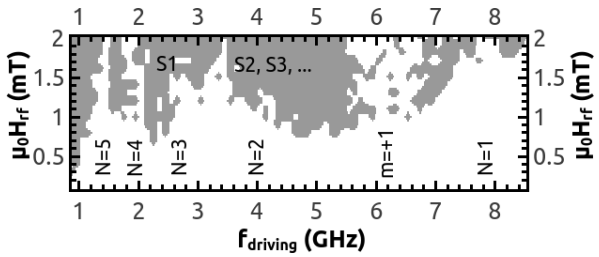

Figure 4.11: Reversal of the core polarity was achieved in the gray area for the following combination of low- and high-frequency in-plane field excitations: first the gyromotion (250 MHz) of the vortex core was excited for 30 ns by a CCW-rotating field of 0.125 mT amplitude. Then a high frequency ($f = f_{\mathrm{driving}}$) clockwise-rotating excitation of 24 periods duration and amplitude H_{rf} was added. In a simple picture reversal was expected to occur only in a region of about 1 GHz width around the resonance of the $m = -1$ mode at 5 GHz. For comparison with Fig. 4.12 and Fig. 4.13 the spin wave modes S1, S2, ... and higher harmonic excitations N have been included.

$m = -1$ mode appears shifted upwards by 250 MHz and the $m = +1$ mode downwards by the same amount.

By changing the gyro-radius the spin wave spectrum also changes. First we have to notice that the vortex core displacement away from the center breaks the rotational symmetry of the system and second, the dynamic gyro-field, which is a static gauge field in the rotating frame, causes the 'dip' on one side of the vortex core.

Due to the lack of the rotational symmetry analytical models are difficult and therefore we performed micromagnetic simulations. Fig. 4.12 shows color encoded the evolution of the spin wave spectrum as a function of the gyro excitation amplitude $\mu_0 H_{\mathrm{gyro}}$, where dark red lines indicate a strong response to a weak $\delta-$like uniform field pulse.

These spectra are obtained with micro magnetic simulations [17] that started with the vortex core in the middle of the disk. Then the gyro-motion was excited with an in-plane rotating field of 250 MHz for about 100 ns. During that time the vortex core reached a circular trajectory with a radius that depends on the amplitude of the gyro-excitation field. An additional short and low amplitude uniform field pulse after 100 ns excited high frequency spin wave modes which are then transformed into the rotating reference frame. The temporal evolution of the recorded magnetic configuration after the pulse was first transformed into the rotating reference frame and then Fourier transformed in order to obtain the spectra shown in Fig. 4.12.

The gyration induces much more complicated spectra than without gyro-excitation: more modes can be distinguished and their resonance frequencies strongly depend on the gyro-radius. In more detail, we observe different behavior for the $m = -1$ (5 GHz) and $m = +1$ (6.25 GHz) modes. While the resonance of the $m = +1$ mode is basically left unaffected, the resonance of the $m = -1$ mode splits up into a series of distinct modes labeled S1, S2, ... when the gyro-radius is increased up to 150 nm. As exemplified in the inset of

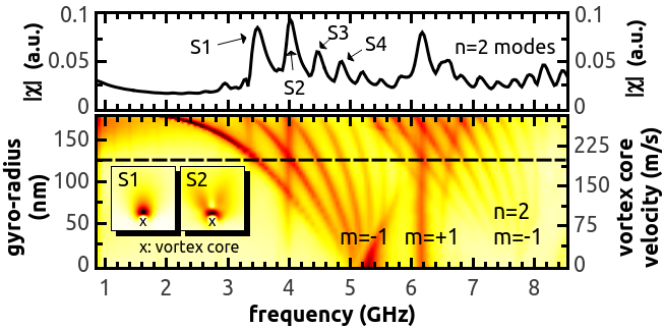

Figure 4.12: When the VC is at the center of the disk the Fourier spectrum of M_z shows the two lowest spin wave modes around 5 and 6 GHz. Displacing the VC breaks the rotational symmetry and gives rise to a richer spectrum. Single spin wave spectra like that for a gyro-radius of 125 nm (dashed line) are color encoded and combined to show the evolution of the spectra with the gyro-radius and the VC velocity. The insets show two spin wave mode profiles in a 400 by 400 nm^2 region around the disk center.

Fig. 4.12 these modes are located in the region of the dip and the number of nodes increases with frequency. Of particular interest is the lowest frequency spin wave mode S1, as it approaches zero frequency when the vortex core reaches the critical velocity of about 300 m/s. It is therefore this mode that becomes more and more localized in the dip and goes soft, i.e. the effective potential becomes shallow, the corresponding restoring forces vanish and the unstable magnetization reverses.

Due to the broken rotational symmetry caused by the finite displacement of the vortex core additional modes, that could not be excited with a uniform field pulse in absence of gyro-motion, can also be observed. Most prominent is a mode that elliptically deforms the vortex core at a resonance frequency of 4 GHz which does not depend on the gyro-radius [120].

The spectrum for a gyro-radius of about 125 nm is explicitly shown in Fig. 4.12 because the corresponding gyro-excitation field of 0.125 mT is the same as for the switching diagram (Fig. 4.11). But while for this case the lowest frequency spin wave resonance S1 is around 3.5 GHz, the additional excitation of spin waves by a continuously clockwise rotating in-plane uniform field leads to very low thresholds for even smaller frequencies below 3 GHz. Hence the switching diagram (Fig. 4.11) is still not well explained.

So far we only considered small amplitude (linear) excitations, but no effects that are nonlinear in the spin wave excitation amplitude. For example the GHz magnetic fields also excite the vortex core to gyrate on a small orbit. Although the radius of the motion is small the higher frequency compared to the gyro-frequency means a significant vortex core velocity due to the GHz excitation. The increased vortex core velocity is therefore expected to cause a further frequency down-shift of the spin wave modes facilitating the polarity reversal at lower frequencies.

In the next step we go beyond the linear spin wave regime in order to investigate effects of finite spin wave amplitude in more detail.

One difficulty in dealing with nonlinear phenomena is to find observables that contain the important information and leave out most of the irrelevant and linear dynamics.

As we want to investigate spin waves and the gyro-motion in the nonlinear regime we focus on the M_z-component of the spatially averaged magnetization which is particularly sensitive to (non) linear interactions. This becomes apparent when one considers that the azimuthal dependence of M_z is given by $\exp(im\varphi)$ for the spin waves and vanishes for all modes with $m \neq 0$. The rotational symmetry also forbids time dependent contributions of the pure gyro motion to M_z. Thus, only simultaneous spin wave and gyro-excitations are reflected in the out-of-plane magnetization M_z.

As already mentioned we expect nonlinear behavior that ultimately leads to the polarity reversal. As an instability process its rate of change depends on the excess of driving over damping. In order to slow down the instability process which allows for a reasonable resolution in time and in frequency we keep the rf-excitation amplitude small at 0.1 mT. In this way we can use 10 ns time windows centered at time t_0 after the start of the rf-excitation for the windowed Fourier transforms shown in Fig. 4.13.

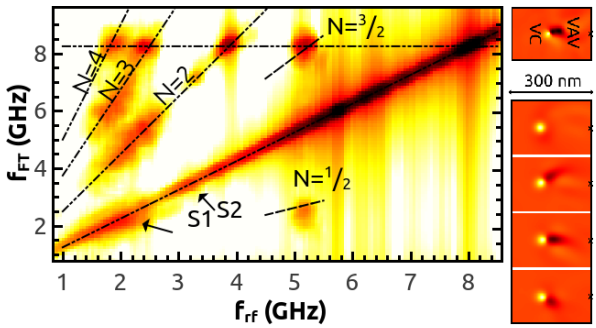

Figure 4.13: Windowed power spectra 24 ns (= t_0) after the rf-excitation of 0.1 mT amplitude started. Especially the soft spin wave mode S1 shifts further to lower frequencies during the rf-excitation. The response in Fourier-frequency space (f_{FT}) indicates excitation of modes also at harmonics $N \cdot (f_{\mathrm{rf}} + 0.25\ \mathrm{GHz})$ of the excitation frequency f_{rf}. On the right side snapshots of the out-of-plane magnetization are shown illustrating the similarity between the V/AV-pair that forms between the vortex core and the disk center (marked by x) and the non-harmonic interference pattern shown at four different times within one excitation period.

Simulated power spectra taken for $t_0 = 24$ ns are shown in Fig. 4.13 using a logarithmic color scale. It confirms that the modes S1 and also S2 shift further to lower frequencies. In particular the resonance of the spin wave mode S1 is now found below 2.5 GHz and it is approaching zero frequency and going soft. Apart from the response at the excitation frequency a strong response is also found for higher harmonics of the rf-excitation frequency. This is in particular the case for the S1 mode and whenever a mode/modes around 8 GHz can be excited by subharmonic frequencies.

An explanation for the high harmonic components for modes localized at

the dip region could read as follows: The 'dip' region is characterized by small stiffness fields and relatively large susceptibilities can be expected. The basic idea is now to look at the nonlinear interference of localized modes with the 'dip' as a repeated and partial creation and annihilation of V/AV-pairs. This process involves highly anharmonic magnetization precession that is still periodic with the excitation period providing the possibility to couple with higher harmonic frequencies.

The reason why especially the mode around 8 GHz is excited might be found in the fact that this/these modes are characterized by an additional radial node compared to the modes S1, S2, ... and that they are also located near the 'dip' but have a larger extent about the size of the gyro-radius.

Finally, we provide an explanation for the switching diagram obtained by Sproll et al. [120] using the results discussed so far. For that the experimental excitation parameters, i.e. 24 excitation periods of amplitude $\mu_0 H_{\mathrm{rf}}$ up to 2 mT and rotating in the plane have been used in micromagnetic simulations.

For a gyro-field amplitude of $\mu_0 H_{\mathrm{gyro}} = 0.125$ mT a switching diagram has been simulated (Fig. 4.11) where gray color indicates that the vortex core polarity after the end of the simulation was opposite to the initial polarity. In a region from 3.5 to 7.5 GHz the threshold amplitude is low except around 6 GHz. Comparing this with the linear spin wave spectrum (Fig. 4.12) leads to the conclusion that the broad reduction is due to the modes originating from the $m = -1$ mode which reach down to 3.5 GHz (S1 mode) and the gap is due to the $m = +1$ mode. The switching diagram seems to have a gap, but in reality this occurs because the polarity is switched twice as once the polarity is reversed the $m = +1$ mode can be excited by the CW rotating field and the reversal threshold is smaller than for the $m = -1$ mode. Therefore the initial vortex core polarity is restored by the second reversal process within about a linewidth around the $m = +1$ resonance line.

The generation of higher harmonic spin waves was already observed for amplitudes as low as 0.1 mT in Fig. 4.13 and the nonlinear resonances of the S1 mode ($N = 5, 4, 3$ in Fig. 4.13; $N = 5$ is not visible due to the limited time resolution) thus explain the abrupt increase of the switching threshold at 1.4, 1.8, and 2.5 GHz. For these frequencies energy is transferred away from the S1 mode and into the less confined mode at 8 GHz. This increases the effective damping for the S1 mode and hence the switching threshold.

For frequencies below 1 GHz the off-resonant excitation of the gyro-mode is responsible for the low switching threshold.

To summarize, we found in this subsection that the magnetic excitations of a disk in the vortex ground state, namely the gyro-motion and spin wave excitations, show interesting interactions. First the gyration of the vortex core breaks the rotational symmetry and alters the linear spin wave spectrum quite drastically and then interactions between the vortex core and the spin wave modes may also lead to scattering into other spin wave modes or to the reversal of the vortex core polarity.

4.5 Linear interference in pulsed experiments

As already mentioned Kammerer et al. [137, 138] investigated switching of the vortex core polarity in the same kind of samples as in reference [120] discussed above. The authors used short bursts of rotating in-plane magnetic fields to excite spin wave modes in a magnetic disk and thereby reversed the vortex core polarity on a sub-nanosecond time scale. Here we discuss more details of the involved magnetization dynamics and its consequences for the vortex core polarity reversal diagrams (Fig. 4.14).

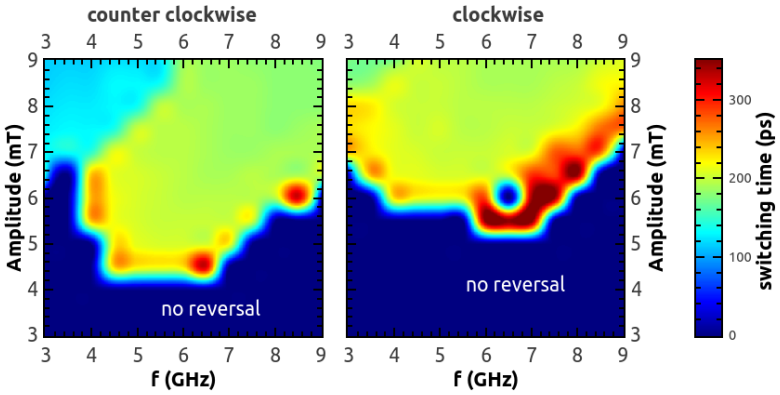

Figure 4.14: Switching diagrams displaying the switching time, i.e. the time from the beginning of the one period long rotating pulse till the first polarity reversal process as a function of the driving frequency and amplitude. In both cases we observe a broad region around the spin wave resonances where the amplitude, necessary for switching, reaches its minimum. The switching times are almost constant ($\approx$ 200 ps) over large regions of the switching diagram although the driving amplitudes are significantly different.

Due to the short duration of the burst of only one period of the excitation the spectral width is quite broad and it is possible to excite two modes at the same time. Especially the $n = 1, m = \pm 1$ modes, whose resonance frequencies are separated by approximately 1 GHz for our particular geometry couple both to the homogeneous excitation field.

In order to get a brief overview of the temporal interference due to these two modes we define $m := m_x + im_y$ as the average over the whole sample magnetization and split it into contributions $m = m_+ + m_-$ from the two spin wave modes $n = 1, m = \pm 1$. Starting from the Landau-Lifshitz equation one can again derive an equation of motion for $m_\pm$. Without proof the equation is very simple due to the rotational symmetry and reads:

$$\dot{m}_\pm = i\omega_\pm m_\pm + F_\pm e^{i\omega t} \tag{4.17}$$

where $\omega_\pm$ are the eigenfrequencies and $F_\pm$ the coupling to the driving field of frequency $f = \omega/2\pi$. Note that $f < 0$ means clockwise rotating field excitation and $f > 0$ counter clock wise and therefore also ω_- is negative (corresponds to clockwise rotating mode $m = -1$) and ω_+ is positive (all for $p = +1$). Time

integration of eq. 4.17 leads to

$$m_{\pm}(t) = \frac{iF_{\pm}}{\omega_{\pm} - \omega} \left(e^{-i\omega_{\pm} t} - e^{-i\omega t} \right) \tag{4.18}$$

for $t \leq 2\pi/\omega = T$ and

$$m_{\pm}(t) = m_{\pm}(T) e^{-i\omega_{\pm} t} \tag{4.19}$$

for $(t > T)$. Note that due to damping the eigenfrequencies are complex and all terms are finite and well defined.

In order to check whether this simplified model possibly includes the relevant physics we fitted the traces of $|m| = |m_x + im_y|$ for clockwise and counter clockwise rotating excitation fields of 5.5 GHz frequency and 4.5 mT amplitude simultaneously to $|m| = |m_+ + m_-|$. The results are shown in table 4.1.

	$\omega_-/2\pi$ (GHz)	$\omega_+/2\pi$ (GHz)
best fit	-4.7-0.9i	7.2-0.18i
std deviation	0.5, 0.4i	0.7, 0.25i
	F_+	F_-
best fit	$0.9e^{-0.42i}$	$-0.57e^{-0.37i}$
std deviation	0.1, 0.18	0.05, 0.30

Table 4.1: Precession frequencies and amplitudes of the $n = 1, m = \pm 1$ modes obtained by fitting micromagnetic simulation data.

Although by checking other driving frequencies and amplitudes we noticed that the fit parameters slightly depend on the driving frequency and amplitude we find that both modes couple with approximately the same amplitude to the external driving field.

Interestingly the relaxation times are different:
$\tau_- \approx 1/(2\pi \cdot 0.9)$ ns $= 0.18$ ns and $\tau_+ \approx 1/(2\pi \cdot 0.18)$ ns $= 0.88$ ns. While relaxation of the $m = +1$ mode seems to be close to typical intrinsic relaxation rates, the $m = -1$ mode has an increased relaxation rate which hints at coupling to other spin wave modes.

To compare the switching times, i.e. the time after the beginning of the burst when the first reversal occurs with our simple interference model, we approximately set $F_+ = -F_- = F$ in eq. 4.18 and use the eigenfrequencies already determined earlier in micromagnetic simulations for $\omega_\pm$. Fig. 4.15 shows color-encoded times of constructive (dark red) and destructive interference, i.e. $|m| = |m_+ + m_-|$ and a clear preference of switching for constructive interference. Thus the simple picture seems to hold in this case, i.e. the effective fields of both spin wave modes add to the gyro-field of the vortex core and stimulate the polarity reversal.

4.6 Different behavior for CW and CCW excitation

The behavior of the magnetization dynamics above the switching threshold is significantly different for CW and CCW excitation as simulated and measured

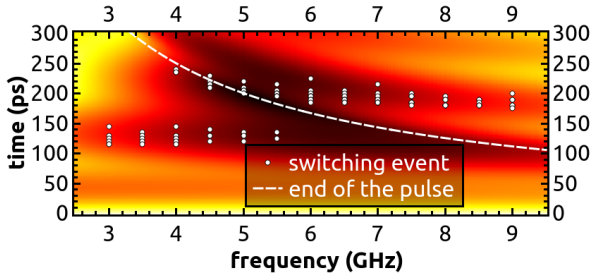

Figure 4.15: Constructive interference of both spin wave modes $n = 1, m = \pm 1$ visible as maxima of $|m(t)| = |m_+ + m_-|$ (dark red) initiate vortex polarity switching events within a relatively broad frequency range. The color-encoded interference pattern was calculated with the simple model, while the switching events have been observed in full micromagnetic simulations with CCW excitation amplitudes up to 9 mT.

by Kammerer et al. [137, 138]. In particular it was observed that multiple reversals occurred for CW excitation already very close above the threshold. It is important to understand the reasons for this behavior as for data storage technology it is vital to achieve selective reversal, i.e. reversal of only one type of core polarity. It is clear that this becomes more and more complicated when the burst length is decreased because the spectral width increases and therefore the difference between excitation of one over the other polarity mode vanishes. But the different behavior above the threshold (i.e. multiple reversals or only a single reversal) cannot be explained like this.

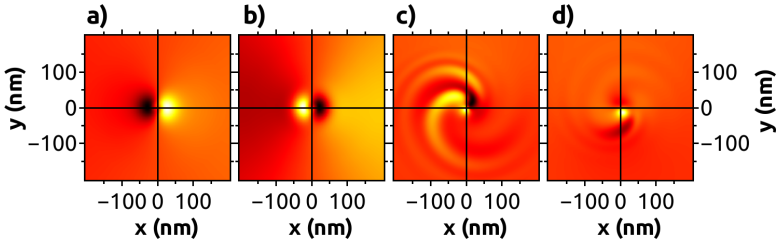

Figure 4.16: Mode profiles M_z of the $n = 1, m \pm 1$ mode in a) and b) and snapshots of the out-of-plane dynamic magnetization after 250 ps demonstrating the difference in magnetization dynamics involved in core polarity reversal. The excitation amplitude was 5 mT and the carrier frequency 5.5 GHz. While in the CW case c) a spiral like structure forms, the CCW case displays a less complicated and more localized pattern d) which consists mainly of the $m = +1$ mode.

We begin the explanation with a look at two snapshots of the out-of-plane magnetization after 250 ps for CW and CCW excitation with 5 mT amplitude (Fig. 4.16 c and d). While we observe a spiral like structure for the CW case the dynamic magnetization is much more confined to the center of the disk in the

CCW case. The spiral structure is not a single mode neither a nonlinear effect as it also appears for small excitation amplitudes and vanishes again after about 300 ps. It is a superposition of (linear) $m > 0$ modes that dephase after a short time due to different resonance frequencies. In fact the eigenfrequencies for the lowest clockwise rotating modes are approximately 5 and 8 GHz, i.e. their separation is 3 GHz and dephasing is expected to happen within approximately a third of a nanosecond. Furthermore the observation made earlier that the relaxation time for the $m = -1$ mode is significantly increased is a hint that the higher spin wave modes are excited by the $m = -1$ spin wave mode which thereby loses energy and amplitude faster than expected for a single mode decay.

Finally when we believe that the sum of all effective fields is responsible for the creation of the V/AV-pair, we easily understand why for the CW case the reversal is more complicated than in the CCW case. In the CW case V/AV-pairs form in the spiral arms and due to the larger separation between the anti-vortex and the original vortex the reversal does not take place and the anti-vortex annihilates with its own vortex instead of the original vortex core, or even multiple V/AV-pairs are created. All this leads to less predictable and reliable reversal behavior after the end of the burst. As each single annihilation event was also detected as a 'switching event' in [137] this was termed multiple reversals in the paper. This narrows the region in parameter space (frequency and amplitude) where reliable selective reversal can be achieved.

Reviewing the results of the previous subsection where nonlinear processes lead to the excitation of a spin wave mode at around 8 GHz (Fig. 4.13) it seems likely that the same nonlinear processes are at work in both cases.

Note that in both cases the excitation of the 8 GHz mode acts against a reliable polarity reversal by increasing the threshold and by leading to the creation of additional V/AV-pairs. Therefore it seems desirable to avoid these kinds of interactions. On the other hand the question arises if these spin wave modes can also be used in an advantageous way by inverting the interaction precesses.

In conclusion interactions of the vortex core with spin wave modes in a micron sized disk have been investigated and a surprising wealth of spin wave modes and interactions has been found to contribute to the vortex polarity reversal process. Due to the difficulty of dealing with a combination of topological and wave like excitations in the nonlinear regime the work in this section strongly relied on micromagnetic simulations and an adequate analysis of the obtained data (> 1 TByte).

Summary

In this thesis the magnetization dynamics in thin ferromagnetic films and nanostructures has been studied experimentally and numerically. In particular we studied nonlinear spin wave dynamics in a plane film whereby we measured the magnon density and relaxation times and found an instability which was not reported to our knowledge. Detailed theoretical considerations then lead to an improved understanding of nonlinear spin wave dynamics in the low frequency regime [139].

Then spin wave propagation was studied in stripes and antidot lattices. It was found that the spin waves in the antidot lattice behaved like propagating in an effective medium [72] and that by matching the wave vector spin waves can be injected from the plane film into the antidot-lattice [67]. In the stripes anticrossings in the dispersion relation of spin waves have been found [68] and the dispersion relation has been used to extract the spin transfer torque parameters (P and β) when the propagating spin waves interacted with an electric current [66].

And finally vortex structures as well as their interactions with spin wave modes have been investigated in the last section. In disks linear and nonlinear effects of the interaction of spin wave modes with the gyrating vortex core have been found and the reversal behavior of the vortex core polarity was investigated [120, 119]. In the case of vortex domain walls effects of disorder, nonlocal damping [92] and chirality dependent Walker breakdown [99] have been studied.

Furthermore, contributions have been made to the work of Martin Obstbaum [140] and Ajay Gangwar [141] in particular on the anisotropic magneto resistance (AMR), of Matthias Kronseder [4] on numerical simulations of domain patterns, of Frank Hoffmann on simulations for GaMnAs [142] and Markus Härtinger on nonlinear magnetization dynamics in disks and Martin Decker on confined spin wave modes.

Publications

1. [19] H. T. Nembach, **H. Bauer**, J. M. Shaw, M. L. Schneider, and T. J. Silva, Applied Physics Letters **95**, 062506 (2009). 'Microwave assisted magnetization reversal in single domain nanoelements'

2. [67] S. Neusser, G. Duerr, **H. G. Bauer**, S. Tacchi, M. Madami, G. Woltersdorf, G. Gubbiotti, C. H. Back, and D. Grundler, Phys. Rev. Lett. **105**, 067208 (2010). 'Anisotropic Propagation and Damping of Spin Waves in a Nanopatterned Antidot Lattice'

3. [72] S. Neusser, **H. G. Bauer**, G. Duerr, R. Huber, S. Mamica, G. Woltersdorf, M. Krawczyk, C. H. Back, and D. Grundler, Phys. Rev. B **84**, 184411 (2011). 'Tunable metamaterial response of a $Ni_{80}Fe_{20}$ antidot lattice for spin waves'

4. [142] G. Woltersdorf, F. Hoffmann, **H. G. Bauer**, and C. H. Back, Phys. Rev. B **87**, 054422 (2013). 'Magnetic homogeneity of the dynamic properties of (Ga,Mn)As films from the submicrometer to millimeter length scale'

5. [4] M. Kronseder, M. Buchner, **H. Bauer**, and C. Back, Nature Communications **4** (2013). 'Dipolar-energy-activated magnetic domain pattern transformation driven by thermal fluctuations'

6. [120] M. Sproll, M. Noske, **H. Bauer**, M. Kammerer, A. Gangwar, G. Dieterle, M. Weigand, H. Stoll, G. Woltersdorf, C. H. Back, and G. Schütz, Applied Physics Letters **104**, 012409 (2014). 'Low-amplitude magnetic vortex core reversal by non-linear interaction between azimuthal spin waves and the vortex gyromode'

7. [66] J.-Y. Chauleau, **H. G. Bauer**, H. S. Körner, J. Stigloher, M. Härtinger, G. Woltersdorf, and C. H. Back, Phys. Rev. B **89**, 020403 (2014). 'Self-consistent determination of the key spin-transfer torque parameters from spin-wave Doppler experiments'

8. [119] **H. G. Bauer**, M. Sproll, C. H. Back, and G. Woltersdorf, Phys. Rev. Lett. **112**, 077201 (2014). 'Vortex Core Reversal Due to Spin Wave

Interference'

9. [140] M. Obstbaum, M. Härtinger, **H. G. Bauer**, T. Meier, F. Swientek, C. H. Back, and G. Woltersdorf, Phys. Rev. B **89**, 060407 (2014). 'Inverse spin Hall effect in $Ni_{81}Fe_{19}$ normal-metal bilayers'

10. [68] **H. G. Bauer**, J.-Y. Chauleau, G. Woltersdorf, and C. H. Back, Applied Physics Letters **104**, 102404 (2014). 'Coupling of spinwave modes in wire structures'

11. [92] accepted for publication in Physical Review Letters: T. Weindler, **H. G. Bauer**, R. Islinger, B. Boehm, J.-Y. Chauleau, and C. H. Back (2014). 'Magnetic Damping: Domain Wall Dynamics vs. Local Ferromagnetic Resonance'

12. [139] submitted: **H. G. Bauer**, P. Majchrak, T. Kachel, C. H. Back, and G. Woltersdorf (2014). 'Non-linear spin-wave excitation at low bias fields'

13. [99] in preparation: R. Islinger, T. Weindler, **H. G. Bauer**, J.-Y. Chauleau and C. H. Back (2014). 'Chirality dependent mechanism for Vortex-Wall Polarity Reversal'

14. [141] in preparation: A. Gangwar, **H. G. Bauer**, J.-Y. Chauleau, M. Noske, M. Weigand, H. Stoll, G. Schütz, and C. H. Back. (2014). 'Electrical determination of vortex states in a sub-micron magnetic element'

Bibliography

[1] L. D. Landau and E. M. Lifshitz, Phys. Z. Sowjetunion **8**, 153 (1935)

[2] B. Heinrich and J. Cochran, Advances in Physics **42**, 523 (1993)

[3] J. R. Macdonald, Proceedings of the Physical Society. Section A **64**, 968 (1951)

[4] M. Kronseder, M. Buchner, H. Bauer, and C. Back, Nature Communications **4** (2013)

[5] T. L. Gilbert, Phys. Rev. **100**, 1243 (1955)

[6] T. L. Gilbert, IEEE Trans. Mag. **40**, 3443 (2004)

[7] L. Berger, Journal of Applied Physics **55** (1984)

[8] L. Berger, Phys. Rev. B **54**, 9353 (1996)

[9] J. Slonczewski, Journal of Magnetism and Magnetic Materials **159**, L1 (1996)

[10] S. Zhang and Z. Li, Phys. Rev. Lett. **93**, 127204 (2004)

[11] A. Thiaville, Y. Nakatani, J. Miltat, and Y. Suzuki, EPL (Europhysics Letters) **69**, 990 (2005)

[12] C. Abert, L. Exl, F. Bruckner, A. Drews, and D. Suess, Journal of Magnetism and Magnetic Materials **345**, 29 (2013)

[13] A. Kakay, E. Westphal, and R. Hertel, IEEE transactions on magnetics **46**, 2303 (2010), record converted from VDB: 12.11.2012

[14] R. Chang, S. Li, M. V. Lubarda, B. Livshitz, and V. Lomakin, Journal of Applied Physics **109**, 07 (2011)

[15] T. Fischbacher, M. Franchin, G. Bordignon, and H. Fangohr, Magnetics, IEEE Transactions on **43**, 2896 (2007)

[16] M. J. Donahue and D. G. Porter, "oommf-computer code, http://math. nist. gov/oommf,"

[17] A. Vansteenkiste and B. V. de Wiele, Journal of Magnetism and Magnetic Materials **323**, 2585 (2011)

[18] J. Nickolls, I. Buck, M. Garland, and K. Skadron, Queue **6**, 40 (2008)

[19] H. T. Nembach, H. Bauer, J. M. Shaw, M. L. Schneider, and T. J. Silva, Applied Physics Letters **95**, 062506 (2009)

[20] J. H. E. Griffiths, Nature **158**, 670 (1946)

[21] C. Kittel, Phys. Rev. **73**, 155 (1948)

[22] D. Polder, Philosophical Magazine Series 7 **40**, 99 (1949)

[23] I. Neudecker, G. Woltersdorf, B. Heinrich, T. Okuno, G. Gubbiotti, and C. Back, Journal of Magnetism and Magnetic Materials **307**, 148 (2006)

[24] E. Schlömann, J. J. Green, and U. Milano, Journal of Applied Physics **31**, S386 (1960)

[25] V. E. Zakharov, V. S. L'vov, and S. S. Starobinets, Usp. Fiz. Nauk **114**, 609 (1974); [Sov. Phys. Usp. **17**, 896 (1975])

[26] V. E. Zakharov, V. S. L'vov, and S. S. Starobinets, Sov. Phys. Usp. **17**, 896 (1975)

[27] P. Krivosik and C. E. Patton, Phys. Rev. B **82**, 184428 (2010)

[28] B. A. Kalinikos and A. N. Slavin, Journal of Physics C: Solid State Physics **19**, 7013 (1986)

[29] V. L'vov, *Wave Turbulence Under Parametric Excitation* (Springer, Berlin, 1994)

[30] R. M. White and M. Sparks, Phys. Rev. **130**, 632 (1963)

[31] G. Bertotti, I. Mayergoyz, and C. Serpico, Physica B: Condensed Matter **306**, 106 (2001)

[32] I. Mayergoyz, G. Bertotti, and C. Serpico, *Nonlinear Magnetization Dynamics in Nanosystems* (Elsevier Science, 2008)

[33] J. Goulon, A. Rogalev, F. Wilhelm, N. Jaouen, C. Goulon-Ginet, and C. Brouder, The European Physical Journal B - Condensed Matter and Complex Systems **53**, 169 (2006)

[34] D. A. Arena, E. Vescovo, C.-C. Kao, Y. Guan, and W. E. Bailey, Phys. Rev. B **74**, 064409 (2006)

[35] H. Suhl, Phys. Rev. **101**, 1437 (1956)

[36] G. Woltersdorf and C. H. Back, Phys. Rev. Lett. **99**, 227207 (2007)

[37] M. Sparks, *Ferromagnetic relaxation theory* (McGraw-Hill, New York, 1964)

[38] A. G. Gurevich and G. A. Melkov, *Magnetization Oscillations and Waves* (CRC Press, Boca Raton, 1996)

[39] H. Suhl, J. Phys. Chem. Solids **1**, 209 (1957)

[40] C. E. Patton, Phys. Rep. **103**, 251 (1984)

[41] G. de Loubens, V. V. Naletov, and O. Klein, Phys. Rev. B **71**, 180411 (2005)

[42] K. Gilmore, Y. U. Idzerda, and M. D. Stiles, Phys. Rev. Lett. **99**, 027204 (2007)

[43] K. J. Harte, Journal of Applied Physics **39**, 1503 (1968)

[44] F. Schwabl, *Quantenmechanik (QM I):*, Springer-Lehrbuch (Springer, 2002) ISBN 9783540431060

[45] F. Bloch, Zeitschrift für Physik A Hadrons and Nuclei **52**, 555 (1929)

[46] H. M. Olson, P. Krivosik, K. Srinivasan, and C. E. Patton, Journal of Applied Physics **102**, 023904 (2007)

[47] A. Y. Dobin and R. H. Victora, Phys. Rev. Lett. **90**, 167203 (2003)

[48] T. Gerrits, P. Krivosik, M. L. Schneider, C. E. Patton, and T. J. Silva, Phys. Rev. Lett. **98**, 207602 (2007)

[49] T. J. Silva, C. S. Lee, T. M. Crawford, and C. T. Rogers, Journal of Applied Physics **85**, 7849 (1999)

[50] C. Bi, X. Fan, L. Pan, X. Kou, J. Wu, Q. Yang, H. Zhang, and J. Q. Xiao, Applied Physics Letters **99**, 232506 (2011)

[51] L. Bianchini, S. Cornelissen, J.-V. Kim, T. Devolder, W. van Roy, L. Lagae, and C. Chappert, Applied Physics Letters **97**, 032502 (2010)

[52] Y. Khivintsev, B. Kuanr, T. J. Fal, M. Haftel, R. E. Camley, Z. Celinski, and D. L. Mills, Phys. Rev. B **81**, 054436 (2010)

[53] G. Floquet, Ann. *É*cole Norm. Sup. **12**, 47 (1883)

[54] R. Matsumoto and S. Murakami, Phys. Rev. Lett. **106**, 197202 (2011)

[55] T. Martin, G. Woltersdorf, C. Stamm, H. A. Dürr, R. Mattheis, C. H. Back, and G. Bayreuther, Journal of Applied Physics **105**, 07D310 (2009)

[56] S. Y. An, P. Krivosik, M. A. Kraemer, H. M. Olson, A. V. Nazarov, and C. E. Patton, Journal of Applied Physics **96**, 1572 (2004)

[57] J. P. Park, P. Eames, D. M. Engebretson, J. Berezovsky, and P. A. Crowell, Phys. Rev. Lett. **89**, 277201 (2002)

[58] J. Jorzick, S. O. Demokritov, B. Hillebrands, M. Bailleul, C. Fermon, K. Y. Guslienko, A. N. Slavin, D. V. Berkov, and N. L. Gorn, Phys. Rev. Lett. **88**, 047204 (2002)

[59] D. R. Birt, K. An, M. Tsoi, S. Tamaru, D. Ricketts, K. L. Wong, P. Khalili Amiri, K. L. Wang, and X. Li, Applied Physics Letters **101**, 252409 (2012)

[60] V. E. Demidov, S. O. Demokritov, K. Rott, P. Krzysteczko, and G. Reiss, Phys. Rev. B **77**, 064406 (2008)

[61] K. Vogt, H. Schultheiss, S. Jain, J. E. Pearson, A. Hoffmann, S. D. Bader, and B. Hillebrands, Applied Physics Letters **101**, 042410 (2012)

[62] V. Vlaminck and M. Bailleul, Science **322**, 410 (2008)

[63] V. Vlaminck and M. Bailleul, Phys. Rev. B **81**, 014425 (2010)

[64] M. Zhu, C. L. Dennis, and R. D. McMichael, Phys. Rev. B **81**, 140407 (2010)

[65] K. Sekiguchi, K. Yamada, S.-M. Seo, K.-J. Lee, D. Chiba, K. Kobayashi, and T. Ono, Physical Review Letters **108**, 017203 (2012)

[66] J.-Y. Chauleau, H. G. Bauer, H. S. Körner, J. Stigloher, M. Härtinger, G. Woltersdorf, and C. H. Back, Phys. Rev. B **89**, 020403 (2014)

[67] S. Neusser, G. Duerr, H. G. Bauer, S. Tacchi, M. Madami, G. Woltersdorf, G. Gubbiotti, C. H. Back, and D. Grundler, Phys. Rev. Lett. **105**, 067208 (2010)

[68] H. G. Bauer, J.-Y. Chauleau, G. Woltersdorf, and C. H. Back, Applied Physics Letters **104**, 102404 (2014)

[69] S. Nikitov, P. Tailhades, and C. Tsai, Journal of Magnetism and Magnetic Materials **236**, 320 (2001)

[70] S. Neusser and D. Grundler, Advanced Materials **21**, 2927 (2009)

[71] V. V. Kruglyak, S. O. Demokritov, and D. Grundler, Journal of Physics D Applied Physics **43**, 264001 (2010)

[72] S. Neusser, H. G. Bauer, G. Duerr, R. Huber, S. Mamica, G. Woltersdorf, M. Krawczyk, C. H. Back, and D. Grundler, Phys. Rev. B **84**, 184411 (2011)

[73] M. Haidar and M. Bailleul, Phys. Rev. B **88**, 054417 (2013)

[74] T. L. Gilbert, Phys. Rev. **100**, 1243 (1955)

[75] K. J. Harte, Journal of Applied Physics **39**, 1503 (1968)

[76] B. A. Kalinikos and A. N. Slavin, Journal of Physics C Solid State Physics **19**, 7013 (1986)

[77] R. D. McMichael, M. D. Stiles, P. J. Chen, and W. F. Egelhoff, Journal of Applied Physics **83**, 7037 (1998)

[78] A. Aharoni, Journal of Applied Physics **83** (1998)

[79] G. Tatara, H. Kohno, and J. Shibata, Physics Reports **468**, 213 (2008)

[80] D. Ralph and M. Stiles, Journal of Magnetism and Magnetic Materials **320**, 1190 (2008)

[81] T. Silva and W. Rippard, Journal of Magnetism and Magnetic Materials **320**, 1260 (2008)

[82] S. S. P. Parkin, M. Hayashi, and L. Thomas, Science **320**, 190 (2008)

[83] V. Vlaminck and M. Bailleul, Science **322**, 410 (2008)

[84] R. D. McMichael and M. D. Stiles, Science **322**, 386 (2008)

[85] G. Woltersdorf, M. Kiessling, G. Meyer, J.-U. Thiele, and C. H. Back, Phys. Rev. Lett. **102**, 257602 (2009)

[86] S. Pollard, L. Huang, K. Buchanan, D. Arena, and Y. Zhu, Nature Communications **3** (2012)

[87] G. S. D. Beach, C. Knutson, C. Nistor, M. Tsoi, and J. L. Erskine, Phys. Rev. Lett. **97**, 057203 (2006)

[88] T. Ono, H. Miyajima, K. Shigeto, K. Mibu, N. Hosoito, and T. Shinjo, Science **284**, 468 (1999)

[89] D. Atkinson, D. A. Allwood, G. Xiong, M. D. Cooke, C. C. Faulkner, and R. P. Cowburn, Nat Mater **2**, 85 (2003)

[90] B. Wiele, L. Laurson, and G. Durin, The European Physical Journal B **86**, 1 (2013)

[91] J. Leliaert, B. V. de Wiele, A. Vansteenkiste, L. Laurson, G. Durin, L. Dupre, and B. V. Waeyenberge, arXiv:1306.0681(2013)

[92] T. Weindler, H. G. Bauer, R. Islinger, B. Boehm, J.-Y. Chauleau, and C. H. Back(2014)

[93] G. S. D. Beach, C. Nistor, C. Knutson, M. Tsoi, and J. L. Erskine, Nat Mater **4**, 741 (2005)

[94] S. Neusser and D. Grundler, Advanced Materials **21**, 2927 (2009)

[95] D. J. Clarke, O. A. Tretiakov, G.-W. Chern, Y. B. Bazaliy, and O. Tchernyshyov, Phys. Rev. B **78**, 134412 (2008)

[96] A. A. Thiele, Phys. Rev. Lett. **30**, 230 (1973)

[97] D. L. Huber, Phys. Rev. B **26**, 3758 (1982)

[98] K.-S. Lee, S.-K. Kim, Y.-S. Yu, Y.-S. Choi, K. Y. Guslienko, H. Jung, and P. Fischer, Phys. Rev. Lett. **101**, 267206 (2008)

[99] R. Islinger, T. Weindler, H. G. Bauer, J.-Y. Chauleau, and C. H. Back(2014)

[100] R. L. Compton and P. A. Crowell, Phys. Rev. Lett. **97**, 137202 (2006)

[101] H. Min, R. D. McMichael, M. J. Donahue, J. Miltat, and M. D. Stiles, Phys. Rev. Lett. **104**, 217201 (2010)

[102] K. Y. Guslienko, G. R. Aranda, and J. M. Gonzalez, Phys. Rev. B **81**, 014414 (2010)

[103] B. Van Waeyenberge, A. Puzic, H. Stoll, K. W. Chou, T. Tyliszczak, R. Hertel, M. Fähnle, H. Brückl, K. Rott, G. Reiss, I. Neudecker, D. Weiss, C. H. Back, and G. Schütz, Nature **444**, 461 (2006)

[104] R. Hertel and C. M. Schneider, Phys. Rev. Lett. **97**, 177202 (2006)

[105] J.-Y. Chauleau, R. Weil, A. Thiaville, and J. Miltat, Phys. Rev. B **82**, 214414 (2010)

[106] Y. Nakatani, A. Thiaville, and J. Miltat, Journal of Magnetism and Magnetic Materials **290–291, Part 1**, 750 (2005), proceedings of the Joint European Magnetic Symposia (JEMS' 04)

[107] N. L. Schryer and L. R. Walker, Journal of Applied Physics **45**, 5406 (1974)

[108] H. Min, R. D. McMichael, J. Miltat, and M. D. Stiles, Phys. Rev. B **83**, 064411 (2011)

[109] J. Foros, A. Brataas, Y. Tserkovnyak, and G. E. W. Bauer, Phys. Rev. B **78**, 140402 (2008)

[110] S. Zhang and S. S.-L. Zhang, Phys. Rev. Lett. **102**, 086601 (2009)

[111] H. T. Nembach, J. M. Shaw, C. T. Boone, and T. J. Silva, Phys. Rev. Lett. **110**, 117201 (2013)

[112] Z. Yuan, K. M. D. Hals, Y. Liu, A. Starikov, A. Brataas, and P. J. Kelly, arXiv:1404.1488(2014)

[113] K. Y. Guslienko, Applied Physics Letters **89**, 022510 (2006)

[114] S. Rößler, S. Hankemeier, B. Krüger, F. Balhorn, R. Frömter, and H. P. Oepen, Phys. Rev. B **89**, 174426 (2014)

[115] J. Xiao, A. Zangwill, and M. D. Stiles, Phys. Rev. B **73**, 054428 (2006)

[116] M. Eltschka, M. Wötzel, J. Rhensius, S. Krzyk, U. Nowak, M. Kläui, T. Kasama, R. E. Dunin-Borkowski, L. J. Heyderman, H. J. van Driel, and R. A. Duine, Phys. Rev. Lett. **105**, 056601 (2010)

[117] D. Claudio-Gonzalez, A. Thiaville, and J. Miltat, Phys. Rev. Lett. **108**, 227208 (2012)

[118] K.-J. Lee, M. Stiles, H.-W. Lee, J.-H. Moon, K.-W. Kim, and S.-W. Lee, Physics Reports **531**, 89 (2013), self-consistent calculation of spin transport and magnetization dynamics

[119] H. G. Bauer, M. Sproll, C. H. Back, and G. Woltersdorf, Phys. Rev. Lett. **112**, 077201 (2014)

[120] M. Sproll, M. Noske, H. Bauer, M. Kammerer, A. Gangwar, G. Dieterle, M. Weigand, H. Stoll, G. Woltersdorf, C. H. Back, and G. Schütz, Applied Physics Letters **104**, 012409 (2014)

[121] A. Wachowiak, J. Wiebe, M. Bode, O. Pietzsch, M. Morgenstern, and R. Wiesendanger, Science **298**, 577 (2002)

[122] S. Bohlens, B. Krüger, A. Drews, M. Bolte, G. Meier, and D. Pfannkuche, Applied Physics Letters **93**, 142508 (2008)

[123] M. Bolte, G. Meier, B. Krüger, A. Drews, R. Eiselt, L. Bocklage, S. Bohlens, T. Tyliszczak, A. Vansteenkiste, B. Van Waeyenberge, K. W. Chou, A. Puzic, and H. Stoll, Phys. Rev. Lett. **100**, 176601 (2008)

[124] S.-K. Kim, K.-S. Lee, Y.-S. Yu, and Y.-S. Choi, Applied Physics Letters **92**, 022509 (2008)

[125] K. Nakano, D. Chiba, N. Ohshima, S. Kasai, T. Sato, Y. Nakatani, K. Sekiguchi, K. Kobayashi, and T. Ono, Applied Physics Letters **99**, 262505 (2011)

[126] K. Y. Guslienko, B. A. Ivanov, V. Novosad, Y. Otani, H. Shima, and K. Fukamichi, Journal of Applied Physics **91**, 8037 (2002)

[127] F. Hoffmann, G. Woltersdorf, K. Perzlmaier, A. N. Slavin, V. S. Tiberkevich, A. Bischof, D. Weiss, and C. H. Back, Phys. Rev. B **76**, 014416 (2007)

[128] K. Y. Guslienko, A. N. Slavin, V. Tiberkevich, and S.-K. Kim, Phys. Rev. Lett. **101**, 247203 (2008)

[129] M. Buess, R. Höllinger, T. Haug, K. Perzlmaier, U. Krey, D. Pescia, M. R. Scheinfein, D. Weiss, and C. H. Back, Phys. Rev. Lett. **93**, 077207 (2004)

[130] C. E. Zaspel, B. A. Ivanov, J. P. Park, and P. A. Crowell, Phys. Rev. B **72**, 024427 (2005)

[131] M. Buess, T. P. J. Knowles, R. Höllinger, T. Haug, U. Krey, D. Weiss, D. Pescia, M. R. Scheinfein, and C. H. Back, Phys. Rev. B **71**, 104415 (2005)

[132] M. Kammerer, M. Weigand, M. Curcic, M. Noske, M. Sproll, A. Vansteenkiste, B. Van Waeyenberge, H. Stoll, G. Woltersdorf, C. H. Back, and G. Schütz, Nature Communications **2** (2011)

[133] R. Hertel, S. Gliga, M. Fähnle, and C. M. Schneider, Phys. Rev. Lett. **98**, 117201 (2007)

[134] Q. F. Xiao, J. Rudge, B. C. Choi, Y. K. Hong, and G. Donohoe, Applied Physics Letters **89**, 262507 (2006)

[135] M. Curcic, B. Van Waeyenberge, A. Vansteenkiste, M. Weigand, V. Sackmann, H. Stoll, M. Fähnle, T. Tyliszczak, G. Woltersdorf, C. H. Back, and G. Schütz, Phys. Rev. Lett. **101**, 197204 (2008)

[136] Y. Gaididei, V. P. Kravchuk, D. D. Sheka, and F. G. Mertens, Phys. Rev. B **81**, 094431 (2010)

[137] M. Kammerer, H. Stoll, M. Noske, M. Sproll, M. Weigand, C. Illg, G. Woltersdorf, M. Fähnle, C. Back, and G. Schütz, Phys. Rev. B **86**, 134426 (2012)

[138] M. Kammerer, M. Sproll, H. Stoll, M. Noske, M. Weigand, C. Illg, M. Fähnle, and G. Schütz, Applied Physics Letters **102**, 012404 (2013)

[139] H. G. Bauer, P. Majchrak, K. Torsten, C. H. Back, and G. Woltersdorf, arXiv, 1410.6693(2014)

[140] M. Obstbaum, M. Härtinger, H. G. Bauer, T. Meier, F. Swientek, C. H. Back, and G. Woltersdorf, Phys. Rev. B **89**, 060407 (2014)

[141] A. Gangwar, H. G. Bauer, J.-Y. Chauleau, M. Noske, M. Weigand, H. Stoll, G. Schütz, and C. H. Back(2014)

[142] G. Woltersdorf, F. Hoffmann, H. G. Bauer, and C. H. Back, Phys. Rev. B **87**, 054422 (2013)